EINDHOVEN UNIVERSITY OF TECHNOLOGY

Eindhoven University of Technology

MASTER

Towards hexagonal silicon-germanium lasers

van Lange, V.T.

Award date:
2020

Link to publication

Disclaimer
This document contains a student thesis (bachelor's or master's), as authored by a student at Eindhoven University of Technology. Student theses are made available in the TU/e repository upon obtaining the required degree. The grade received is not published on the document as presented in the repository. The required complexity or quality of research of student theses may vary by program, and the required minimum study period may vary in duration.

General rights
Copyright and moral rights for the publications made accessible in the public portal are retained by the authors and/or other copyright owners and it is a condition of accessing publications that users recognise and abide by the legal requirements associated with these rights.

- Users may download and print one copy of any publication from the public portal for the purpose of private study or research.
- You may not further distribute the material or use it for any profit-making activity or commercial gain

Towards hexagonal silicon-germanium lasers

V.T. van Lange

January 14, 2020

Author:	V.T. (Victor) van Lange
StudentID:	0886748
Email:	v.t.v.lange@student.tue.nl
Supervisor:	Prof. Dr. E.P.A.M Bakkers
	Dr. J.E.M. Haverkort
Daily Supervisor	A. Dijkstra
Affiliation:	Dep. Applied Physics and Institute for Photonic Integration
	Eindhoven University of Technology
	P.O. Box 513
	5600 MB Eindhoven - The Netherlands
Cooperation with:	Prof. Dr. J. Finley
Daily supervisor:	D. Busse
Affiliation:	Walter Schottky Institut
	Technische Universität München
	Am Coulombwall 4
	D-85748 Garching - Germany

Abstract

To keep improving microprocessors in the near future, the interconnects between chips and chiplets should be changed from electrical to optical to improve performance and lower power consumption. Recent work has shown that the group-IV material hexagonal silicon-germanium has a direct band-gap, a radiative lifetime competitive with the III-V materials and a large tunability of the emission wavelength. These properties are essential to create a laser that can function as a light source for these optical interconnects.

In this work, two laser structures are introduced using this hexagonal silicon-germanium material, the photonic band edge laser and the single nanowire Fabry-Perot laser. First we evaluate the photonic band edge laser geometry using Finite-Difference Time-Domain simulations to determine the photonic crystal design parameters. For the target design parameters, the emission is coupled to a slow light mode for gain enhancement. Secondly, using simulations, we determine the optimal guided mode for single-nanowire Fabry-Perot laser to be the TE01 mode. Finally we evaluate the nanowires for laser properties using time-resolved photoluminescence and show a number of interesting properties, including saturation behaviour due to a presumed non-radiative state acting as a carrier reservoir.

Acknowledgements

I would like to thank a number of people for their help and support during my Master Thesis. Foremost I would like to thank my daily supervisor Alain Dijkstra for his mentoring during my project. Especially near the end we had many conversations together over nearly as many cups of coffee. Your perspective often helped me refocus and find the answers I often already had. I also like to thank David Busse, my daily supervisor from Munich, for his help during the first part of my project. Together we figured out how to set up the simulations and process and interpret the result. During this process we exchanged a lot of knowledge, optimisation ideas and especially lots of frustration with the software. Furthermore I like to thank my main supervisors. Prof. Dr. Erik Bakkers whose enthusiasm lead me to this great project in this fantastic group, Prof. Dr. Jonathan Finley from Munich whose many ideas and insights were extremely valuable for this project, and Dr. Jos Haverkort for being very enthusiastic about the project and being nearly always available to discuss any result or idea. My most special thanks go to Elham Fadaly for growing the samples I designed and measured and her amazing work on the growth optimisations that were required to do so. I would like to thank Ksenia Korzun for helping me figure out the simulations and for helping me measure on the Fourier microscope. Furthermore I would like to thank the entire AND group for welcoming me and making me feel part of the group.

Thank you to my fellow master students: Marvin van Tilburg, Chenyang Mao, David Rodrigues and Wouter Peeters, for all the lunches and talks we enjoyed together, it made the journey all the more fun.

Finally I like to thank my family and friends for their continuous support the past year, for listening to my stories and cheering me on.

Contents

Abstract 1

Acknowledgements 2

1 Introduction 6
1.1 Hexagonal Silicon-Germanium 9
1.1.1 Efficient light emission 9
1.1.2 Wavelength tuning 9
1.1.3 Efficiency 12
1.2 Research goals and outline of work 13

2 Background 15
2.1 Optical emission from semiconductors 15
2.1.1 Intensity, excitation dependence 15
2.1.2 Lifetime, excitation dependence 17
2.1.3 Lifetime, temperature dependence 17
2.1.4 Intensity, temperature dependence 18
2.1.5 Experimental observation 19
2.2 Lasers 19
2.2.1 Fabry-Perot resonator 22
2.2.2 Photonic crystals 23

3 Fabrication 28
3.1 SiGe growth 28
3.2 Gold capping 31

4 Experimental setup 33
4.1 Finite Difference Time Domain simulations 33
4.1.1 Bloch boundary conditions 34
4.1.2 Perfectly Matched Layer boundary condition 37
4.2 Fourier transform infrared spectroscopy based PL 38
4.3 Time-resolved photo-luminescence 40
4.4 Fourier Plane Imaging Microscopy 41
4.5 Scanning electron microscope 42

5 Photonic band edge laser **44**
5.1 Introduction 44
5.2 Simulation setup 46
5.3 Simulation results 50
5.3.1 Further verification and stability 55
5.4 Fabricated structure 62
5.5 FPIM results 65

6 Single Nanowire laser **67**
6.1 Simulation setup 67
6.2 Simulation results 69
6.3 Method 72
6.4 Results 74
6.4.1 Radiative limit 77
6.4.2 Gold capping 82

7 Summary & Conclusion **86**
7.1 Outlook & Recommendation 87

References **90**

Appendices **99**

A Neutral density filter calibration **99**

B Hex-SiGe refractive index material models **100**

1 Introduction

Microprocessors are everywhere, at home, at work and in your pocket. In everyday life we use devices with a microprocessor, or computer chip, like a phone or laptop. However not many people realise that we use these small and compact machines to connect to a much larger aggregate of processors in the datacenter, which is where most of the processing capacity in the world is located.

All these devices are expected to increase in performance each year as we continuously demand more performance. This growth in performance is still governed by Moore's law stating the number of components on a chip, and therefore the performance will double every two years [1]. This prediction is still accurate and results in the existence of multiple so called "wars" which can be determined from figure 1. The initial war, the so called megahertz, or later gigahertz war, was based on increasing the processor clock speed as much as possible to improve the performance. This effect can be seen form single thread performance in blue which starts strongly correlated with the clock frequency in green. This war continued upto around 2005 when the clock speed became stagnant between 4 to $5GHz$ due to rapidly increasing power consumption shown in red.

Because it was no longer possible to increase the performance of one core, the focus changed to increasing performance by having the processor multi-task using multiple cores. This is visible from the black dataset showing the number of cores go up at the same time as the frequency levels off. From this point onwards, the industry transitioned into the still ongoing cores war. This core war also recently changed the paradigm of how a processor is built. Instead of creating a large monolithic chip, a chiplet architecture is explored where multiple smaller chips are combined in one package to together form one big processor. This is necessary to increase performance and decrease power consumption, but also to improve the yield and thereby decrease the cost of these chips [2]. Additionally using chiplets, the optimum technology can be used for each component [2]. A prime example of this technology is the AMD Epyc "Rome" using nine chiplets to create one processor[3] shown in figure 2.

However as the number of cores and chiplet pieces are used to create one processor increases, so does the need for interconnects to bind the cores together. These interconnects need to have increasingly low latency and high bandwidth to be able to "feed" the cores the data they need to do the computations. Furthermore, in recent datacenter class processors over 40% of the power consumed by the processor is used by the interconnect fabric [4]. These datacenters together use 2.5% of the global yearly power

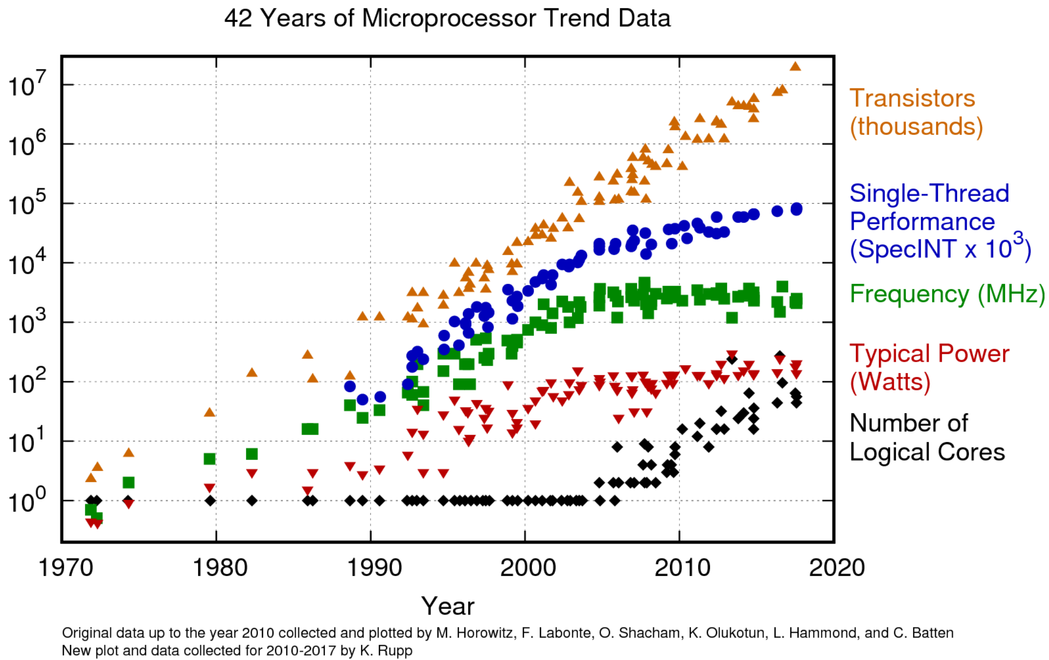

Figure 1: The evolution of microprocessors over the years in terms of transistor count (orange), single core/thread performance (blue), clock frequency (green), power consumption (red) and the amount of cores in black. Figure from [6, Fig. 1].

consumption which is only expected to increase [5].

This is where optical interconnects will come into play. Light has been the *de facto* standard for long distance (kilometers) communication for years in the form of single-mode fibre-optics. Not only because of its higher bandwidth and lower latency, but also due to the lower power consumption and the immunity to electromagnetic interference (EMI). These are exactly the properties that are required for the inevitable interconnect war that will be required to further increase processor speeds.

The use of optical interconnects has been proposed for both chiplet-to-chiplet communication with a chiplet-on-interposer architecture [8], and the processor-to-processor communication [9]. These complementary technologies approach the communication problem using low power optical networks to connect the individual components. To increase the density and bandwidth of these networks, they leverage wavelength division multiplexing to send multiple wavelengths over the same waveguide simultaneously. Furthermore latency and power are decreased because an optical interconnect does not have a capacitance that needs to be charged [10]. Only at the very smallest scale, within a chiplet, the interconnects will remain electrical. The optical interconnects will be too large to in-

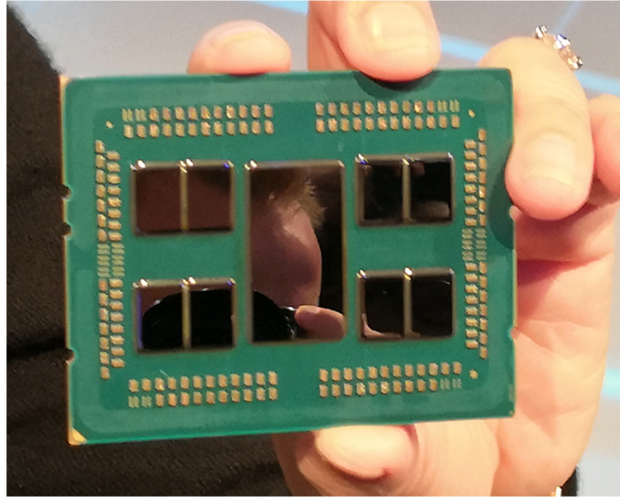

Figure 2: The AMD Epyc "Rome" processor using nine chiplets to form one processor. The eight small chiplets house eight cores each for a total of 64 cores, while the larger center chiplet provides all the IO which includes components such as memory controllers and interconnects. Figure from [7, Fig. 1].

tegrate at those scales as the size of integrated optical components is inevitably the micrometer range compared to the nanometer scale used in current CMOS technology. This means that future systems should become opto-electronic hybrids.

For these hybrid architectures we need both sources and detectors for multiple wavelengths, preferably those with low cost and easy integration with current CMOS based technologies. In this work we will focus on the sources and more specifically nanolasers. Lasers are components that convert electrical to optical signals of a well defined wavelength. The cavity and the gain material are the two most important components of a laser that influence its efficiency and its emission wavelength. Using group III-V materials like indium-phosphide (InP) and gallium-arsenide (GaAs) it is possible to make fast and efficient lasers. These materials have a short radiative lifetime, meaning that lasers from these materials can be switched on and of quickly which is required for a high bandwidth interconnect [11–13]. However these materials have two major issues: they are difficult to integrate with silicon and they are expensive. Using group IV materials like silicon and germanium would be preferred as CMOS technology is already based on these materials, they are more abundant and the supply channels already benefit from the economy of scale making it vastly cheaper. That is, if they would be efficient light emitters, which they are unfortunately not because of their indirect band-gap [14].

1.1 Hexagonal Silicon-Germanium

In this chapter we will introduce the hexagonal silicon germanium material and discuss why it is an efficient light emitter. Additionally we will discuss the tunability of the wavelength and finally the efficiency of the material.

1.1.1 Efficient light emission

To use a material as a light source, the material needs to be an efficient light emitter. To be an efficient emitter means that the semiconductor should have a direct band gap. In a direct band gap semiconductor, the conduction band minimum and the valence band maximum are located at the same k point, this makes it easier for the material to emit light as the electron only needs to jump straight across instead of also jumping in k. This is exactly what the naturally occurring cubic crystal structure silicon and germanium have not. The bandstructures of cubic silicon and germanium are presented in figure 3 A and B both with a conduction band minimum that is not aligned with the k point of the valence band maximum as can be seen from the annotated blue circles. Notably, while germanium has a local minimum in the conduction band at the Γ point, it is still an indirect semiconductor as it is not the global minimum.

However, when changing this cubic crystal structure to a hexagonal crystal structure, the bandstructure changes too. For hexagonal silicon, a local minimum appears at the Γ point, however it remains an indirect bandgap semiconductor as the global conduction band minimum is located at the M point instead [15] as shown in figure 3C by the annotated circles. For hexagonal germanium on the other hand, this change of crystal phase makes it exhibit a direct bandgap as the conduction band minimum and the valence band maximum are now aligned [15, 16] as seen in figure 3D. This means that hex-Ge is well suited to be used as an optical source.

1.1.2 Wavelength tuning

The direct bandgap of hex-Ge is approximately $0.3eV$, which is very small compared to other direct bandgap materials like indium-phosphide (InP) and gallium-arsenide (GaAs) at round $1.3-1.5eV$ [17], and hex-Si has no direct bandgap, but the gap between the local minimum of the conduction band and the maximum of the valence band at the Γ point is approximately $1.7eV$. By alloying these materials we can get the best of both worlds, the direct bandgap from the hex-Ge and increase its size by adding hex-Si.

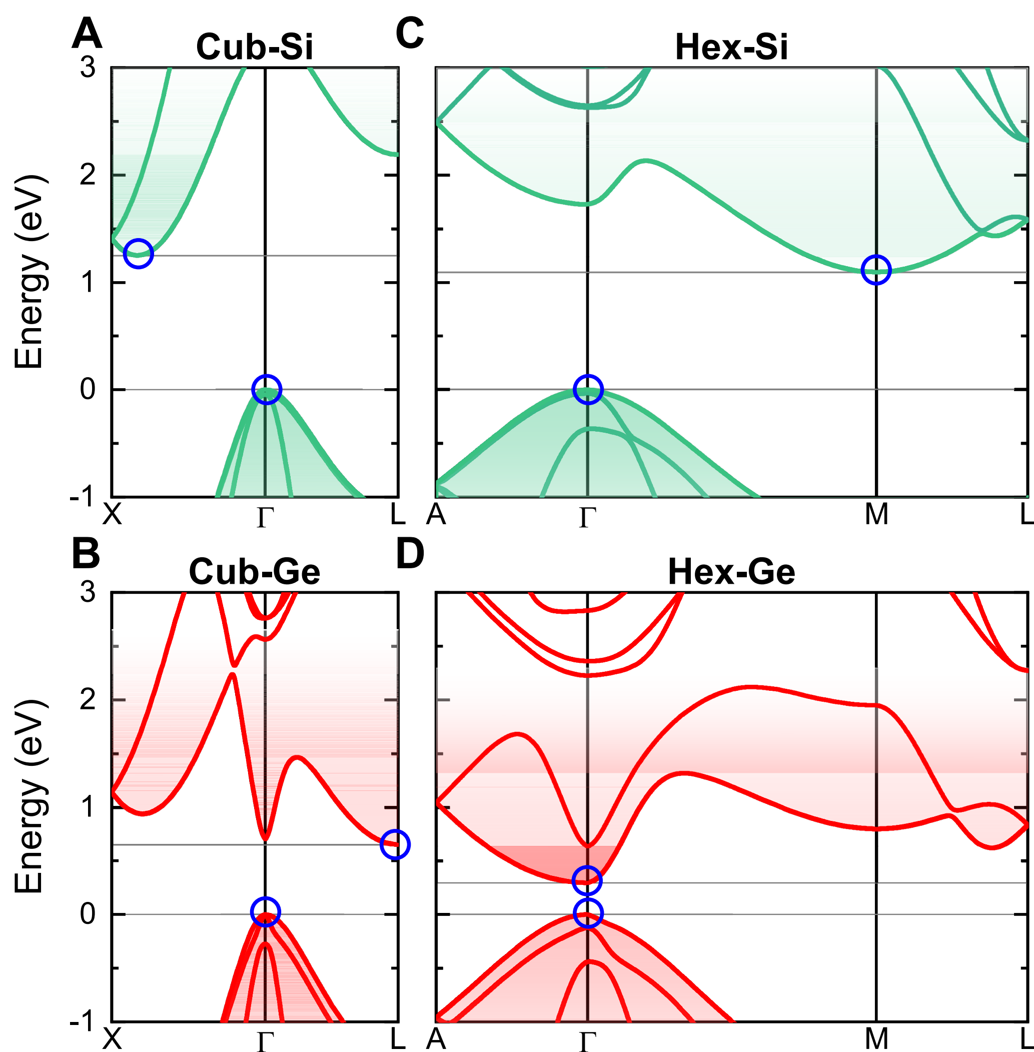

Figure 3: The bandstructures of cubic and hexagonal silicon and germanium calculated by DFT showing the indirect nature of A) cubic-Si, C) hexagonal-Si and B) cubic-Ge and the direct bandgap nature of D) hexagonal-Ge. In each bandstructure, the positions of the conduction band minimum and the valence band maximum are annotated by the blue circles. Adapted from [15, Fig. 1].

To find the limits of this tunability, *ab initio* Density Functional Theory (DFT) can be used to calculate how the energies of the different conduction band minima for hex-Ge at the Γ, M, L and U points from figure 3 shift when the germanium is alloyed with silicon to form different alloy ratios $Si_{1-x}Ge_x$ where x ratio of germanium in the alloy.. These DFT calculations result in the lines plotted in figure 4B. Only when the Γ point has the lowest energy is the bandgap direct. Therefore it can be seen that hex-SiGe is predicted to be a direct bandgap semiconductor for compositions from $x = 100\%$ to $x = 65\%$ germanium and that the emission energy can be tuned from $0.3eV$ to nearly $0.7eV$ which in wavelength is equivalent to a range from $\sim 4.1\mu m$ to $\sim 1.8\mu m$.

From the Γ line in figure 4B, an empirical relation between the emission energy and the material composition is estimated using a polynomial fit resulting in

$$E_{emission} = 1.62383 - 1.59678\,x + 0.32893\,x^2 \tag{1.1}$$

With x the Germanium fraction, which is only valid for compositions where Γ is the lowest. This relation will be used to estimate the emission energy for compositions that have not yet been measured in PL as the simulations need to be optimised for this emission energy.

This prediction was verified by measuring the photoluminescence (PL) spectrum for multiple $Si_{1-x}Ge_x$ alloy ratios in the 100% to 65% range which are shown in figure 4A. The peak center is determined for each composition and added to the prediction in figure 4A, it can be seen that the prediction and the measurement are in good agreement, confirming the tunability of the hex-SiGe.

Being able to tune the emission wavelength is a strongly desired feature for the creation of many devices. Some examples include photovoltaics [18], where layers with different band gaps are used to increase the efficiency of infrared sensors which, just like solar cells, benefit of efficient absorption. But also for integrated photonics applications like wavelength division multiplexing [19] the tunability can be used to create transmitters and/or receivers for different wavelengths from similar material, reducing compatibility issues. The more silicon rich alloys, like 65%, also come close to the U-band fibre optics wavelength starting at $1675nm$ [20], meaning hex-SiGe could also be used for long range fibre based communication. Finally hex-SiGe could also be of use in gas sensing in agricultural industry as the wavelength of the hex-SiGe can be tuned to match the absorption lines of CO_2 and H_2O [21].

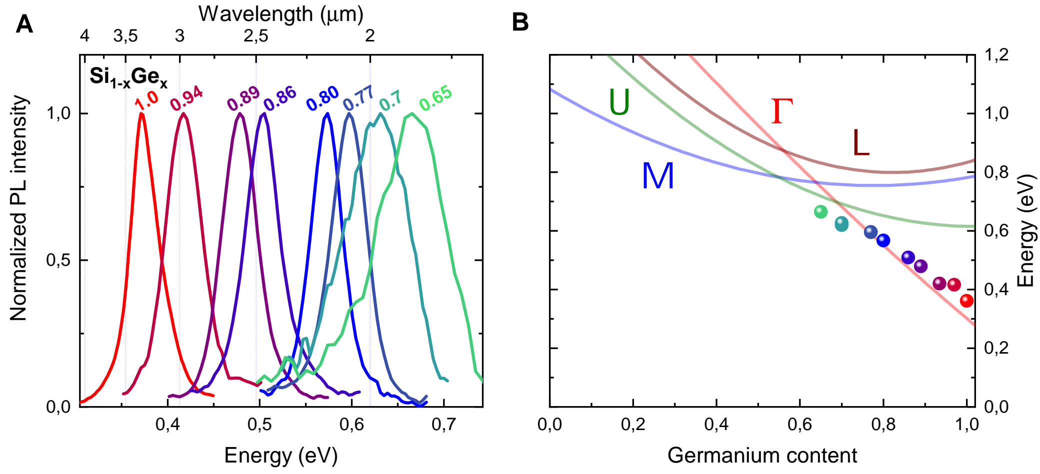

Figure 4: A) the photoluminesence spectra of the different alloy compositions showing a clear shift of the emission center when adding more silicon to the germanium. B) The predicted conduction band minima from the DFT calculations together with the measured positions from A. The measured PL is in reasonable agreement with the prediction and illustrates the large tuning range in emission energy for the different alloy compositions.

1.1.3 Efficiency

Even when the bandgap is found to be direct, not all band-to-band transitions have to be allowed. Some of these transitions are forbidden by the selection rules given by group theory [22] which are based on the crystal symmetry. The same hex-Ge bandstructure as in figure 3D is shown in figure 5a with the two valence and conduction band edges closest to the bandgap annotated at the Γ point. In figure 5b the optical transitions and their strength are presented and it is visible that most of the transitions are forbidden and that the direct transition across the bandgap $\Gamma_{9v}^{+} \rightarrow \Gamma_{8c}^{-}$ is only weakly allowed.

However when a hex-SiGe alloy is formed, the symmetry of the hexagonal crystal is broken because germanium atoms in the unit cell are replaced randomly by silicon atoms. As the selection rules are based on symmetry, this can re-allow forbidden transitions, making the emission more efficient. It was recently shown that for both the hex-Ge and the hex-SiGe a very short lifetime is found of $\sim 1ns$ which is similar to GaAs and InP at similar doping levels [11–13, 15]. The exact cause of this lower than expected lifetime for hex-Ge is still unknown, but it might be related to high arsenic doping concentration caused by the growth. This shows that hex-Ge and hex-SiGe are not just direct band gap semiconductors, but also that their emission is an efficient and above all fast process com-

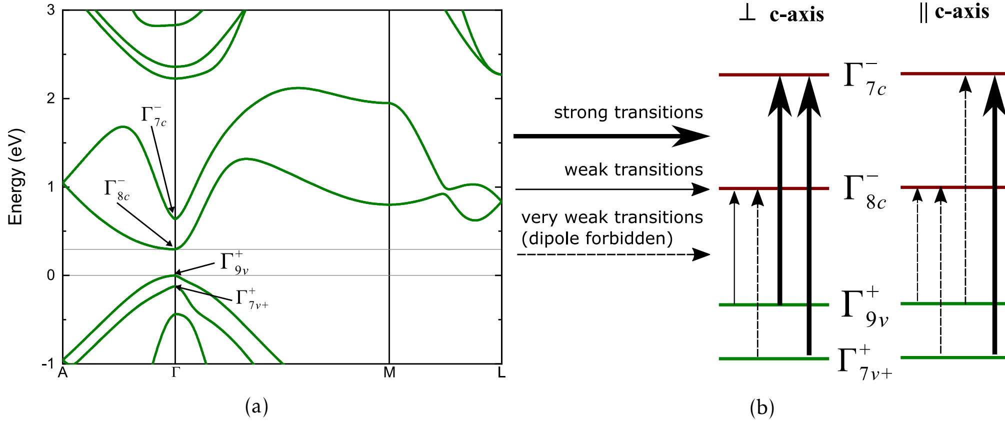

Figure 5: a) The bandstructure of hex-Ge annotated with the Γ band edges and b) A diagram showing the optical transition strength for each of the valence to conduction band transitions determined from the matrix elements. Notably the transition directly across the bandgap is only weakly allowed. Adapted from [16, Fig.4b and Table VII].

petitive with III-V materials like InP and GaAs.

Fast light emission means that the material can be turned on and off quickly which is an essential light source property for an optical interconnect as it determines the bandwidth.

1.2 Research goals and outline of work

As hex-Ge and hex-SiGe are found to be efficient direct band gap light emitters with a competitively short radiative lifetime compared to the rivalling III-V materials, the next step is to show lasing. Therefore a cavity should be designed to provide the necessary optical feedback. However as the state-of-the-art fabrication method of this material system is limited to nanowires instead of planar layers, this goal comes with a unique set of challenges.

To account for the limited geometrical design freedom of the material, there are two possible laser structures that are investigated in this work. The first design is the Photonic Band Edge Laser which uses a photonic crystal of hex-SiGe nanowires to provide the required feedback. As the design of a photonic crystal is non-trivial, the photonic band edge laser design is investigated numerically in detail to find the optimum parameters for such a laser device. After fabricating the designed structure, we attempt to verify the presence of photonic effects.

The second geometry is the more simple Fabry-Perot nanowire cavity laser. Using simulations, the optimum nanowire thickness and corre-

sponding laser mode can be determined by calculating the modal reflectivity as a function of nanowire diameter. This information can be used to optimise the growth. Finally, nanowires of this thickness range can be evaluated for signs of laser properties using Time-Resolved photoluminescence.

The main research goals are:

- Numerically determine the design parameters of a hex-SiGe photonic band edge laser.
- Verify the presence of photonic effects in the fabricated photonic band edge structure.
- Numerically determine the optimal thickness and corresponding laser mode for a Fabry-Perot nanowire laser by evaluating the modal reflectivity.
- Optically characterize the nanowires in this thickness range using Time-Resolved photoluminescence for laser properties.

The report is structures into four main parts: The general information, the photonic band edge laser, the single nanowire laser and the conclusions. In the general part, we already introduced the material in this chapter, the next chapter will focus on introducing the theory of semiconductor light emission, lasers and how photonic crystals work and can be used for lasing in the case of the photonic band edge laser. Afterwards we continue with chapter three explaining the fabrication of the hex-SiGe material which is the basis of the introduced laser structures. The fourth chapter will introduce the simulation technique and the experimental setups.

In the fifth chapter we will dive deep into the design of the photonic band edge laser. The structure will be introduced and the simulation setup and results will be discussed in detail. Furthermore we will show final design and the fabricated structure and attempt to verify the presence of photonic effects.

The single nanowire Fabry-Perot laser will be discussed in the next part. The simulation setup will be explained and the optimal laser mode and diameter will be determined. This will be followed up by time-resolved photoluminescence measurements of nanowires in this width regime.

Chapter seven will be used to conclude and give recommendations for future research.

2 Background

In this chapter, the general theory required in this work will be introduced. First a model for the semiconductor emission is introduced to differentiate behaviour of radiative and non-radiative recombination. Afterwards the laser components and conditions are discussed and finally the fundamentals of photonic crystals are introduced and placed in context of gain enhancement and threshold reduction.

2.1 Optical emission from semiconductors

To better understand the material for stimulated emission and lasing, it is important to first have a base model for the emission of the degenerately n-doped hex-SiGe. Here the excitation power and temperature dependence for the different recombination channels will be briefly discussed.

In semiconductors, when a valence band electron absorbs a photon with an energy larger than the bandgap energy, it is excited from the valence band into the conduction band leaving a hole creating an electron-hole pair. Later when the electron and hole want to recombine, there are three main channels to do so: When the electron and hole can recombine non-radiatively assisted by a trap level inside the bandgap, this process is called Shockly-Read-Hall (SRH) recombination. Alternatively, when a photon with frequency $\Delta E = h\nu$ is emitted when recombining the electron and hole at an energy difference ΔE, the process is categorised as radiative recombination. Finally when the electron and hole recombine but the energy is transferred to another carrier (e or h) instead of producing a photon, the process is labelled Auger recombination. These three processes are shown schematically in figure 6.

2.1.1 Intensity, excitation dependence

The different recombination processes require the presence of a different number of carriers. The SRH recombination only needs to trap a single carrier, radiative recombination obviously needs both an electron and a hole and Auger recombination needs three carriers, two to recombine and one more to transfer the energy to. As the system is degenerately n-doped, it can be assumed that the electrons greatly outnumber the holes. Because both carriers need to be available for recombination, the recombination is limited by the minority carriers or holes. Therefore excitation power, or generation G, dependence of the integrated PL intensity can be given by

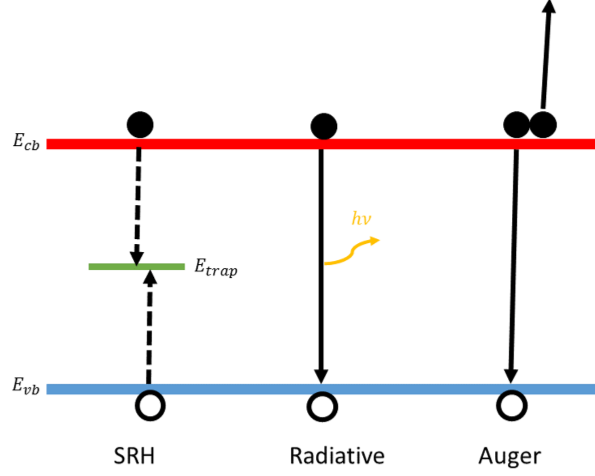

Figure 6: A schematic of the main recombination channels in a semiconductor. The electrons and holes are shown by the closed and open circles respectively and the arrows show the recombination pathways. From left to right, they are the non-radiative Schockly-Read-Hall recombination, the radiative recombination and the e-e-h Auger recombination.

the adjusted ABC-rate model

$$G = Ap + Bpn + Cpn^2 \tag{2.1}$$

in which A, B, C are the Shockley-Read-Hall, the radiative and the Auger recombination coefficients. Furthermore n and p are the electron and hole carrier densities. When exciting above the doping concentration, which is the high excitation regime, the behaviour should be as predicted by Yoo et al. [23]

$$G = A\sqrt{\frac{I_{PL}}{aB}} + \frac{I_{PL}}{a} + C\left(\frac{I_{PL}}{aB}\right)^{3/2} \tag{2.2}$$

where a is a measure for the collection efficiency of the setup. According to this relation, the measured PL intensity should behave according to a power law $I_{PL} \propto P^S$ [24] where P is the excitation density and S the power slope. When shown on a logarithmic scale, this results in a different slope S from $\log(I_{PL}) \propto S \cdot \log(P)$ depending on which recombination is dominant. For SRH recombination this slope is expected to be 2, for radiative recombination it is 1 and 2/3 for Auger. However, from previous work, no signs of Auger behaviour have yet been seen in Hex-SiGe [15]. Therefore we will assume Auger to be negligible in this work.

2.1.2 Lifetime, excitation dependence

The radiative lifetime τ_{rad} is given by [25]

$$\tau_{rad} = \frac{\Delta n}{R_{rad}} \tag{2.3}$$

Where Δn is the injected carrier density and R_{rad} the radiative recombination rate. The radiative rate itself given by

$$R_{rad} = Bnp = B(n_0 + \Delta n)(p_0 + \Delta p) \tag{2.4}$$

Where n_0, p_0 are the equilibrium carriers densities which in this degenerate case mostly originate from the unintentional n-doping $n_0 \ggg p_0$, and $\Delta n = \Delta p$ are the excess carrier densities generated equally by optically pumping the system. Because the material is degenerately n-doped, we will assume little p-doping $\Delta n \gg p_0$. In the low excitation regime, where the injected carrier density is lower than the doping concentration $\Delta n \ll n_0$ but , this lifetime behaves as

$$R_{rad} = Bnp \approx Bn_0 \Delta n \Rightarrow \tau_{rad} = 1/Bn_0 \tag{2.5}$$

which is constant for increasing excitation power. Alternatively, when the high excitation regime ($\Delta n \gg n_0$) is reached, the behaviour changes to

$$R_{rad} = Bnp \approx B\Delta n^2 \Rightarrow \tau_{rad} = 1/B\Delta n \tag{2.6}$$

in which the lifetime starts to decrease with when the excitation power is increased and bigger excess carrier concentrations are induced.

2.1.3 Lifetime, temperature dependence

For the temperature dependence of the PL, the most important contribution originates from thermally activated non-radiative Shockley-Read-Hall traps. The non-radiative SRH lifetime τ_{SRH} of these traps is given by [26]

$$\tau_{SRH} = (\sigma v_{th} N_t)^{-1} \tag{2.7}$$

in which σ is the capture cross section of the trap, v_{th} is the thermal velocity of the carriers and N_t the density of traps in the material. This capture cross section is given by [27]

$$\sigma = \sigma_\infty e^{-\frac{E_{act}}{k_b T}} \tag{2.8}$$

in which σ_∞ is the capture cross section for infinite temperature and E_{act} the activation energy of the trap. While the thermal velocity is defined as

$$v_{th} = \sqrt{\frac{k_b T}{m^*}} \tag{2.9}$$

When the thermal velocity is higher, the carriers can diffuse further before they recombine, increasing the likelihood of being captured by a trap. In the limit of low temperature $k_b T < E_{act}$, the SRH lifetime goes to infinity. Therefore the SRH lifetime will only contribute significantly when the traps have been thermally activated after which the non-radiative lifetime is mostly dominated by the change in thermal velocity.

2.1.4 Intensity, temperature dependence

Using this information, it can be determined how the PL intensity I_{PL} will change as a function of temperature by considering its ratio with I_0 the PL intensity at $0K$. At that temperature negligible non-radiative recombination can be assumed, meaning all recombination is radiative, giving maximum PL intensity. The ratio can be written as the ratio of the radiative recombination rate R_{rad} and the total recombination rate which is the sum of R_{rad} and the non-radiative recombination rate R_{nr}. These recombination rates can be re-expressed in lifetimes as

$$\frac{I_{PL}}{I_0} = \frac{R_{rad}}{R_{rad} + R_{nr}} = \frac{\frac{1}{\tau_{rad}}}{\frac{1}{\tau_{rad}} + \frac{1}{\tau_{nr}}} = \frac{1}{1 + \frac{\tau_{rad}}{\tau_{nr}}} \tag{2.10}$$

in which τ_{rad} and τ_{nr} are the radiative and non-radiative lifetime respectively. It is clear that this ratio is always equal or smaller than unity. Given this relation and assuming τ_{nr} equal to τ_{SRH}, the integrated PL intensity can be rewritten as the Arrhenius function [28]

$$I(T) = \frac{I_0}{1 + R_A e^{-\frac{E_A}{k_b T}}} \tag{2.11}$$

Where $R_A = \frac{\tau_{rad}}{\tau_{(nr,A,0)}}$ is the quenching strength and E_A the activation energy of the non-radiative process. The quenching strength is given as the ratio between the radiative lifetime τ_r and the characteristic non-radiative lifetime of the trap $\tau_{(nr,A,0)}$.

2.1.5 Experimental observation

In measurements we can only observe the effective lifetime given by

$$\frac{1}{\tau_{eff}} = \frac{1}{\tau_{rad}} + \frac{1}{\tau_{SRH}} + \frac{1}{\tau_{Auger}} \tag{2.12}$$

but given this relation we can see that the shortest lifetime should always dominate the observed effective lifetime.

2.2 Lasers

The design of a laser only requires three fundamental components. A resonating cavity to provide the optical feedback, a gain medium to generate spontaneous emission and amplify it by stimulated emission and an energy source called a pump to ensure enough carriers are excited to sustain the amplification. While this sounds like a simple recipe, in practice it is essential that these components are well tuned to create a functioning laser. Therefore in this section we will introduce a model of a laser, afterwards we will introduce the laser conditions for the Fabry-Perot laser and finally we introduce the concept of a photonic crystal and how it can be used to lower the lasing threshold.

To derive the laser equations and conditions, the processes inside a laser need to be evaluated and balanced. This will be done by means of the semiconductor Fabry Perot laser [29] which consists of a gain material placed between two mirrors. To match the introduced hex-SiGe material, the system is assumed to be degenerately n-doped which will be indicated by a partially filled conduction band. The laser structure and the occurring processes for this laser are shown in figure 7. The laser has three primary categories of processes: Excitation, emission and losses. The excitation of the carriers will be provided by a pump laser by using photons with an energy larger than the bandgap energy of the gain material. The higher the pump rate R_p the more free carriers will be available.

To emit light, an electron-hole pair needs to radiatively recombine over the bandgap and generate a photon. For this process, the gain material has two mechanisms: spontaneous emission and stimulated emission. The spontaneous emission is the normal radiative recombination introduced in the previous section, recombining without outside influence at a rate $R_{sp} = \frac{1}{\tau_r}$. However, as spontaneous emission is random, not all emitted photons will couple to the lasing mode, therefore we define β_{sp} as the fraction of spontaneously emitted light that does indeed couple to the lasing mode. Although similar to spontaneous emission, stimulated emis-

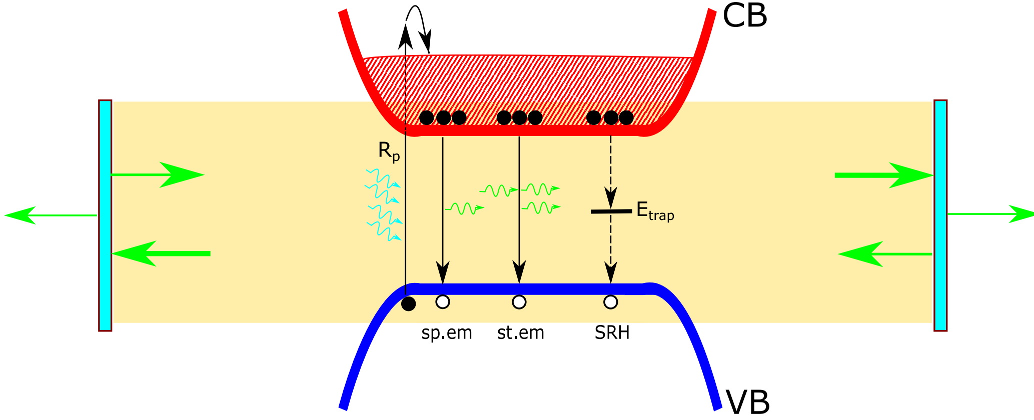

Figure 7: A schematic of the geometry and the internal processes of a Fabry-Perot laser. The semiconductor gain material and optical cavity is shown in yellow with blue mirrors on either end. The valence and conduction band are shown with the absorption or pump process, the spontaneous emission (sp.em) and the stimulated emission (sp.em) process of recombining without or with an incoming photon respectively, carrier loss by SRH recombination and finally the photon loss at the mirrors illustrated by the green arrows. The electrons and holes in each process are indicated by the filled and empty circles.

sion requires an additional component. To get simulated emission, the electron-hole pair needs to interact with an incoming photon to immediately recombine and emit a photon of identical energy and phase. This process is responsible for the optical amplification required in a laser. An important parameter is the gain $G(p)$ as a function of the carrier density $p = P/V$ with P the number of holes inside the gain material and V its volume. This parameter indicates how many electrons-hole pairs a photon can stimulate to recombine per unit of time for a certain carrier density. When this is combined with the amount of photons already in the cavity the total stimulated emission rate is found to be $G(p)N_{ph}$.

Finally, there are two loss mechanisms in a laser: the carrier loss and the cavity loss. The carrier loss is caused by carriers that undergo non-radiative recombination due to SRH traps, which has an associated rate of R_{nr} as discussed in the previous section. On the other hand, there are also losses from photons leaving the cavity, this is called the cavity loss. The main cavity loss for a Fabry-Perot laser is generally the mirror loss. As the mirrors are not perfectly reflective, photons are lost from the cavity in each round trip as some are transmitted instead of reflected. However this is unavoidable as a laser with two perfectly reflective mirrors would not be very useful as no laser beam would be emitted. The mirror loss and any other losses associated with the cavity are summarized in a cavity loss rate $L_{cav}(N_{ph})$ which depends on the number of photons in the cavity N_{ph}.

With all the processes explained, it is now possible to formulate the laser rate equations in terms of the number of photons N_{ph} in the cavity and the number of holes in the gain material P as

$$\begin{aligned} \frac{dP}{dt} &= R_p - G(p)N_{ph} - L_p(P) \\ \frac{dN_{ph}}{dt} &= G(p)N_{ph} - L_{cav}(N_{ph}) + \beta_{sp}R_{sp}(P) \end{aligned} \tag{2.13}$$

Where the total carrier loss $L_p = R_{sp} + R_{nr}$ is given by the sum of the spontaneous emission and non-radiative recombination.

This relation can be generalised by $G(p) = g(p)\Gamma_a$ where the total cavity gain is split into the gain in the active layer only $g(p)$ and the fraction of the photons inside the active layer Γ_a. Additionally it can be re-expressed in terms of lifetimes using equations 2.3 and 2.12 and redefining the cavity loss $L_{cav}(N_{ph}) = \frac{N_{ph}}{\tau_{ph}}$ where τ_{ph} is the characteristic time a photon is trapped inside the cavity [29]

$$\begin{aligned} \frac{dP}{dt} &= R_p - g(p)\Gamma_a N_{ph} - \frac{P}{\tau_p} \\ \frac{dN_{ph}}{dt} &= g(p)\Gamma_a N_{ph} - \frac{N_{ph}}{\tau_{ph}} + \beta_{sp}\frac{P}{\tau_r}. \end{aligned} \tag{2.14}$$

Using the second equation, the importance of the laser cavity can be shown. If the number of photons is assumed constant and the contribution from the spontaneous emission is assumed very small, we trivially find the steady state condition

$$g(p)\Gamma_a = \frac{1}{\tau_{ph}} \tag{2.15}$$

meaning that stimulated emission generation rate should be equal to the photon loss rate which effectively states that each photon in the cavity on average stimulates exactly one electron to recombine during its lifetime in the cavity. If the cavity is improved and the loss reduced, less gain will be required for steady state operation.

2.2.1 Fabry-Perot resonator

Which brings us to the resonator component of the laser design. In this work, two resonator designs are investigated, the simple Fabry-Perot cavity for the single nanowire lasers and a Photonic Crystal cavity for the Photonic band edge laser. For a Fabry-Perot cavity, two main conditions

have to be fulfilled to achieve stable oscillation of light inside the cavity. These two conditions are the resonance condition and the gain condition.

The resonance condition is met when the wavelength of the gain medium exactly fits the cavity as given by [29]

$$\sin(n_r k_0 L) = 0 \tag{2.16}$$

where the n_r is the effective refractive index of the cavity, k_0 is the wavenumber in vacuum and L is the cavity length. The solution to this equation can be written as

$$n_r k_0 L = n\pi \tag{2.17}$$

where n is a positive integer. When now re-expressing the wavenumber in vacuum in terms of the wavelength $k_0 = \frac{2\pi}{\lambda_0}$, the resonance condition is found to be

$$L = n\frac{\lambda_0}{2n_r} \tag{2.18}$$

Because the wavelength in a material is given by $\lambda_n = \frac{\lambda_0}{n_r}$, the length L should be equal to a positive integer times the half-wavelength in the cavity material to achieve resonance. Since the spontaneous emission peak is broad in terms of emitted wavelengths, as shown previously in figure 4, there should always be some resonant wavelength available if the cavity is long enough.

The gain condition states that there is a certain minimum amount of material gain necessary to start lasing. This condition is met when the number of photons lost from the cavity in each round trip is equal to the number of photons added by the gain material due to stimulated emission. The relation for this condition is given by [29]

$$R_1 R_2 e^{g \cdot 2L} = 1 \tag{2.19}$$

where R_1, R_2 are the reflectivities of the two cavity mirrors or end facets, g is the optical power gain coefficient of the cavity and L the length of the cavity. Due to the waveguide nature of the structures that will be introduced in this work, it is necessary to separate the cavity optical power gain coefficient g into

$$g = \Gamma_a g_a - \alpha_i \tag{2.20}$$

where Γ_a is the optical confinement factor of the optical mode inside the gain material, g_a the optical gain coefficient of the gain material and α_i the internal loss of the cavity per unit distance. This optical loss can have many origins, but some examples are scattering from surface roughness,

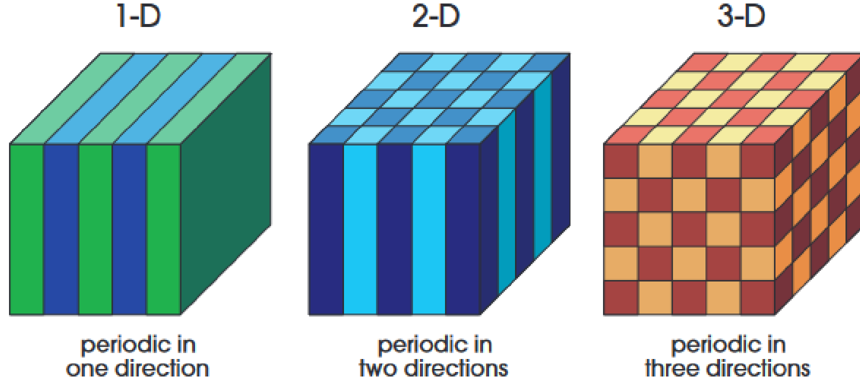

Figure 8: Schematic examples of photonic crystals in one, two and three dimensions. the different refractive index materials are indicated by their different color. Adapted from [31, Ch. 1, Fig. 1].

leakage of light into the substrate or towards infinity or free carrier absorption [30]. When combining these relations, the relation for the threshold gain is found to be

$$\Gamma_a g_a = \alpha_i + \frac{1}{2L}\ln\left(\frac{1}{R_1 R_2}\right) \tag{2.21}$$

where the left-hand side is the threshold gain, α_i the internal cavity loss, and the rightmost term is the mirror loss. When these losses are mitigated, the threshold is reduced, meaning the material will start to lase easier. The cavity reflectivities are important as the reflections facilitate the required optical feedback, but increasing the cavity length is the most effective way of reducing the threshold. The internal losses are often a result of the fabrication process, the geometric, and/or the material properties of the laser structure and are therefore generally difficult to change or improve.

2.2.2 Photonic crystals

Another way to lower the threshold gain is by using a Photonic crystal (PhC). A photonic crystal is a periodic structure of dielectric materials with a periodicity in the order of the wavelength of light. The periodicity can be in one, two or three dimensions, examples of these structures are shown in figure 8.

In a homogeneous medium we can characterise the waves by their magnetic field $\vec{H}_k(r)$

$$\vec{H}_k(r) = \vec{H}_0 e^{i\vec{k}\cdot\vec{r}} \tag{2.22}$$

which is a plane wave with a wave vector $\vec{k}$ at a position $\vec{r}$ with a polarization direction $\vec{H}_0$.

However when a periodic modulation of the refractive index is introduced, for example with a period a in the x direction, the system can no longer be solved by just a plane wave. The plane wave must be modulated by a periodic function with a period equal to this a. This result is known as Bloch's theorem [17, 31]

$$\vec{H}_k(r) = e^{i\vec{k}\cdot\vec{r}}\vec{u}_{\vec{k}}(\vec{r}) \tag{2.23}$$

where the magnetic field $\vec{H}_k(r)$ can be solved by a plane wave with a wave vector $\vec{k}$ at a position $\vec{r}$ modulated by a periodic function $\vec{u}_{\vec{k}}(\vec{r}) = \vec{u}_{\vec{k}}(\vec{r}+\vec{R})$ for all lattice vectors $\vec{R} = \ell a\hat{x}$ where ℓ is an integer, and a the periodicity of the medium.

The photonic bandgap of the photonic crystal is formed because the degeneracy of the even and odd modes is broken. This will be illustrated for an infinite 1D photonic crystal with a unit cell of length a. A third of this unit cell consists of a material with refractive index $n = 2$ in a background of air ($n = 1$), this structure is shown in figure 9a. For a wavelength $\lambda = 2a$ which is twice the crystal period or lattice constant, we get $k = \frac{\pi}{a}$. There are only two ways to center this mode while keeping the unit cell symmetric about its center. Either the field nodes can be positioned in the center of the high, or the low refractive index region. These two cases are shown in also figure 9a with the even mode in blue and the odd mode in orange. When we now take into account the electric-field energy density is given by [31]

$$W = \frac{\epsilon_r \epsilon_0 |E|^2}{8\pi} \tag{2.24}$$

in which $\epsilon_r \approx n^2$ is the relative electric permittivity with its approximate relation to the refractive index n, ϵ_0 the electric permittivity of vacuum and E the electric field. It is found that the energies of these modes are indeed no longer equal. The lower frequency mode stores most of its energy in the high ϵ_r dielectric while the higher frequency mode stores a larger fraction of the energy in the low ϵ_r, this is also visible in figure 9b. Because each wavelength can now have two frequencies depending on the odd- or evenness, instead of one energy in the bulk case, the photonic bandstructure of the system will split and a bandgap is opened. An example bandstructure is shown in figure 10 to show a bandgap opening when changing bulk GaAs into a 50% GaAs/Air multilayer with a period of a, the two band edges $k = \frac{\pi}{a}$ are annotated with a blue or orange circle for the

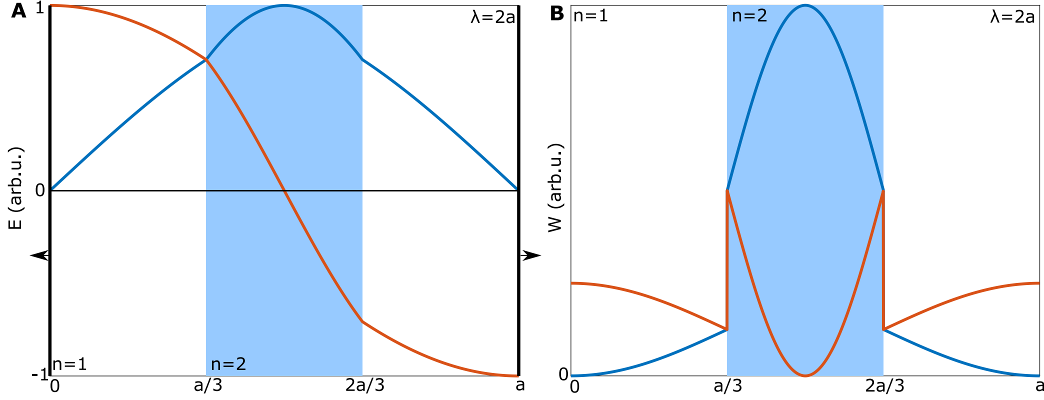

Figure 9: a) The normalised E field distribution for an even (blue) and odd (orange) mode of a $\lambda = 2a$ wavelength in a unit cell of an infinitely periodic multilayer of length a with refractive indices $n = 1, 2$. b) The electric-field energy density W given by equation 2.24.

even and odd mode respectively. These bands that originate are called the Dielectric band for the modes inside the high ϵ_r region, in the example's case the GaAs, and the Air band for the modes inside the low ϵ_r region, which in the example is also air.

The main point of interest for the PhC laser structures investigated in this work is in the bands just around this bandgap. Because when light enters the photonic crystal, the photons are subject to many multiple reflections at the interfaces of the different materials, this makes it difficult for the light to percolate through. For some frequencies, this interference will be so strong that they are not able to propagate in the crystal at all, these exist inside photonic band gap. At the bottom of the air band and at the top of the dielectric band in the right part of figure 10, the bandstructure is almost flat. This means that the group velocity v_g of the light is very low. As it is defined as the slope of the bandstructure as

$$v_g = \frac{\partial \omega}{\partial k} \tag{2.25}$$

where ω is the angular frequency and k the wave vector.

The goal is to create a material in which the electronic band-gap energy is at a very similar energy as the photonic band-edge. The emitted photons are then immediately trapped in the band edge with a very low group velocity, thereby increasing the effective cavity length L, of that mode in the gain material. This will increase gain and lower the lasing threshold[32–37].

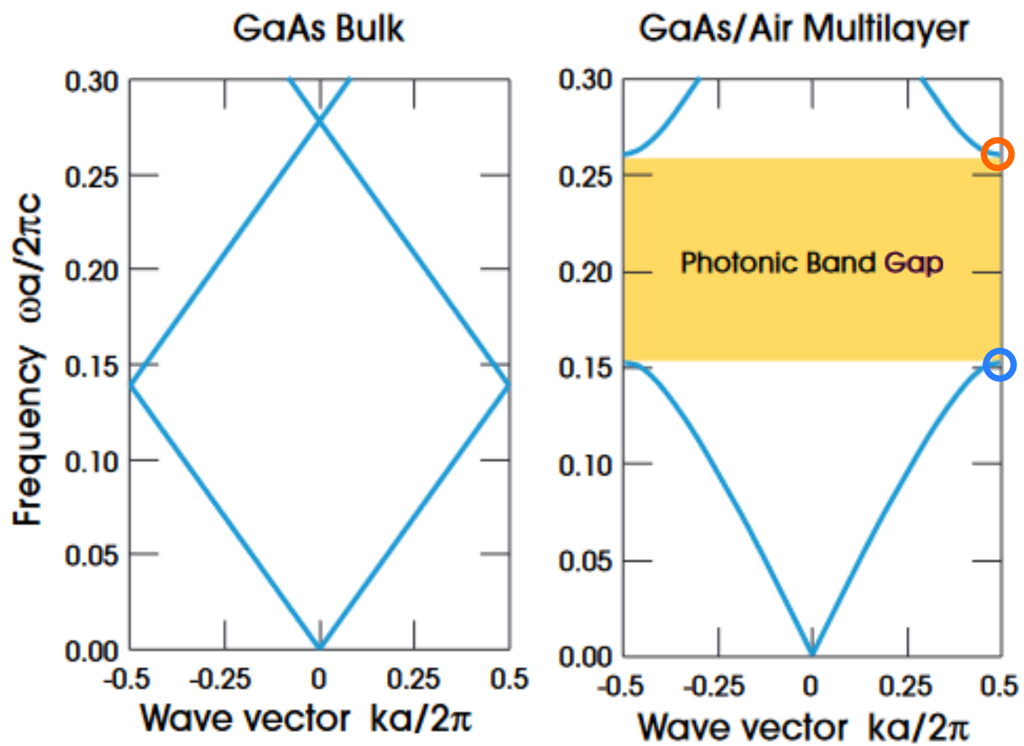

Figure 10: The calculated photonic bandstructures for bulk GaAs $\epsilon_r = 13$ and a GaAs/Air $\epsilon_r = 13, 1$ multilayer of $0.5a$ alternating layers showing the opening of the bandgap when introducing the periodic structure. The positions analogous to the even and odd mode from figure 9 are annotated by the blue and orange circle respectively. Adapted from [31, Ch. 4, Fig. 2].

3 Fabrication

To design any kind of device or structure using hex-SiGe, we need to bring this material into reality by fabricating it. Therefore, first the growth process is introduced and afterwards we discuss an additional gold capping step which will be used in an attempt to improve the nanowire laser structure in chapter 6.

3.1 SiGe growth

The state of the art method to grow hex-SiGe is by growing core/shell nanowires. The hexagonal phase silicon-germanium is obtained by the application of the crystal transfer method[38]. To perform this method, a thin Wurtzite Gallium Arsenide (GaAs) core is grown as a template. When the SiGe shell is then epitaxially grown around the core, the shell takes over the crystal structure from the Wurtzite core. GaAs is chosen as a core material as it is lattice matched to hex-Ge[15, 39]. This decision is made because the focus will be on pure germanium and high germanium content $Si_{1-x}Ge_x$ alloys. A transmission electron microscope image of the result of such crystal transfer is shown in figure 11 for a gallium-phosphide/hex-Si core/shell nanowire which shows that the shell is indeed grown in the crystal structure of the core. Additionally, the core is kept thin to reduce strain and the chance of defects caused by strain in the shell.

Therefore to grow the hex-GaAs/SiGe core/shell nanowires, first the hex-GaAs cores need to be grown. The cores are grown by gold catalysed vapour-liquid-solid[41] (VLS) growth in a MetalOrganic Vapour-Phase Epitaxy (MOVPE) reactor on a GaAs(111)B substrate. To grow the GaAs nanowires in the Wurtzite phase, the conditions need to be thermodynamically favourable inside the reactor. This favourable situation can be engineered by correct tuning of the III-V ratio and the temperature. The Wurtzite phase is stable when the contact angle ϕ of the Au catalyst particle is within the critical angles $55° \leq \phi \leq 125°$ [42–44]. Within these conditions each new layer nucleates at the triple phase line resulting in a Wurtzite layer. The target contact angle during growth is therefore 90° so we are far from either critical value. This stability window of the Wurtzite phase is illustrated in figure 12. The core thickness is determined by the size of the gold particle used as the catalyst.

To then grow the hex-SiGe shell, first the gold particle is etched away to avoid contaminating the shell with gold. Then silicon and germanium precursors are introduced in the reactor to grow the hexagonal radial shell

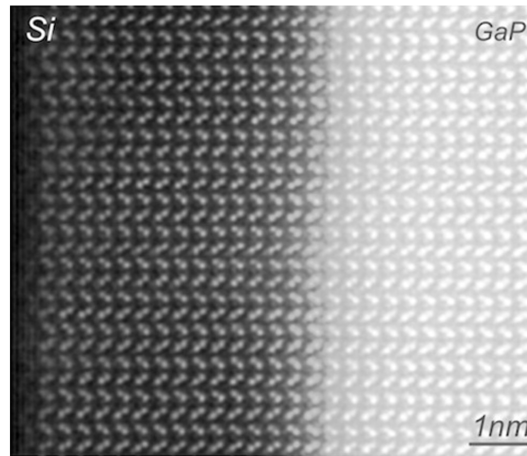

Figure 11: A high-resolution high-angle annular darkfield (HR-HAADF) scanning transmission electron microscopy (STEM) image showing that the epitaxial growth of a silicon shell on a Wurtzite gallium-phosphide (GaP) core will grow in the same crystal structure. Figure adapted from [40, Abstract graphic]

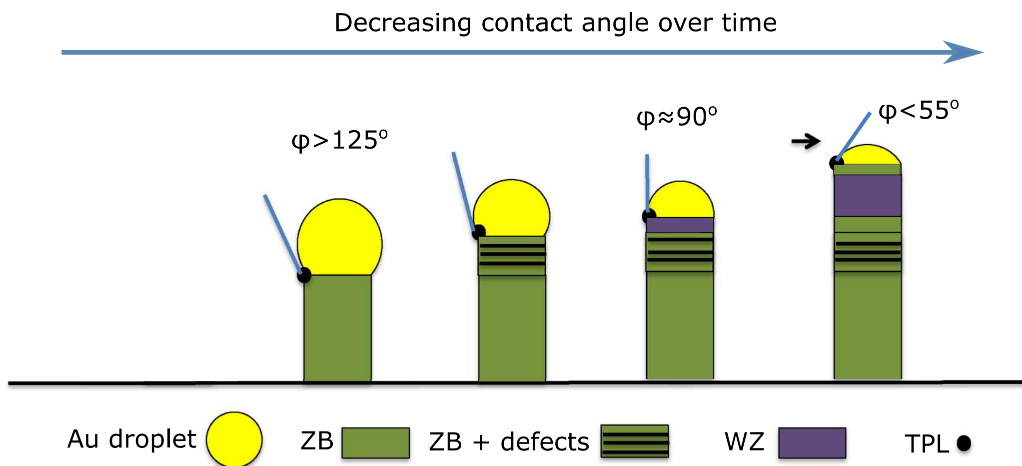

Figure 12: A schematic of the influence of the contact angle ϕ at the triple phase line on the growth of Zinc-Blende (ZB) or Wurtzite (WZ) crystal. Above 125° and below 55° the nanowire grows in the ZB phase, at $\sim 90°$ it grows in the Wurtzite phase and in-between these angles the nanowire can grow both resulting in a defected nanowire. Figure adapted from [45, Fig. 5]

until the shells have reached their required thickness.

The fabrication process is shown schematically in figure 13a-j. To begin the fabrication process, a GaAs (111)B wafer is cleaned using a diluted Ammonia solution to remove the native oxide and any contaminating residues (a) and spin coated with a positive E-Beam resist (b).

This covered wafer is transferred to an Electron-Beam-Lithography (EBL) machine. The machine exposes the resist according to an input layout which, as the resist is positive, softens the resist in these locations (c). Only the softened resist is etched away when the sample is placed in the developing solution creating a hole in the resist for every nanowire growth site (d). On top of the this etched surface an 8nm layer of gold is evaporated using an electron beam evaporator (EBE) (e). To get catalyst droplets, the excess gold on top of the unexposed resist has to be removed. This is done by submersing the sample in a positive resist stripper which will etch away the remaining resist causing the excess gold to fall off the surface (f). After stripping, the sample is placed in an oxygen plasma to burn off any resist residue left behind (g).

With the substrate cleaned and the catalyst particles patterned, the nanowire cores can be grown in the MOVPE reactor. The substrate is placed inside the reactor just below the showerhead on a temperature controlled pedestal. First the GaAs cores of the nanowires are grown (h) keeping in mind the required conditions for the Wurtzite phase. The precursors used in this process are Trimethylgallium or TMGa $Ga(CH_3)_3$ and Trihydridoarsenic or Arsine AsH_3.

Secondly the SiGe shell is grown around the cores to create the hexagonal material by transferring the crystal phase (i). The precursors used for this are Germanium tetrahydride or Germane GeH_4 and Disilane Si_2H_6. As the shell growth is at higher temperature, the part of the GaAs cores and the substrate is evaporated in this process. While this heavily dopes the shell with Arsenic, it also evaporates thin parasitic nanowires that formed from tiny particles of gold that redeposited after stripping the excess gold in solution.

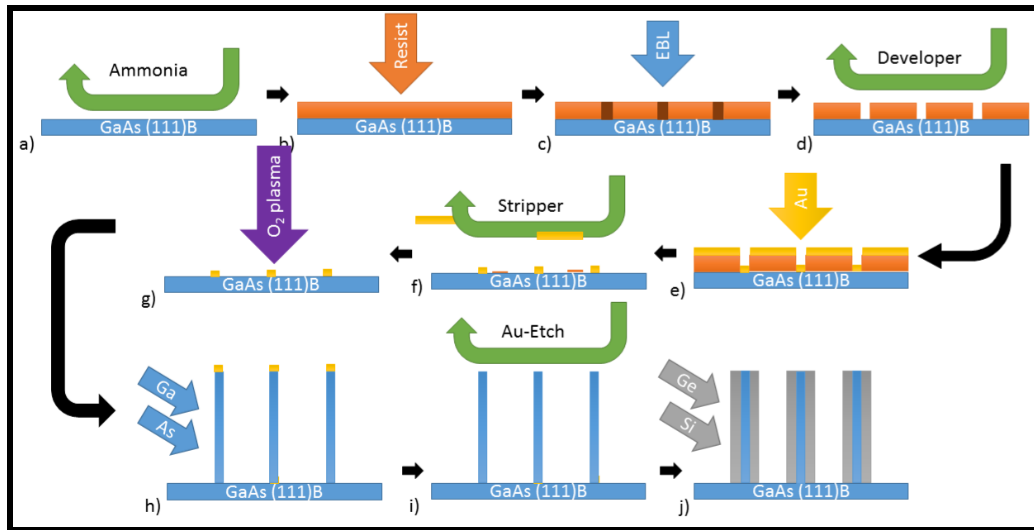

Figure 13: A schematic view of the fabrication steps: a) The wafer is cleaned using a dilute ammonia solution. b) A positive EBL resist is spin-coated. c) The resist is exposed in the EBL. d) The resist is developed. e) An 8nm layer of gold is deposited using an EBE. f) Excess gold is removed by stripping the remaining resist. g) Resist residue is removed with oxygen plasma. h) The GaAs core nanowires are grown in the MOVPE reactor. i) The gold catalyst particles are etched away by a cyanide based solution. j) Germanium shell is grown in the MOVPE reactor.

3.2 Gold capping

For the single nanowire measurements an optional gold-capping step is introduced. From SEM images shown later, it is known that during the shell growth near the tip of the nanowire there is an inverse tapered section and a dome-like structure on top. The schematics for these steps in figure 14 have been adjusted for the existence of this "mushroom top". After the growth of the SiGe shell (a), a sticking layer of $10nm$ Cr/Ti and afterwards a layer of $100nm$ Gold is directionally deposited on the nanowire array (b). This is expected to improve the reflectivity of the mushroomed top facet. The nanowires are then "swiped" or mechanically transferred from the original substrate to another to measure single nanowires (c). The secondary substrate can be $GaAs$, Si/SiO_x or a multi-layer $Si/Cr/Au/SiO_x$ mirror substrate for which the top SiO_x has a thickness of $12nm$.

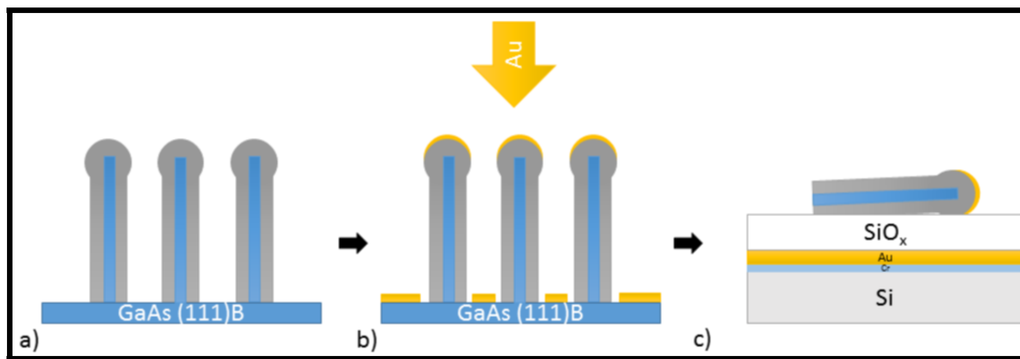

Figure 14: The schematic view of the fabrication steps for the gold capped nanowires: a) The as-grown nanowires are taken. b) Gold is directionally deposited and finally the nanowires were swiped on a multilayer $Si/Cr/Au/SiO_x$ substrate to be measured.

4 Experimental setup

In this section, first the foundation of the Finite Difference Time Domain simulation technique is introduced for the computational investigation of the photonic properties of the photonic crystal. Afterwards the experimental setups are introduced, starting with the Fourier Transform InfraRed (FTIR) spectroscopy and the Time-Resolved photoluminescence (TRPL) setup. The FTIR and the TRPL are used to respectively spectrally and temporally resolve the photoluminescence. Finally the Fourier Plane Imaging microscopy (FPIM) setup and the Scanning Electron Microscope (SEM) are discussed. The FPIM is used to perform a diffraction experiment on the nanowire array samples and the SEM is used to image the nanowires and nanowire arrays.

4.1 Finite Difference Time Domain simulations

The Finite Difference Time Domain (FDTD) simulation technique is based on calculating the propagation of electric and magnetic fields in space and time. The equations solved in this model are given by the Maxwell curl equations,

$$\begin{aligned} \frac{\partial \vec{D}}{\partial t} &= \nabla \times \vec{H} \\ \vec{D}(\omega) &= \epsilon_0 \epsilon_r \vec{E}(\omega) \\ \frac{\partial \vec{H}}{\partial t} &= -\frac{1}{\mu_0} \nabla \times \vec{E} \end{aligned} \tag{4.1}$$

in which $\vec{D}$ is the electric displacement field, $\vec{H}$ is the magnetic field, and $\vec{E}$ the electric field respectively, ϵ_0 and ϵ_r are the vacuum and relative permittivity and μ_0 is the vacuum permeability. In this system it is assumed that the simulated materials are non-magnetic. The benefit of this specific formulation is the absence of material specific parameters in the first and third part of equation 4.1. Only the second part depends on the material and therefore more computationally involved. This step can generally be tackled using signal processing techniques, specifically using Z transforms[46, 47]. These equations are discretized in space using a (non-uniform) Cartesian grid and in time and then solved numerically. The field components E_ν and H_ν with $\nu = x, y, z$ are not centred in the Cartesian grid but staggered in what is called a Yee lattice [48, 49]. One voxel, or cube, of this Yee lattice is shown in figure 15a with the H-field components placed on the cube face centers, while the E-field components are

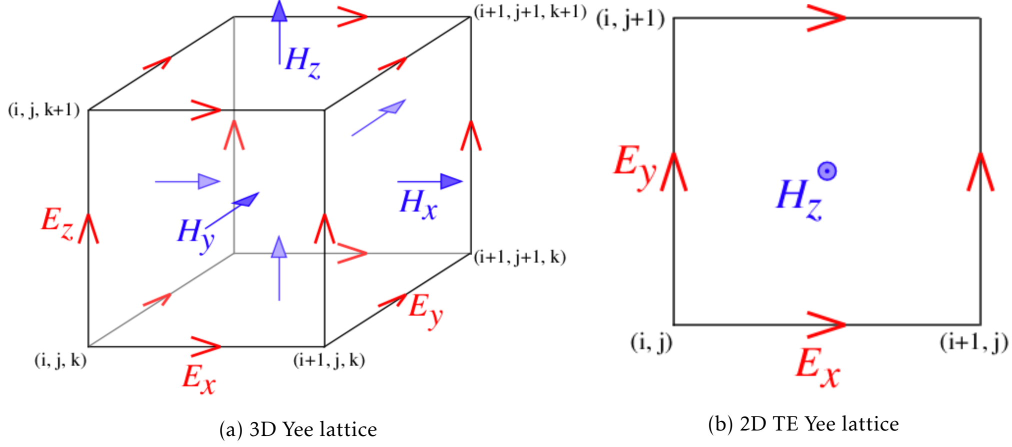

(a) 3D Yee lattice

(b) 2D TE Yee lattice

Figure 15: A schematic of the 3D (a) and 2D TE (b) Yee lattice used to discretize the FDTD simulations spatially as illustrated in [49, Fig. 1-2]. For each grid voxel (a) the E- and H-field components are staggered by placing them on the cube edges and faces respectively. For the 2D TE case (b) only the bottom plane of the voxel with needs to be calculated. To get the 2D TM Yee lattice, only H and E have to be exchanged while keeping the components identical.

placed on the cube edges. When the 2D case is considered in 15b, the voxel can be simplified to an XY-plane with the components E_x, E_y, H_z for TE modes and H_x, H_y, E_z for the TM modes. When a common position of both the E- and H-field is required, the field components are interpolated where necessary.

Now the simulation volume is discussed, it is important to define what happens at the boundaries of this simulation volume. For the upcoming simulations two boundary conditions are used: The Bloch boundary conditions and the Perfectly Matched Layer (PML).

4.1.1 Bloch boundary conditions

When simulating a (quasi) infinite periodic structure it is generally sufficient to simulate one unit-cell of the periodic structure and impose a form of periodic boundary conditions in the direction of the periodicity. The Bloch boundary condition (Bloch BC) is a generalised form of periodic boundary conditions.

$$\begin{aligned} \vec{E}_{x_{min}} &= e^{-ia_x\vec{k}_{bloch}}\vec{E}_{x_{max}} \\ \vec{E}_{x_{max}} &= e^{-ia_x\vec{k}_{bloch}}\vec{E}_{x_{min}} \end{aligned} \tag{4.2}$$

This is important when the light enters the simulation at an angle. The structure is periodic, but the fields are periodic except for a phase shift

due to the extra travel-distance from the angle. Additionally this is important while working with Bloch waves for photonic crystals. By manually setting the $\vec{k}_{bloch}$ it is possible to filter the modes with a certain periodicity of the plane-wave. This is required to calculate the band-structure and an example of this filtering process is shown in figure 16 for two wavelengths and phase shifts when no structure is present inside the unit cell. When a wave crosses the unit cell boundary, the phase shift is applied and the wave is re-introduced at the other side of the unit cell. The phase shifted wave then interferes with itself destructively unless the wave is resonant with the phase shift applied at the boundary thereby filtering the modes.

When a dielectric structure is then introduced, the effective cavity length is increased. The refractive index n reduces the propagation velocity from the speed of light c to $\frac{c}{n}$ with n which compresses the wavelength from the vacuum wavelength λ_0 to $\lambda = \frac{\lambda_0}{n}$ when inside the material. Compared to vacuum, longer wavelengths can therefore already become resonant, meaning that a resonant mode that exists mainly inside the dielectric structure should have a lower energy.

By varying $\vec{k}_{bloch}$ from 0 to 0.5 in units of $\frac{2\pi}{a}$, with a the lattice constant, plane-waves are considered with a periodicity of many unit cells to just 1 unit cell[17]. Wavelengths smaller then $\lambda = 2a, \vec{k} = \frac{\pi}{a}$ are not possible due to the Nyquist frequency. The periodic structure is "sampling" the wave as it passes through. A shorter wave therefore must be first shifted back into the 1st Brillouin zone to an equivalent k by adding or subtracting a multiple of $\frac{2\pi}{a}$ until the wave is back in the range $-\frac{\pi}{a} \geq \vec{k}_{bloch} \geq \frac{\pi}{a}$. [17] It is only necessary to evaluate the positive half of this range, as the left, or right travelling waves give the same solution.

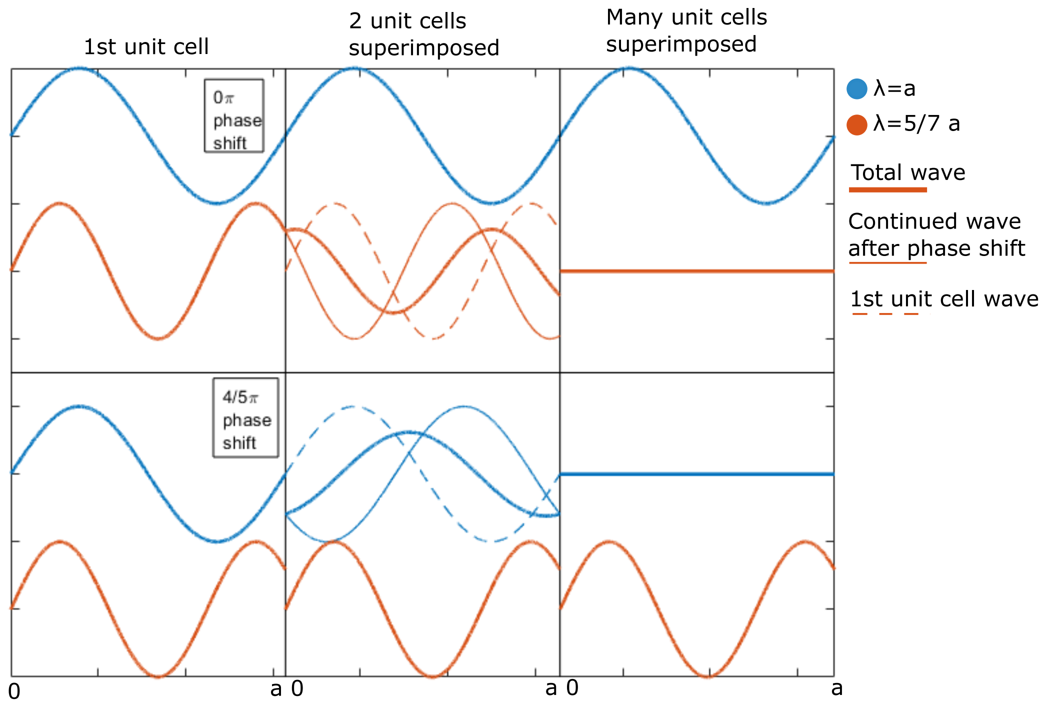

Figure 16: A schematic view of the wavelength filtering by applying the Bloch BC on a 1D unit cell of vacuum for 2 different wavelengths. When no phase shift is introduced (top), the blue wave with the wavelength matching the cavity interferes constructively. The orange wave however has a phase mismatch when the wave is reintroduced (thin line) in the unit cell and interferes with the original wave (dashed line). The resulting wave (Thick line) shows reduced amplitude. When this process continues for many unit cells, the wave disappears. The opposite is true when a phase shift of $\frac{4}{5}\pi$ is now applied (bottom) to the field before reintroducing the waves. The first wave now interferes destructively with itself, while the second wave interferes constructively because of the phase shift. Therefore the phase shift can be used to filter only the wavelengths with a specific periodicity.

4.1.2 Perfectly Matched Layer boundary condition

To simulate (artificial) free-space an absorbing boundary is required. The Perfectly Matched Layer boundary condition is the go-to implementation of such behaviour. In the PML layer the Maxwell equations are modified using complex stretched coordinates by changing the ∇-operator to be

$$\tilde{\nabla} = \frac{1}{s_x}\frac{\partial}{\partial x}\hat{x} + \frac{1}{s_y}\frac{\partial}{\partial y}\hat{y} + \frac{1}{s_z}\frac{\partial}{\partial z}\hat{z} \tag{4.3}$$

where $s_\nu, \nu = x, y, z$ are the stretched coordinate metric coefficients. These coefficients are given by the dispersive function

$$s_\nu = \kappa_\nu + \frac{\sigma_\nu}{a_\nu + i\omega\epsilon_0}, \nu = x, y, z \tag{4.4}$$

assuming a_ν, κ_ν and σ_ν are positive real and potentially 1D functions depending on their respective ν-axis.[50] Forcing the exponential decay of the fields in the PML and thereby simulating infinitely long space. [51, 52] While PML is not completely reflection free, in general the reflections are negligible compared to the actual signal and can often be resolved by tuning the PML settings.

4.2 Fourier transform infrared spectroscopy based photo-luminescence

To spectrally resolve the nanowire emission, a Fourier Transform Infrared or FTIR setup is used to perform macro photo-luminescence (PL) on standing nanowire. This measurement is therefore an ensemble measurement of many wires on the substrate. For these experiments the sample is cooled to 4K in a cryostat using liquid helium. The sample is then excited optically with a chopped continuous wave 976nm laser. The beam is modulated at $35kHz$ to enable the use of a lock-in amplifier to get increased signal to noise ratio. The laser power can be tuned with a continuously variable neutral density filter or powerwheel. A mirror with a hole is used to couple the laser into the setup to avoid the need for a beamsplitter. To both focus the laser on the sample and collect subsequent PL a parabolic mirror is used. This method gives a $\sim 45\mu m$ spot size, allowing large amounts of wires to be measured at once increasing the signal. The collected light is then filtered using a germanium filter to remove the excitation laser reflection and the combination of the Michelson interferometer, the detector (InGaAs/MCT) and the lockin amplifier is used to record an interferogram. The interferogram is phase corrected by the Mertz[53] method to correct for any imperfections in the alignment of the interferometer. The spectrum can then be acquired by the Fourier transform using the Wiener–Khinchin theorem[54, 55]. For most SiGe samples, the InGaAs detector is chosen because of its higher sensitivity, while (close to) pure germanium samples require the MCT detector because their wavelength is too long for the InGaAs detector to measure.

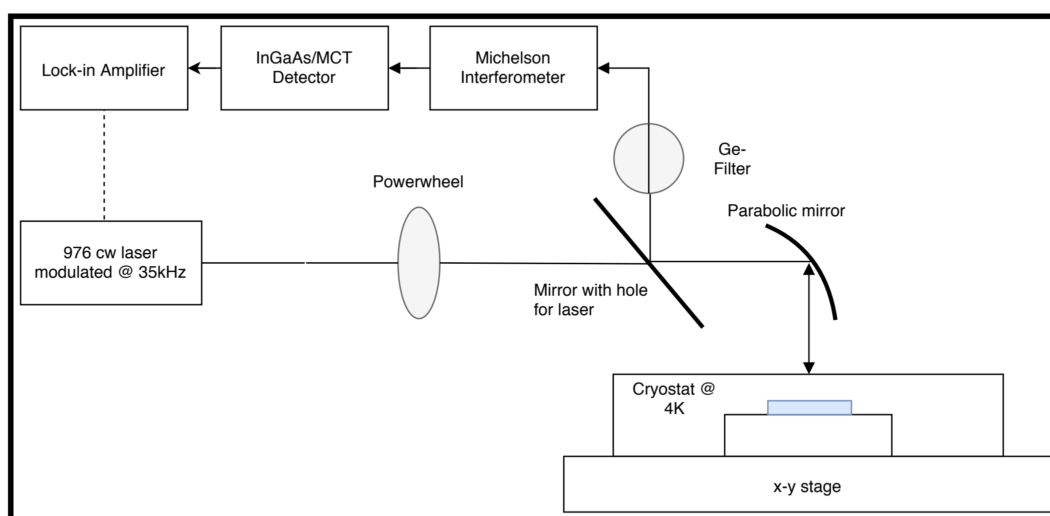

Figure 17: A schematic drawing of a Fourier transform infrared setup. The laser beam is modulated and attenuated, and then focussed on the setup using a parabolic mirror to excite the sample. The subsequently emitted light is collected by the parabolic mirror. The laser reflection is removed by a Ge-filter. The combination of a Michelson interferometer, a detector and a lock-in amplifier is used to extract the PL signal from the laser modulation as a function of the interferometer mirror position building an interferogram. The spectrum is then calculated by applying the Fourier transform.

4.3 Time-resolved photo-luminescence

This setup is used to temporally resolve the photo luminescence, giving insight into the PL-intensity, the decay processes and the accompanying characteristic lifetimes. The main parts of this setup are a femtosecond pulse laser (*NKT photonics Onefive ORIGAMI 10*), a single photon detector, and a time correlator. A schematic view of the signal paths is shown in figure 18.

The measurement is started by the laser sending out a laser pulse and simultaneously starting the clock on the time correlator. The intensity of this pulse can be adjusted by sliding in step variable ND filters and further fine-tuned by a continuously variable filterwheel or powerwheel.

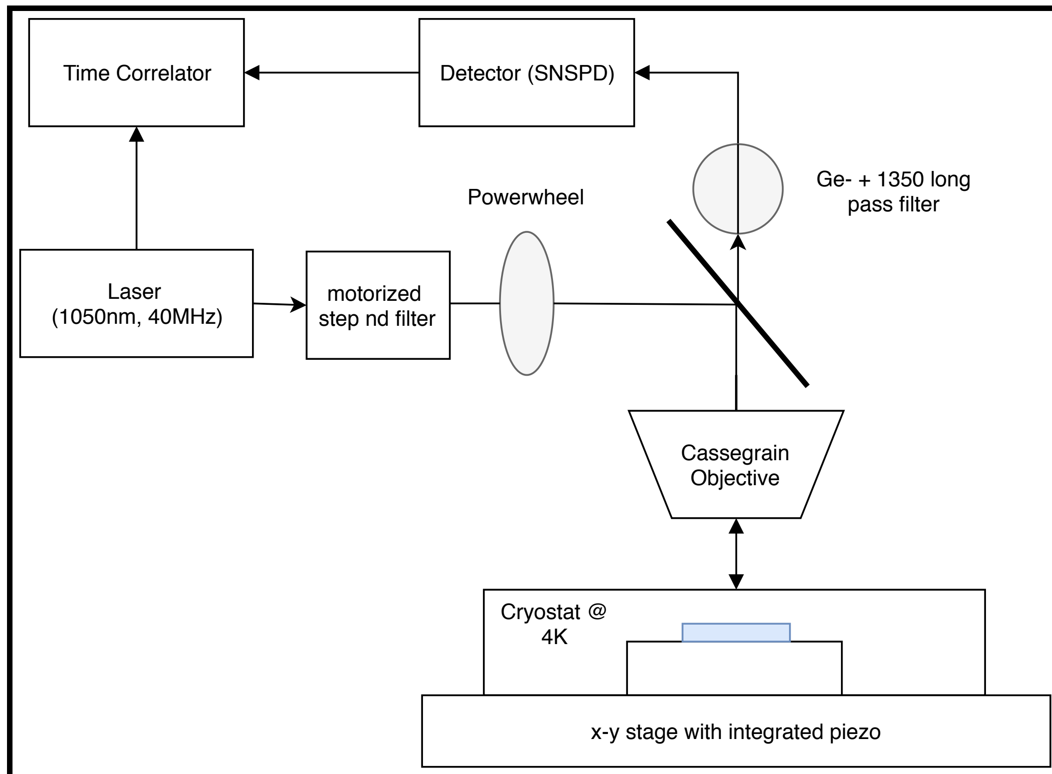

Figure 18: A schematic view of the Time resolved PL setup. The laser pulse is attenuated to a maximum with the powerwheel and can be automatically changed using the motorized linear step ND filters. The sample is then exited by this pulse by focussing it using a Cassegrain objective. The emission is then collected by the objective, filtered to remove any reflection of the laser pulse and measured using the Superconducting Nanowire Single Photon Detector which measures the first incoming photon. The Time correlator finally constructs a histogram of the time delay between the laser emitting the pulse and the SNSPD measuring the first incoming photon.

This laser pulse then excites the sample through the reflective objective, which subsequently luminesces. The emitted light is then collimated by the objective and observed by the superconducting nanowire single photon detector (SNSPD) which then signals the time correlator to stop the clock. Filters are used here to prevent the laser reflection from reaching the detector. The time correlator finally records the time delay between the laser departing and the first photon arriving. This measurement is then repeated at high frequency ($40.006MHz$) and a histogram is generated in the form of counts binned per time delay with a resolution of $4ps$. This histogram can afterwards be integrated to get a total PL intensity and fitted with a single exponential to do lifetime analysis. The objective used is an 36X reflective objective with an estimated transmission of 66% through the objective of the excitation power. The spot-size is estimated to be 4µm, therefore the excitation area is $12.6\mu m^2$ or $1.26\times10^{-7}cm^2$ In this work, the focus is on evaluating the integrated PL intensity and the temporal behaviour of swiped nanowires as a function of excitation power.

4.4 Fourier Plane Imaging Microscopy

A diffraction experiment is conducted using Fourier Plane Imaging Microscopy. The nanowire arrays are used as a small grating, to see if the nanowire arrays are regular enough to show coherent interference.

The maximum intensity angles of the diffracted light are given by Bragg's law:

$$2d\sin\theta_m = n\lambda \tag{4.5}$$

with d the length of the spatial periodicity of the structure, usually a grating, λ the incident wavelength, n an integer denoting the order of the diffraction, and θ_m the angle of maximum intensity [56]. A Fourier Plane Imaging Microscope (FPIM) works by focussing a parallel beam under a certain angle on a single spot on the back focal plane, effectively performing the Fourier transform of the periodic structure. A ray trace of this process is shown in figure 19. In FPIM, a sample is placed in focus of a lens or objective of focal length f. At the same distance f behind the lens, the Fourier tranformed image is projected on the back focal plane. A second, larger, lens of the same focal length f is then placed at $2f$ behind the BFP to re-image the BFP on a CCD camera another $2f$ distance behind this second lens. The continuous wave probe laser is introduced into the objective by using a beam-splitter and can be moved to excite the sample at the desired angle. In the performed measurements only a normal incidence was used.

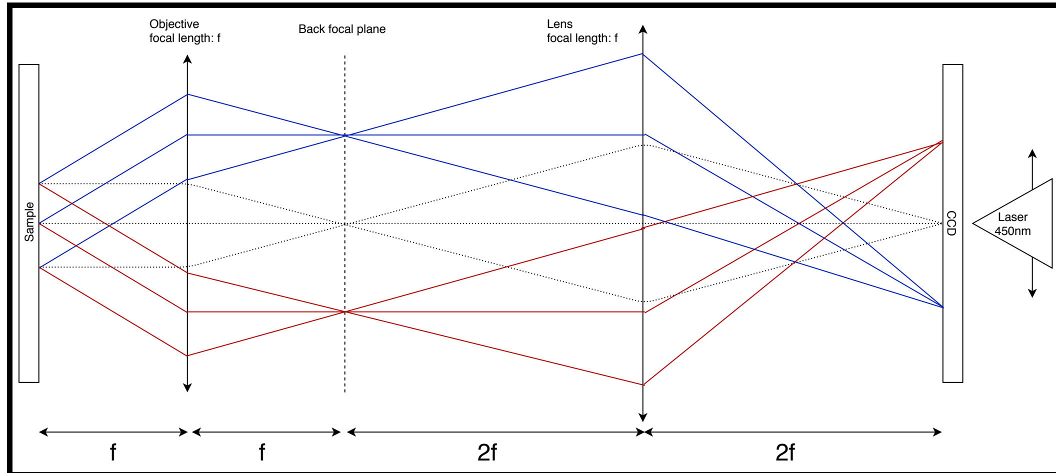

Figure 19: A schematic ray trace of the Fourier Plane Imaging Microscope. The sample is illuminated by a $450nm$ CW laser at normal incidence. The diffracted light is collected by the objective and parallel beams are focussed to a single point on the Back Focal Plane, effectively Fourier transforming the image. This BFP is then refocussed using a second lens of the same focal length but at twice the distance and imaged using a CCD camera.

4.5 Scanning electron microscope

The nanowires are too small to make images using an optical microscope and see anything other than their location because of the diffraction limit. Therefore to make detailed images of these nanowires, after growth or measurements, a Scanning Electron Microscope or SEM is used. Unlike their optical cousins they are not hindered by the diffraction limit as the de Broglie wavelength of electrons is much smaller than the wavelength of optical photons. For a typical $10kV$ SEM operating voltage, the wavelength of the electron is $\lambda_e = 12.2pm$ which is much smaller than visible light. A schematic of a SEM is shown in figure 20. The SEM takes an image shooting a focussed electron beam at the sample. The primary electrons from the focussed beam kick out electrons from their orbit in the sample material. These emitted secondary electrons are then detected by the detector. This process is repeated while scanning across the sample surface in a raster pattern resulting in a space-intensity map which can be converted to a monochrome image showing the sample surface [57, 58]. This process takes place in a vacuum, and is generally only used on cores, or after the SiGe samples have been measured as the electron beam can potentially be damaging the nanowires.

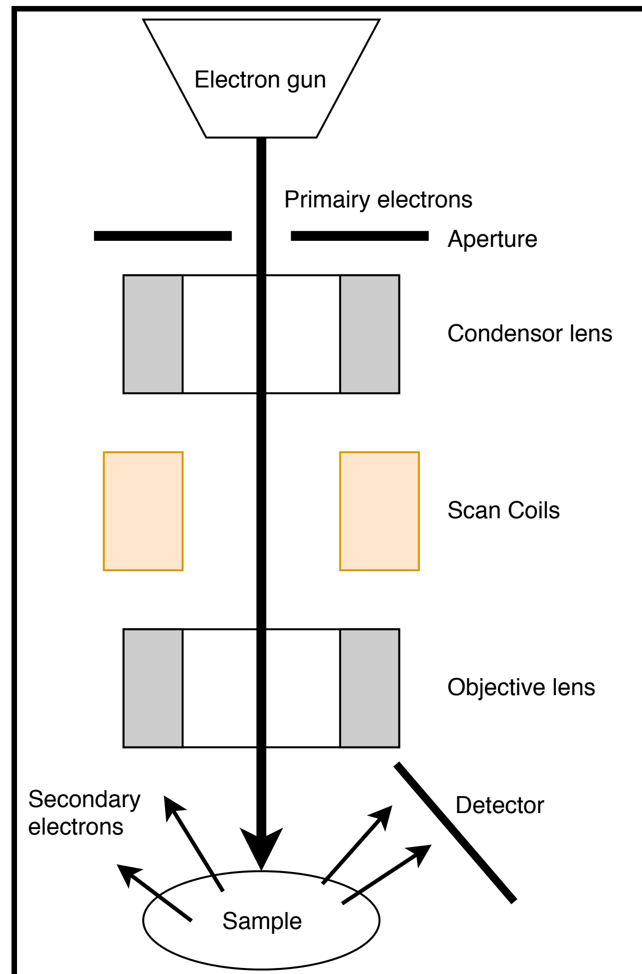

Figure 20: A schematic drawing of an Scanning Electron Microscope. The electron beam is generated by an electron gun and the final beam size is controlled by the aperture. This beam is converged by the condenser lens and raster scanned over the sample using the scanning coils. Finally the objective lens focuses the beam on the sample. The primary electrons kick the sample's electrons from their orbit. These emitted secondary electrons are measured by the detector. This intensity as a function of the position is then translated to an image.

5 Photonic band edge laser

As explained in chapter 1.1, hexagonal germanium can currently only be grown as core-shell nanowires. Early nanowires were too short and too thin to be considered for single nanowire lasing, therefore the obvious choice is to introduce a distributed laser design for gain enhancement. First the concept of the photonic band edge laser is introduced together with the simulation method used to investigate and design these structures. The design parameters are then evaluated numerically by simulations. Using this information a design is proposed for fabrication. Finally this design is evaluated for photonic properties using FPIM.

5.1 Introduction

The photonic band edge laser is a distributed gain laser design that evolved in multiple stages from the Fabry-Perot cavity laser. Figure 21 illustrates these evolutionary steps in the form of schematic laser designs.

The grandfather of all lasers is the simple Fabry-Perot laser [29, 59]. In these lasers the cavity is created by placing a reflector at both sides of a linear cavity as shown in (A). Many Fabry-Perot lasers use mirrors on both sides of a cavity with the gain medium in the center. Alternatively, for semiconductor lasers, the gain medium is incorporated in a waveguide and the cleaved end-facets of the waveguide function as reflecting surfaces.

This concept can be refined by exchanging one or more of the mirrors for Distributed Bragg Reflectors (DBRs) shown in (B). A DBR is constructed by a periodic modulation of the refractive index, specifically a $\frac{\lambda}{4}$ period. Due to this specific period, reflections of the design wavelength λ interfere constructively and the light is not allowed to permeate though the DBR, while other wavelengths are transmitted. The higher the refractive index contrast, the fewer layers are required because the Fresnel reflection of each layer is stronger as given by

$$R = \left| \frac{n1 - n2}{n1 + n2} \right|^2 \tag{5.1}$$

for normal incidence with $n1$ and $n2$ the refractive indices of the two materials[60]. While the mirrors in a Fabry-Perot laser are generally reflective for a broad range of wavelengths, a DBR is reflective for a much more narrow wavelength range around the design wavelength. Because of this property a DBR can be a real single mode laser as harmonics are not reflected.[29]

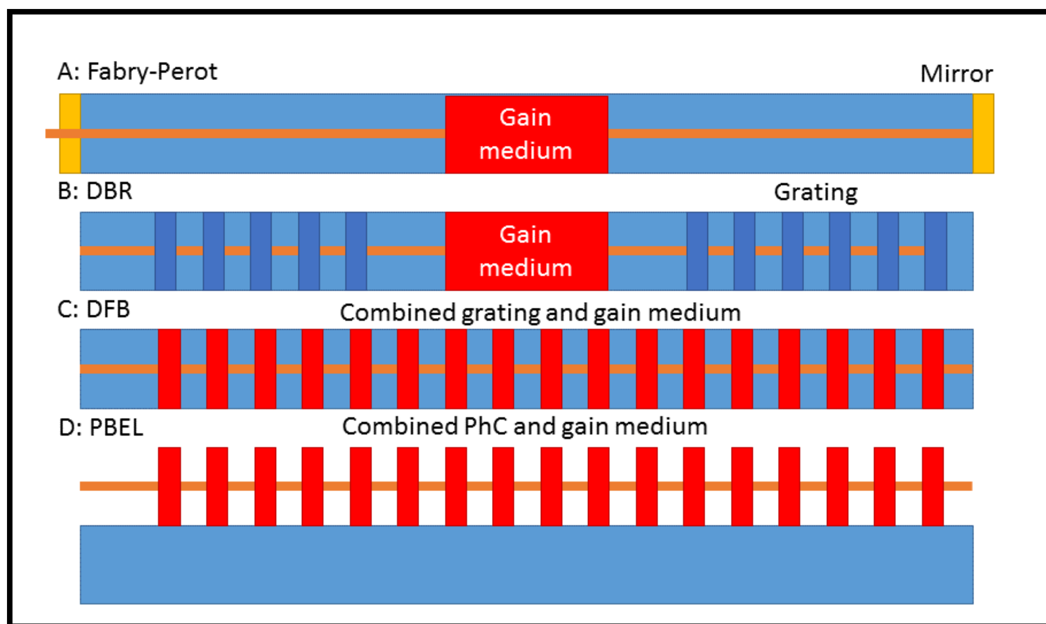

Figure 21: A schematic drawing of four different laser designs. a) The fabry-Perot cavity laser using conventional mirrors. b) The Distributed Bragg Reflector laser that uses alternating layers with a refractive index contrast (DBR) instead of mirrors. c) The Distributed FeedBack (DFB) laser in which the gain material is distributed over the DBR as one of the two materials. d) The nanowire Photonic Band Edge Laser (PBEL) which specifically tunes the DFB with low group velocity photonic crystal properties.

If the gain medium and the surrounding waveguide have sufficient refractive index contrast it is possible to use the gain medium as one of the two materials in the DBR. When the gain medium is distributed in this way (C), the resonator is called a Distributed FeedBack cavity or DFB [29].

A special case of the DFB is found when the cavity is engineered such that the emission energy matches the photonic band-edge energy. At the Photonic band edge, the group velocity of the lasing mode is greatly reduced, therefore the photon-material interaction and the effective cavity length are increased leading to gain enhancement. The photonic band-edge laser (PBEL) is named after exploiting this photonic effect. In this section we will introduce a specific variant of this structure: the 1D nanowire array PBEL (D). For this variant, the photonic crystal is constructed as line of equally spaced hex-Ge or hex-SiGe nanowires in air on a GaAs substrate. For a PBEL, the refractive index of the gain medium is essential and especially its contrast with the background medium. Higher refractive index contrast means stronger confinement of light within the structure, less losses, stronger Bragg reflections, and therefore a lower threshold gain [32, 61].

5.2 Simulation setup

To simulate the proposed PBEL devices using FDTD, the software packages *Lumerical MODE Solutions 2019b r6* and *Lumerical FDTD Solutions 2019b r6* are used. As the chosen simulation geometry we consider the state-of-the-art as-grown nanowires as shown in chapter 3. However due to geometry limitations, a few geometrical assumptions or simplifications are required. Primarily the nanowires are assumed to have no tapering at either the bottom or the top, and the top of the nanowire is assumed flat. Additionally it is assumed that crystal defects do not change the photonic properties so the properties are uniform across the wire. For the array of wires, the absence of any disorder in the nanowire position along the array is assumed. An excerpt of the structure is shown in figure 22. Finally, for computational efficiency, we assume an infinite array of nanowires so periodic Bloch boundary conditions are valid and only one unit-cell needs to be simulated. This assumption generally holds if the fabricated design has enough periods. As a (conservative) rule of thumb ”Enough periods” is defined to be 20 periods. For high refractive index contrast cavities even fewer periods can be sufficient [62–64].

To simulate the dielectric materials, we need material models for the refractive index. For the substrate and the nanowire cores, the GaAs model as defined by Palik [65] is used. On the other hand, the models for the hex-

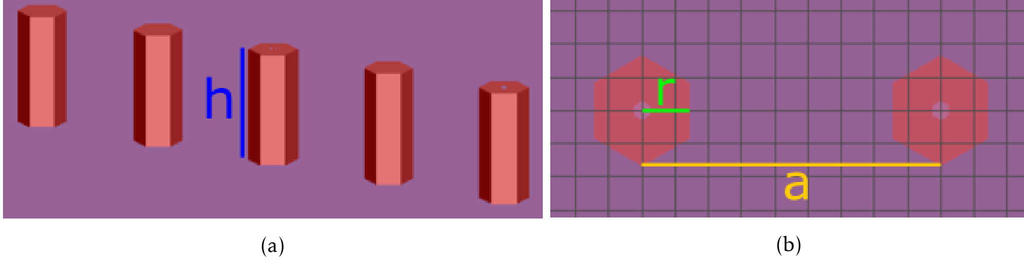

(a) (b)

Figure 22: The perspective (a) and top (b) views of the simulation layout of the GaAs/SiGe Core/Shell nanowires on a GaAs substrate. The GaAs substrate and cores are coloured purple while the SiGe shell is coloured red. The defined design parameters are annotated, nanowire height h, the total nanowire radius or apothem r and the center-to-center pitch a, the GaAs core diameter is fixed to $50nm$.

Ge and hex-SiGe nanowire shells are provided by our collaborators from Jena. These models are shown in appendix B.

From the top view schematic of this structure, figure 23, the simulation geometry (A) is clearer. The propagation direction is set in-plane in the x direction as indicated by the arrow, leveraging the Bloch boundary conditions as shown by the blue bars on the left and right side of the simulation volume. Perpendicular to this direction a Perfectly Matched Layer (PML) is used to absorb any light not travelling in the direction of the propagation, that is out the sides (yellow striped region) and out the top (not shown) to simulate the free-space. For the boundary inside the substrate, the PML is also used, as the substrate is assumed to be thick and any light travelling in too deep is considered to be lost for the photonic structure. Light is inserted into the simulation using many randomly placed dipole sources (B). If the dipoles where placed in a "nice" pattern, there is the risk of failing to properly excite certain modes by only exciting in field-nodes. This randomization in position is a simple way to guarantee the modes are excited properly. A spectrum is generated by the software within the requested limits by generating a time signal using a (chirped) sine in a Gaussian envelope

$$I_{signal}(t) = \sin(\phi_x(t)) * \exp\left(-\frac{(t-t_{offset})^2}{\left(\frac{t_{pulselength}}{2\sqrt{\ln(2)}}\right)^2}\right) \tag{5.2}$$
$$\phi_{standard}(t) = -2\pi f_{center} * (t - t_{offset})$$
$$\phi_{broadband}(t) = a + bt + c\sin(dt)$$

where t is the simulation time, t_{offset} the delay after the simulation be-

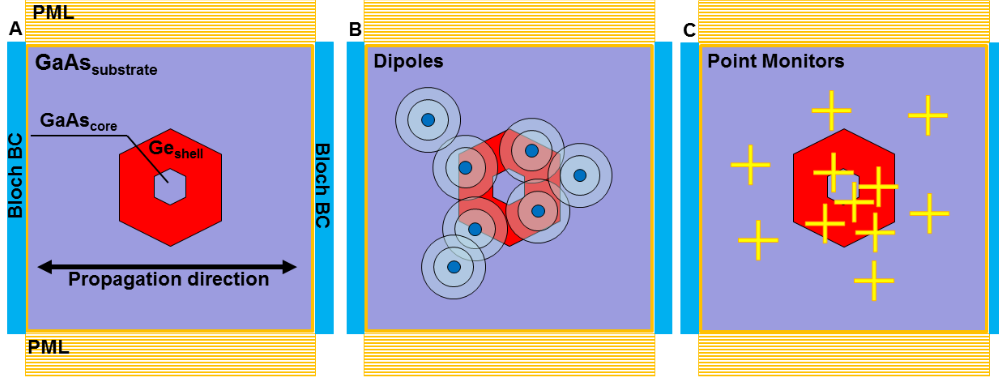

Figure 23: A schematic top-view drawing of the simulation components. a) The simulation volume and geometry showing the GaAs/SiGe core/Shell nanowire on the GaAs substrate. The propagation is chosen to be along the X direction, therefore the Bloch boundary condition is applied in this direction and PML for the perpendicular direction. b) The dipoles are placed into the simulation randomly to exite all modes in the simulated structure. c) The point field monitors are also placed randomly and are used to record the time signal of the E-field components.

gins of envelope center and $t_{pulselength}$ the length of the pulse. These times are given in femtoseconds. For "narrowband" simulations $\phi_x(t) = \phi_{standard}(t)$ is used with f_{center} the center frequency of the pulse in Hz. The $\phi_{broadband}(t)$ function is more complicated and used for the more useful "Broadband" simulation. In this case, the carrier envelope of $I_singnal(t)$ is the same, but the sine component is now chirped by setting $\phi_x(t) = \phi_{broadband}(t)$. The chirp in the sine of $I_singnal(t)$ is caused by the modulation of the frequency by the $c\sin(dt)$ component of $\phi_{broadband}(t)$. The exact determination of the a, b, c, d coefficients is kept proprietary [66, 67]. By Fourier transforming this time signal, the spectrum is then determined. An example of such a chirped pulse and spectrum pair is shown in figure 24. A broader spectrum shortens the pulse, meaning the simulation can be shortened, but care must be taken that enough energy is injected into each frequency to get a reliable response.

To get the resulting photonic bandstructure the point monitors (C) are inserted in the simulation which record the Electric field as a function of time. These point monitors are again placed randomly, for the same reason as the dipoles, to not miss any mode due to accidentally only sampling field nodes. To get the complete photonic bandstructure from the moni-

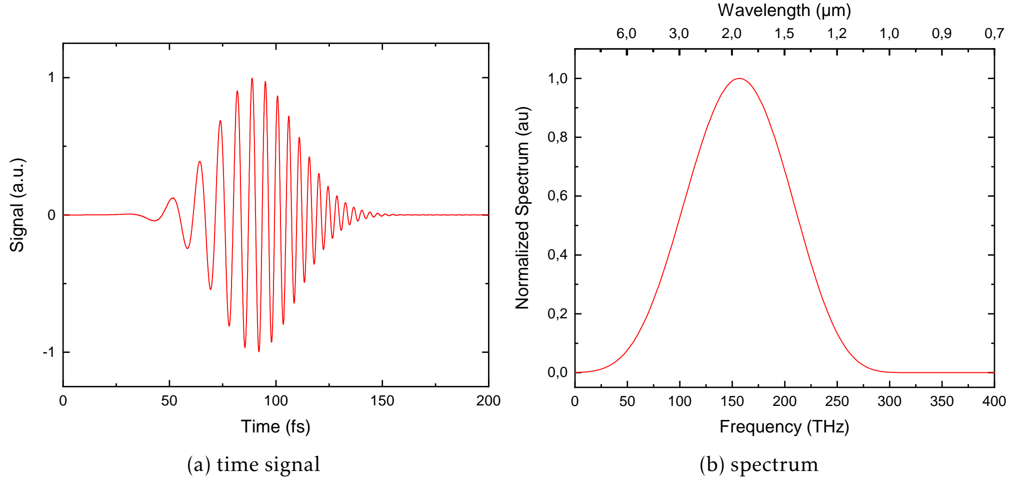

(a) time signal

(b) spectrum

Figure 24: An example chirped sine wave excitation wave (a) that a dipole could use to introduce light into the time-domain simulation and its corresponding frequency-domain spectrum (b) calculated by applying the Fourier transform to (a).

tors the time-domain data is processed using

$$I_{bandstructure} = \sum_{monitors} \sum_{i=x,y,z} \left| \mathcal{Z}\left(N\left(t, t_{center}, t_{width}\right) \cdot E_i\left(t\right)\right) \right|^2 \tag{5.3}$$

where $E_i, i = x, y, z$ is the field component at the position of the monitor multiplied with $N\left(t, t_{center}, t_{width}\right)$, a Gaussian apodization function to remove the startup effects caused by the dipole excitation and any end effects for each $k_b loch$. The power-spectrum is then calculated by the absolute square of $\mathcal{Z}$ which is the chirp Z-transform, which is a generalized form of the discrete-time Fourier Transform with the ability to specify the bandwidth so the FFT is computed only for frequencies that are actually inject by the dipoles. This power-spectrum can be considered as a local bandstructure at that position, by summing all monitors the total bandstructure is constructed. From this result, the position of the bands can be found as regions with a significantly higher resulting values relative to the background. However, as the bandstructure is the sum of many monitors, some modes will just coincidentally ”hit” more monitors than other, for example, better confined modes. Therefore it should be noted that the magnitude **cannot** be used to intercompare the bands for anything except their location.

In a photonic crystal there can be two types of optical mode, the Transversal Electric (TE) mode and the Transverse Magnetic (TM) mode. The TE mode is characterised by the non-zero E_x, E_y, H_z field components and is

polarized perpendicular to the nanowires. For the TM mode the E and H are swapped, it has non-zero H_x, H_y, E_z components and has a polarization parallel to the nanowires [68]. For the structures like the simulated structure, a line of dielectric rods in air, it is known that the photonic bandgap will open for Transverse Magnetic (TM) modes [31]. Therefore the dipoles can be oriented purely in the z-direction to specifically excite the TM modes. These modes can then be further isolated by exploiting the E-field symmetry of the TM modes in the (xz) plane [31]. Incidentally this assumption also reduces the computational requirements. Because the fields are symmetric, only half of the volume (positive y) needs to be calculated.

With the defined simulation, it is now possible to numerically investigate the parameter space of the photonic crystal design.

5.3 Simulation results

To be able to determine the PBEL design parameters, the photonic properties of the structure need to be evaluated. First, we will introduce the bandstructure of these structures by simulating the structure with $2r_{core} = 50nm$ with r_{core} the incircle radius or apothem of the core, a total nanowire incircle radius $r = r_{total} = 0.16\mu m$, a center-to-center pitch $a = 0.9\mu m$ and a height $h = 2.5\mu m$ while varying the Bloch vector $\vec{k}_x$ from 0 to 0.5 in units of $\frac{2\pi}{a}$. From the result in figure 25a it can be clearly seen that multiple lines are present, two strong lines, and one weak but very straight line. Given the linear nature of this weak line, it is hypothesised that this is a simulation artefact caused by light that never couples to the periodic structure. Should this be the case then this line should follow the lightline equation that is trivially derived from

$$E = \hbar\omega, \omega = \frac{ck}{n}, k = \frac{2\pi}{a}k_x \tag{5.4}$$

Which are combined to form the light line equation

$$E = \frac{hc}{na}k_x \tag{5.5}$$

in which the lightline energy is given as a function of the Planck constant multiplied by the speed of light $hc \approx 1.240eV \cdot \mu m$, a the pitch in micrometres, n the refractive index of the medium and k_x the wavenumber in the band-structure units used in the analysis. The lightline for vacuum $n = 1$ and the set periodicity of $a = 0.9\mu m$ is then plotted into the figure as the

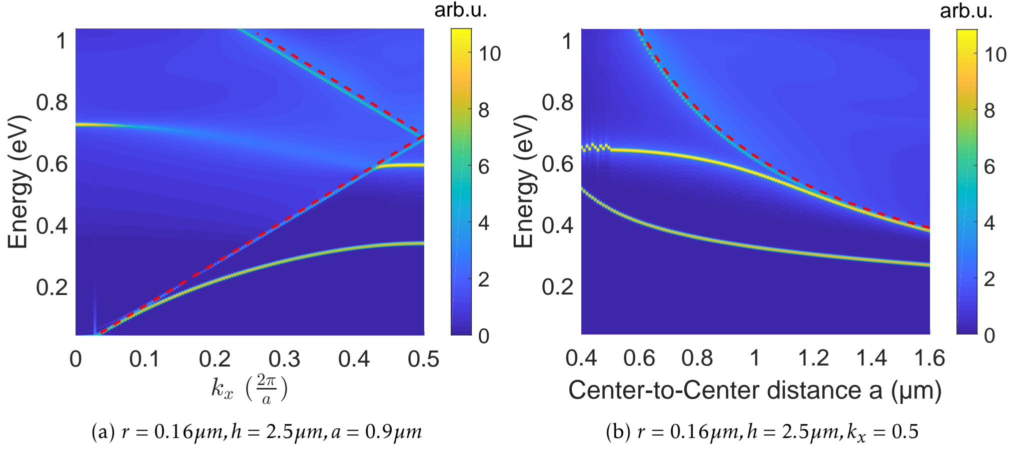

(a) $r = 0.16\mu m, h = 2.5\mu m, a = 0.9\mu m$

(b) $r = 0.16\mu m, h = 2.5\mu m, k_x = 0.5$

Figure 25: a) The calculated bandstructure of a nanowire array with $r = 0.16\mu m, h = 2.5\mu m, a = 0.9\mu m$. The red dashed line shows the lightline according to equation 5.5. Below the light line there are two features visible, the dielectric band (lowest) and the air band (highest). The slow light is found at the dielectric band edge for $E = 0.35eV$ at $k_x = 0.5$. b) The shift of the bandedges when varying the center-to-center pitch a while keeping $k_x = 0.5$ fixed. Again the red dashed line shows the calculated lightline. When the pitch a is decreased, the energy of the bandedges is raised, and vice-versa showing that the bandedge energies are tunable.

red dashed line confirming the observation. As any mode above the lightline is a radiative or "leaky" mode instead of a guided, confined mode, only the features below the lightline have to be considered.

The bottom line is the dielectric band DB which shows the energy of the guided mode for each wave vector. These modes are confined mostly inside of the nanowires, which is where we will have our gain. In contrast, the second line represents the Air band (AB) for which most of the field is outside the nanowires and therefore outside the gain material. The DB has its peak at the $k_x = 0.5$ point which coincides with the band levelling off to be almost horizontal at $\sim .35eV$ this is the dielectric band-edge (DBE). It is at this point that the extremely low group velocity, and therefore optimal gain enhancement, is realised while the light is confined into the gain medium. Therefore while sweeping r and a, only this k-point is evaluated.

Instead of varying k_x, we can now choose to vary a while keeping $k_x = 0.5$ resulting in figure 25b. The "free-space" artefact again matches with equation 5.5 indicated with red dashes and can be ignored. Compared to the DBE position in figure 25a, if the pitch is increased or decreased the DBE moves to lower or higher energies respectively. Therefore it is possible to tune the bandedge position to exactly match the emission energy of the material. The calculation of the bandedges is extended in

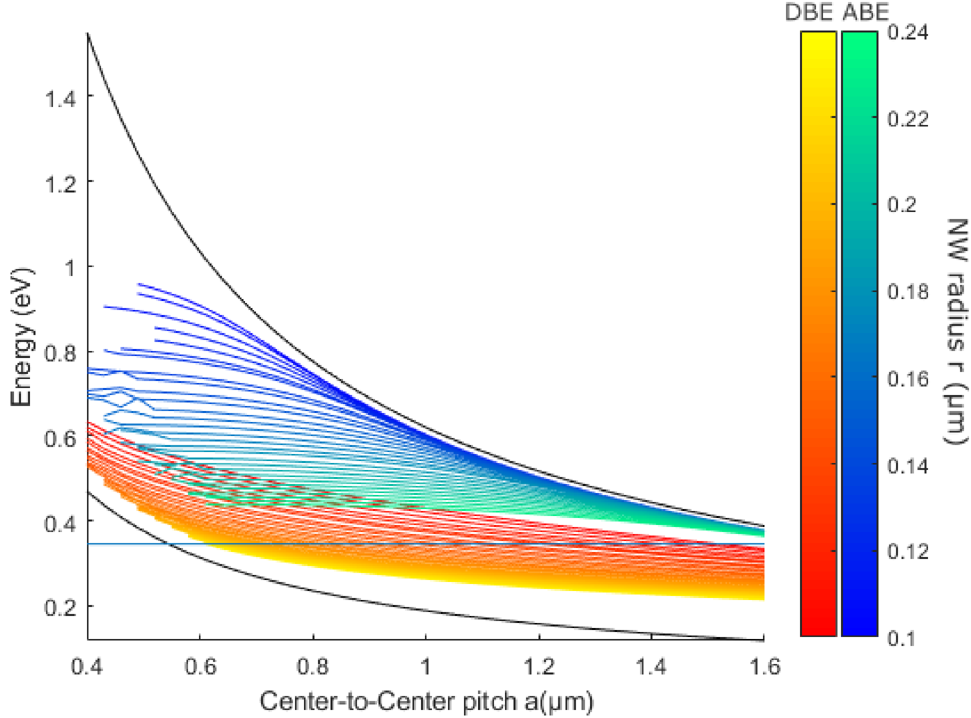

Figure 26: The total radius of the nanowires (core+shell) is shown by the color from $200nm$ (dark red, dark blue) to $440nm$ (yellow, teal). The target energy is shown by the horizontal blue line at $0.356eV$. Additionally the lightlines of vacuum ($n = 1$) and the GaAs substrate ($n \approx 3.3$) are shown with the respective upper and lower black lines.

figure 26 by choosing multiple radii in addition to varying a. The DBE can be tuned from $0.53eV$ down to $0.22eV$ by matching the right r and a. As the higher energy band-edges can be achieved only by minimising the wire thickness and the spacing, in practice the limit will be determined by the fabrication. Next to the band-edges, there are 3 more lines in the figure, the two black lines show the lightline for air (top) and the lightline for the GaAs substrate (bottom). Because the lightline for the GaAs is below the band-structure, we expect to leak light from the structure into the substrate giving additional loss. However, as these simulations are 2D, the vertical coupling is neglected and the loss cannot be quantified unless the simulations are repeated as much more computationally expensive 3D simulations which could not be performed due to time limitations. The blue horizontal line shows the emission energy of pure 100% germanium of $0.356eV$, this line cuts though a big part of the DBE results, meaning there is a lot of tuning possibility in combining r and a to get the correct band-edge energy.

The data of figure 26 can be rewritten to a generalised curve for both band-edges by reworking the data to have the dimensionless axes $\frac{r}{a}$ and $\frac{a}{\lambda}$ with λ the wavelength corresponding to the band-edge energy. Additionally these calculations can be repeated for other SiGe compositions because the different alloys have different refractive indices. Therefore in addition to the 100% germanium alloy, the generalised design curve is also calculated for the 97% and 87.5% germanium alloys with their respective emission energies of $0.384eV$ and $0.479eV$. The resulting relation for these three alloys are shown in figure 27. From this generalised result, matching combinations can be determined by choosing λ as the wavelength matching the emission energy, and choosing a pitch a and determining the accompanying ratio $\frac{r}{a}$ and r by finding the x-value at the intersection with the plotted DBE line. If required, the position of the ABE can then be determined by taking the $\frac{r}{a}$ and finding the y-value when at the intersection with the plotted ABE line.

To further illustrate the process, an example calculation is shown for 100% germanium with a corresponding wavelength of $3.48\mu m$ and a pitch of $1\mu m$. This process is annotated in figure 27 using the black arrows. First $\frac{a}{\lambda}$ is computed to be 0.287, the corresponding $\frac{r}{a}$ for 100% germanium is 0.14 giving a nanowire radius of $140nm$. Afterwards from $\frac{r}{a} = 0.14$ point we can find the ABE to be at $\frac{a}{\lambda} = 0.47$ or $\lambda = 2.1\mu m$ which corresponds with an energy of $0.58eV$ resulting in a bandgap of $E_{bg} = 0.23eV$.

Using this technique, we can get the matching combinations of pitch and radius for which the bandedge energy matches the emission energy (figure 28a) and in addition the band gap for these matching combinations is determined (figure 28b). For the pure germanium, the tuning range is the largest with approximately $0.6 \leq a \leq 1.45\mu m$ and $0.1 \leq r \leq 0.22\mu m$. When increasing the Si-content in the alloy, the tuning range is decreasing from around $0.55 \leq a \leq 1.3\mu m$ and $0.1 \leq r \leq 0.215\mu m$ for 97% to $0.45 \leq a \leq 0.85\mu m$ and $0.1 \leq r \leq 0.175\mu m$ for 87.5%.

This happens because changing the alloy composition changes both the refractive index and the target emission energy. The higher silicon content increases the emission energy, this means the structures need to be designed smaller for the bandedge energy to match. On the other hand the refractive index of the higher silicon content is lower, which allows for slightly larger structures. Effectively the structures need to decrease in size as the former effect is stronger which matches the observation.

While the parameters can be tuned to get the energies matched, from figure 28b it is evident that not all of the parameter combinations are equal. The observed increase in bandgap in figure 28b is expected to be caused by better localization of the guided mode inside the structure. This

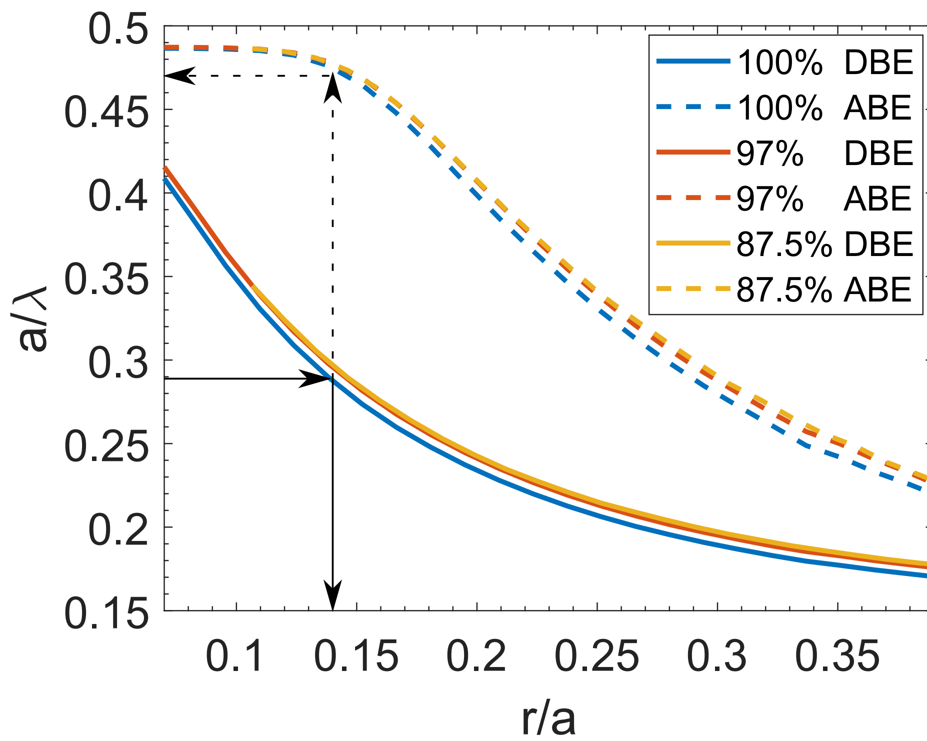

Figure 27: Generalized design parameters for different SiGe compositions for the location of the DBE and the ABE. Here a is the center-to-center pitch, r is the total nanowire radius and λ is the bandedge position wavelength from $\lambda = \frac{E}{hc}$. The black lines arrows indicate how the figure should be read.

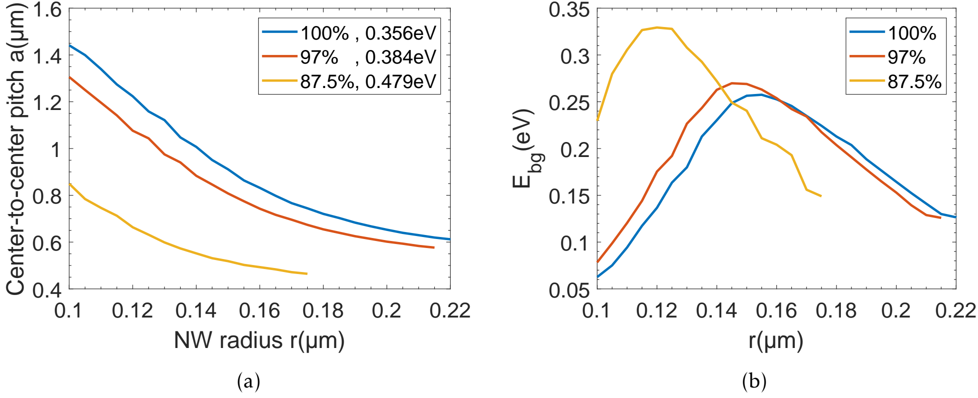

Figure 28: a) The combinations of a and r for which the DBE energy matches the emission energy for the 100%, 97% and 87.5% alloy compositions considered and b) the photonic bandgap E_{bg} determined for said matching combinations.

increased overlap of the mode with the gain material is expected to give the highest gain enhancement and therefore the combination of a and r for which the bandgap is maximum will be considered as the target design parameters for fabrication. This combination for the 100% germanium alloy is estimated to be around by $r = 0.155\mu m, a = 0.864\mu m$, for 97% it is around $r = 0.145\mu m, a = 0.846\mu m$ and for 87.5% this combination is found to be around $r = 0.120\mu m, a = 0.663\mu m$.

5.3.1 Further verification and stability

For the main simulations, certain assumptions were made. In this section some additional variables of the simulation will be checked for their influence on the previously found result.

In the previous simulations, the photonic bandstructure is optimised for the center of the PL peak. The measured PL spectrum of pure germanium (figure 4a) is quite broad, therefore we additionally investigate the optimum parameters at the energies on both sides of the FWHM of the peak. As the FWHM is approximately $30meV$ broad, the points $\pm 15meV$ are evaluated around $0.356eV$ using the curve from figure 27. The alternative design parameters are plotted together with the normal parameters in figure 29a and 29b. The points $\pm 15meV$ approximately give a change of $\mp 7\%$ in a for the same r. This means that quite a big range of parameters should still have a photonic effect on the PL as the band edge energy is still positioned within the FWHM. This available window should allow for some variation in the growth, for example if the shell is slightly too thick or too thin, while retaining the photonic effect.

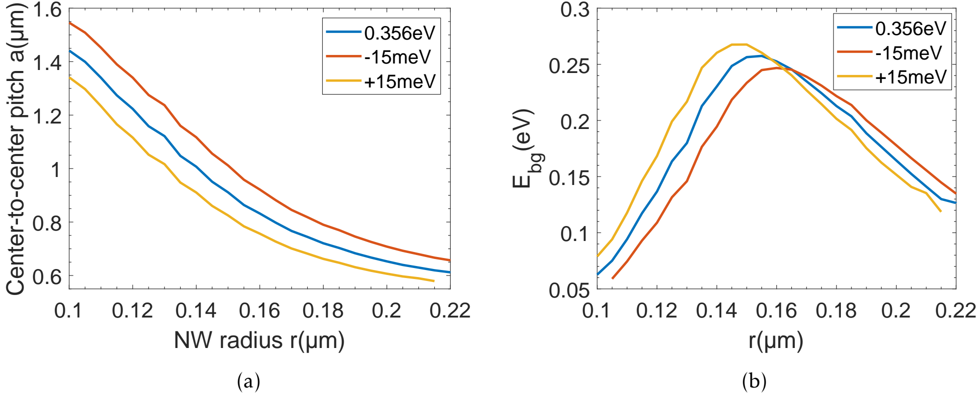

Figure 29: a) The combinations of a and r for which the DBE energy matches 100% Germanium emission, not only for the PL peak energy $0.356eV$ but also for both sides of the $30meV$ FWHM. b) The photonic bandgap E_{bg} determined for said matching combinations. This result shows that a change in bandedge position due to variations in a and r during growth or otherwise, while no longer matched with the PL peak center, should still be positioned within the PL FWHM. This means that the PL should still be influenced by the photonic crystal.

Secondly, we previously assumed the nanowires to be oriented "Face-to-Face" (F2F) (figure 30A). However the orientation is hard to control during fabrication, as the patterned nanowires should then exactly match the crystal orientation of the substrate. Therefore we compare the simulation result for the two extrema, the F2F and the 30 deg turned "Point-to-Point" (P2P) orientation (figure 30B), to see if there is a significant change in photonic bandstructure when the orientation is different. This difference in generalised bandedge positions is shown in figure 30C and it is visible that the difference is small. The DBE does not move significantly, but the ABE on the other hand moves slightly. The $\frac{a}{\lambda}$ is around 1% higher for the same $\frac{r}{a}$ so when r and a are kept constant, the corresponding band edge position λ is slightly smaller. The smaller wavelength means an increase in the energy of the ABE, meaning the bandgap is increased, albeit only slightly. This difference is small compared to the influence of PL width, so this effect can be neglected.

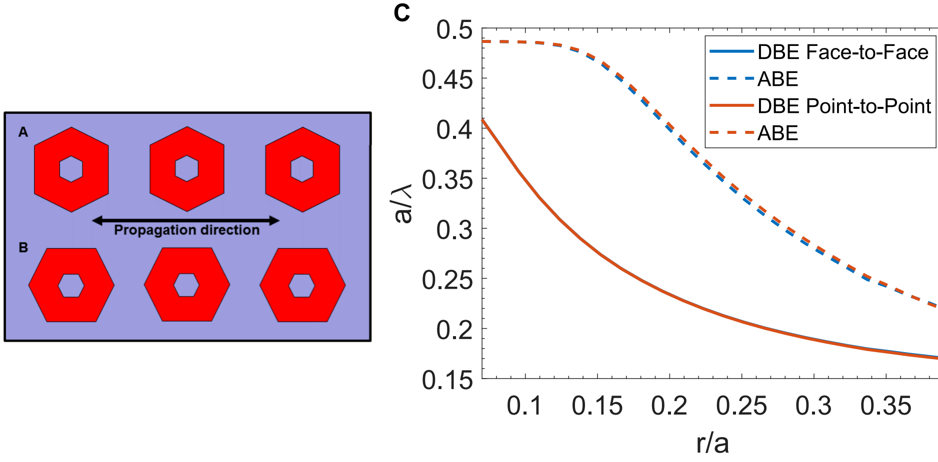

Figure 30: A schematic drawing of the nanowire orientations and the resulting effect. The nanowires are oriented either (a) Face-to-Face or 30 deg rotated as (b) Point-to-Point in the propagation direction. The effect on the generalised design parameters (c) is non-existent for the DBE and only a minor increase to higher a/λ for the same r/a and therefore higher energies for the ABE.

Furthermore the core was estimated to be very thin $d_{core} = 50nm$ to create 2-3µm long nanowires. Thicker cores, however, can be used to grow longer nanowires. To investigate the influence of the core size, the simulations are repeated for a doubled core diameter $d_{core} = 100nm$. This should be larger than the diameter we need for significantly longer nanowires in the 6-10µm range. The difference in the generalised band edge positions of the thick compared to the thin cores is shown in figure 31. The ABE is unaffected, showing no significant shift in position. The DBE on the other hand is affected, the $\frac{a}{\lambda}$ is around 1% higher for the same $\frac{r}{a}$. This means a lightly higher total radius is required if a and λ are kept constant. While an extreme case, the effect again is within the PL width variance, and therefore having a thicker core or some growth variance in general should not influence the structure significantly.

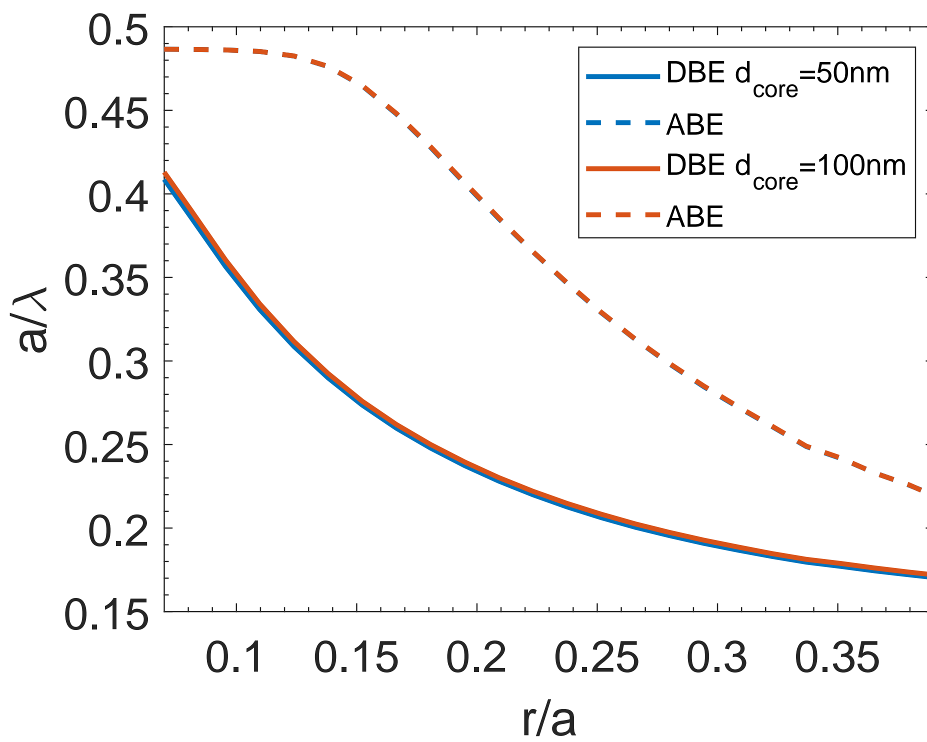

Figure 31: The effect of doubling the core size from the standard $2r_{core} = 50nm$ to $100nm$ on the generalised design parameters. The ABE is unaffected by this change, while the DBE shifts to slightly higher a/λ for the same r/a and therefore a slightly higher energy.

Continuing on this theme, to get the behaviour when changing the nanowire height a full 3D simulation is run. This simulation consists of an infinite nanowire line with a $2r_{core} = 50nm$, total radius $r = 160nm$, a center-to-center pitch $a = 0.825$ and $k_x = 0.5$ while varying $1 \leq h \leq 6\mu m$. The resulting figure 32a shows a number of features. The lowest band, the DBE, initially rapidly lowers from $\sim 0.45eV$ to $\sim 0.38eV$ when the height is increased from $1\mu m$ to $3\mu m$. After this point the energy is nearly constant as only an additional $10meV$ is lost when going to $6\mu m$. This is similar for the ABE at $\sim 0.65eV$ which in this range only loses $1meV$. Additionally the DBE fades away when the height becomes smaller. A possible cause for this phenomenon is that when the nanowires become too small, the mode starts to couple with, or leak into, the substrate. Additionally multiple additional lines descend from the air band. There are two possibilities, either these lines represent additional modes that can exist when the nanowire is long enough, or these lines are a simulation artefact. Because the additional modes were unaffected by changing the mesh density, simulation volume or PML settings, it is unlikely that the modes are an artefact.

To see how these modes behave, a $4\mu m$ long nanowire is simulated, with the bandstructure shown in figure 32b as a function of k_x. The light cone is added to the bandstructure as a red dashed line. This bandstructure shows the multiple modes present between the DBE and the ABE. The first extra mode intersects the band edge energy at $k_x = 0.33$ which is annotated in the figure with the black arrows. To compare these two modes, the spatial distribution of the field intensity is calculated for $E_{DBE} = 0.38eV$ at the $k_x = 0.33$ and 0.5 points. The resulting XZ and YZ E-field intensity profiles are shown in figure 33. From these images it can be seen that over the nanowire, the overlap between the field profile and the nanowire is better for the DBE then for the first extra mode. The extra mode has a lot more of the field intensity outside of the wire in 33b and also in 33d. Therefore, because the additional mode can couple into the wire, it can potentially parasitize on the band-edge mode. However, due to the poor overlap between this mode and the nanowire, it is probably safe to ignore for lasing as they will have little gain.

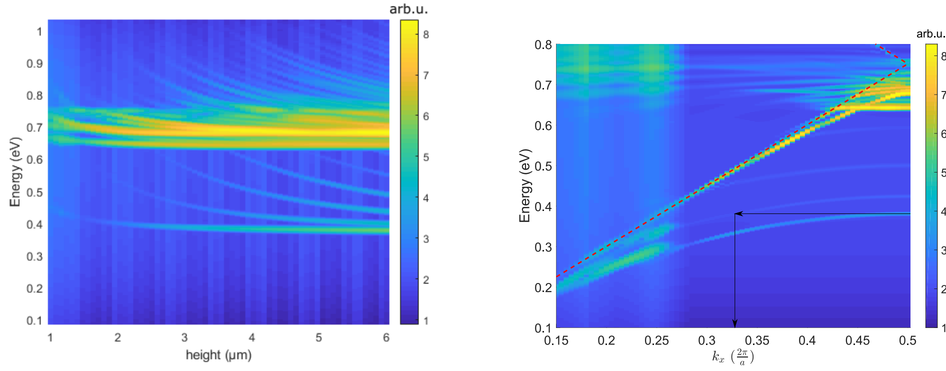

(a) $2r_{core} = 50nm$, $r = 0.16\mu m$, $a = 0.825\mu m$, $k_x = 0.5$ (b) $2r_{core} = 50nm$, $r = 0.16\mu m$, $a = 0.825\mu m$, $h = 4\mu m$

Figure 32: a) The full 3D simulation bandstructure for a nanowire $2r_{core} = 50nm$, $r = 0.16\mu m$, $a = 0.825\mu m$ and $k_x = 0.5$ while varying the nanowire height $1 \leq h \leq 6$. This shows that after 3µm the DBE is nearly constant while below it is increasing. This is probably the length where the mode starts to decouple from the substrate. Additionally it is visible that, while increasing the nanowire height, modes appear in the photonic bandgap. b) This result is confirmed by simulating the bandstructure of the nanowire at $a = 4\mu m$ while varying k_x and plotting the lightline (red dashes). Because the modes are available at all k_x, they should not be measurement artefacts. The black arrows show the $k_x = 0.33$ position where the extra mode intersects the dielectric band edge energy.

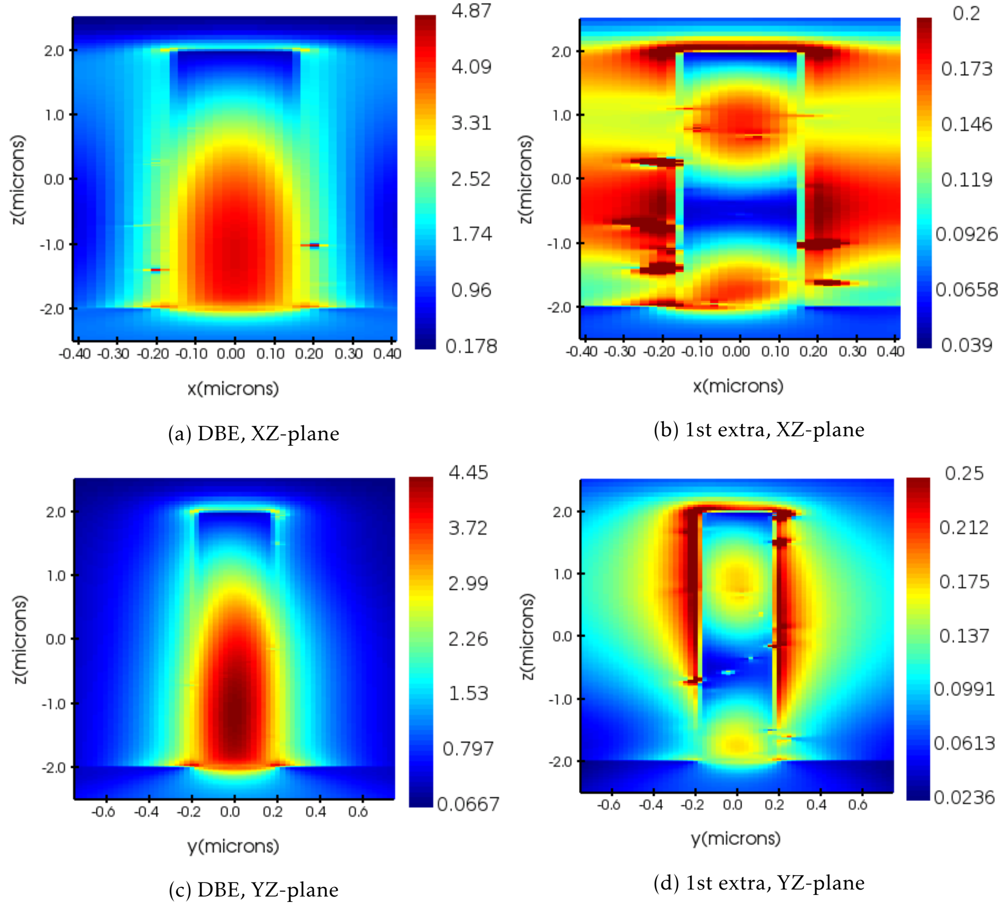

(a) DBE, XZ-plane

(b) 1st extra, XZ-plane

(c) DBE, YZ-plane

(d) 1st extra, YZ-plane

Figure 33: The comparison between the mode profiles of the DBE ($k_x = 0.5$) and the 1st extra mode ($k_x = 0.33$) at the bandedge energy $0.38eV$ in the XZ-plane in (a) and (b) and in the YZ-plane in (c) and (d) respectively. From the comparison it is evident that the overlap between the mode and the nanowire is much worse for the extra mode compared to the DBE. Intense parts of the field are mostly in-between the nanowires along the X-direction and mostly outside the nanowire in the Y direction. The DBE on the other hand has most of its field confined inside the nanowires for both X and Y directions. Due to the bad modal overlap, it is expected that the mode will behave mostly air band like, with little to no gain. Therefore we expect they can be ignored for laser design.

5.4 Fabricated structure

With the results from the simulations, we can define a structure for fabrication to verify the properties of the designed PhC. From figure 28, the combinations of matched a and r are known and the resulting bandgap.

During one fabrication run, one core radius can be chosen during the core growth and one shell thickness during the shell growth. To efficiently create different samples, it is useful to have a design that with a single specified core can be used for a multiple of combinations of radius and composition. This way a stock of cores can be grown in one core growth run and afterwards multiple shell growth runs can be done to get a variety of PBEL structures. A design like this consists of multiple lines with varying pitches such that for any viable shell, even with some of the possible variations of the previous section, a matching pitch is always available.

The design we introduce here covers a great range of pitches, $0.5 \leq a \leq 1.6\mu m$ in steps of $25nm$, resulting in 25 lines, one line of 300 nanowires for each pitch. Each nanowire position is represented by a $2r_{core} = 50nm$ circle, at these positions the EBL will expose the resist so a nanowire can be grown. This design is shown in figure 34. This range covers all pitches for 100% and 97% Germanium compositions and most for 87.5%. The lines are spaced $50\mu m$ apart, $\gg \lambda$, to ensure the lines cannot couple with each other and spaced at least $200\mu m$ from their row labels so there are no reflections.

The first attempt at growing these nanostructures is optimised for 100% germanium and an $r_{total} = 0.155$ which corresponds to the highest bandgap found before. After the core growth the sample is imaged using a SEM (figure 35) which clearly shows the lines of cores. While the locations of the wires are mostly correct and there evidently exists long range order, not everything is perfect. The cores are not all the same height, sometimes nanowires are missing and there are some parasitic nanowires in between the lines. These parasitic nanowires are probably caused by gold that redeposits after stripping the excess gold, but as they are very small they should mostly evaporate during the shell growth. The cores came out a little on the short side around $h \approx 2.3\mu m$, which will become slightly shorter still after the shell growth. After the hex-Ge shell has been grown no further SEM pictures are taken as the electron beam could damage the PL from the sample.

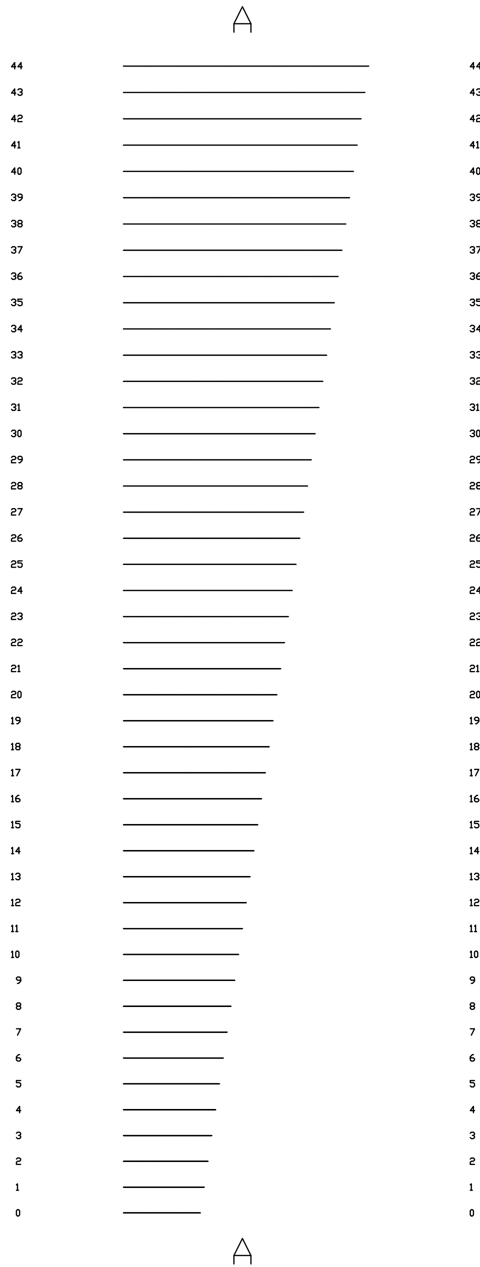

Figure 34: The PBEL line design for fabrication. The sample consists of 45 lines of 300 points with pitches varying from $0.5\mu m$ to $1.6\mu m$ in $25nm$ steps. Each point is a $100nm$ diameter circle that marks the core nanowire location for the EBL to illuminate. Row markers are included to more easily identify the pitch of the row. The lines are spaced $50nm$ apart to make sure there is no coupling between the rows and they are spaced at least $200\mu m$ from their row labels to ensure there are no reflections. This sample should, when grown with one of the determined radii for one of the three material compositions, have at least one matching line.

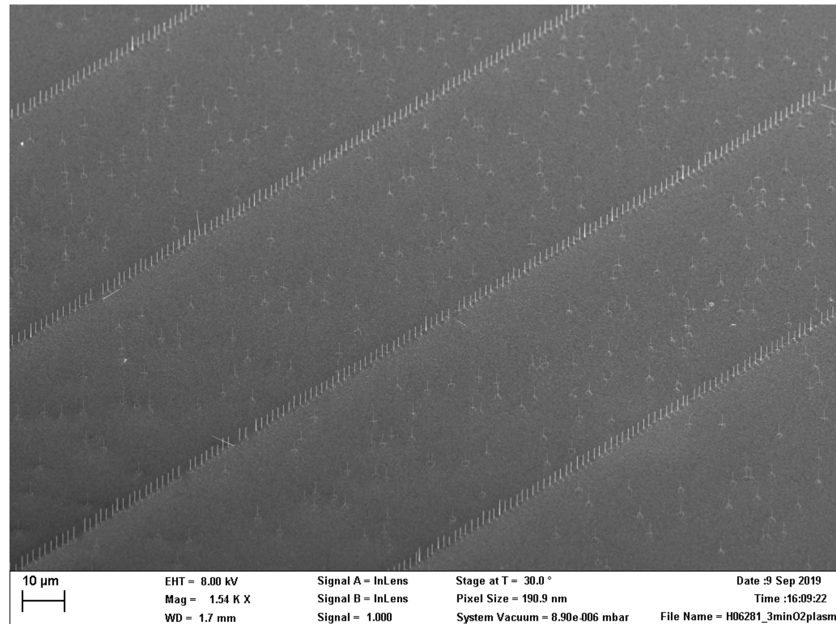

(a)

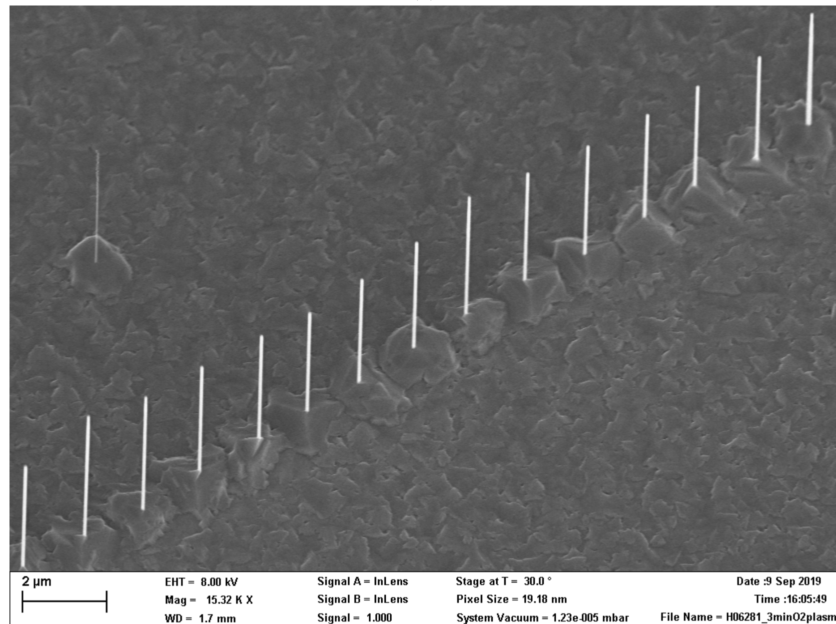

(b)

Figure 35: SEM pictures of the PBEL lines of nanowire cores both in (a) low magnification and (b) higher magnification. The images show long range order and only few defects like missing, malformed or mispositioned nanowires. There are some thin parasitic nanowires in-between the lines, but these are expected to evaporate when the germanium shell is grown. The final nanowire height is smaller than expected at only $\sim 2.3\mu m$.

5.5 FPIM results

With a first sample now grown we conduct a diffraction experiment to verify that the structure gives a coherent Bragg scattering based on its periodicity. However this will only work if the periodicity is uniform enough. The microscope with the $\lambda_{laser} = 450nm$ laser is positioned on one of the lines shown in the real space image in figure 36a. Given that the line of nanowires is straight and the nanowires are mostly equidistant, if the wires diffract well, it is expected that dots depending on the periodicity appear parallel to the real wire. However the corresponding Fourier image (figure 36) shows no such structure but only noise. There are a number of possible explanations for this.

Of course it is possible that there is still too much variance and disorder introduced in the nanowire by the growth to disturb the coherent diffraction. As seen in figure 35, the nanowire cores are not all perfectly the same height and/or not all in the exact planned position. If this is the cause, this can likely still be further improved by additional optimisation of the growth process.

Secondly, from the real image it is clear that the substrate surface around the nanowires is very rough. This results in diffuse random reflection, which can introduce this noise. Additionally, diffraction experiments like these are generally conducted on diffraction gratings. These gratings are generally large fields that consist of long ridges. As the fields are much larger than the laser spot, the complete laser spot participates in diffracting light. However on this sample there is only a single line of nanowires meaning part of the laser is missing the nanowires and instead is hitting the rough substrate. This would mean that this experiment could be more effective with a 2D photonic crystal where there are more nanowires within the laser spot so less light reaches the substrate.

Another cause could be the absorption of the hex-Ge material. The excitation laser energy $2.76eV$ corresponding to the $\lambda_{laser} = 450nm$ is much higher than the bandgap energy of germanium $0.356eV$, so the wires can also be absorbing most of the incident laser light. If the nanowires are absorbing then evidently they should also be emitting, but the $\lambda_{emission} = 3.48\mu m$ is impossible to measure with the CCD used in the setup. In addition, nanowires are known to have good absorption characteristics due to their geometry given their use in nanowire solar cells [69, 70]. This however would mean that not even 2D crystals can be measured with this technique.

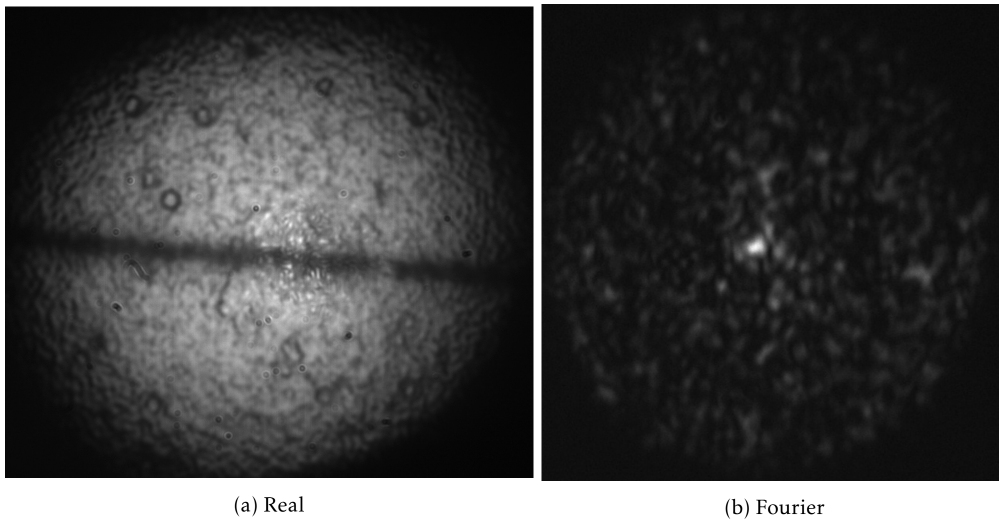

(a) Real (b) Fourier

Figure 36: a) The real-space image as seen through the microscope showing a line of wires on a rough substrate. b) The Fourier-space image of the same location. The Fourier image shows no clear diffraction pattern and consists of only the brighter laser reflection and noise.

6 Single Nanowire laser

When a new generation nanowires was introduced with a much improved maximum length, a second design path became available. The single nanowire laser, for which we use a thick, long nanowire as a Fabry-Perot cavity laser. However, light does not just travel though a nanowire randomly, the light will be travelling in a so called mode due to interfering total internal reflections from the side-facets originating from the refractive index contrast of the nanowire with its environment. Examples of these cavity modes for the GaAs/hex-SiGe core/shell nanowire are shown in figure 37. Important is to determine the minimum wire width required for a mode to become guided. This width depends on the intended emission wavelength and the refractive index at that wavelength [71]. For the derived design wavelength of the cavity, we take a $Si_{20}Ge_{80}$ composition, which results in an energy of $0.557eV$ or $2.23\mu m$ in wavelength from equation 1.1.

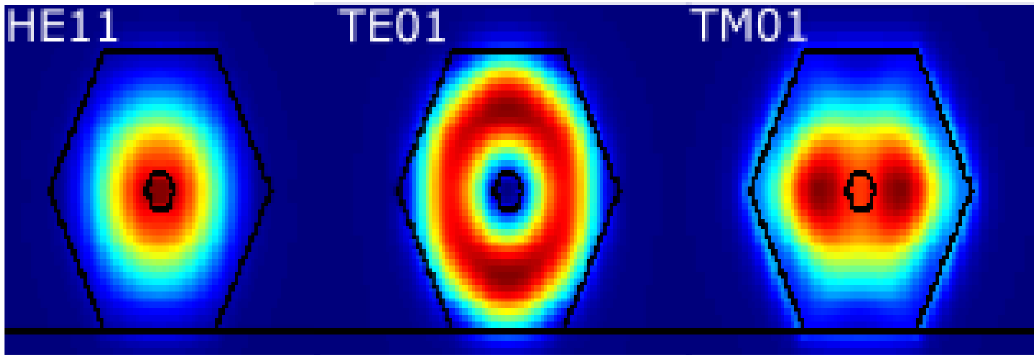

Figure 37: Normalised E-field intensity profiles of the HE11, the TE01 and the TM01 modes.

6.1 Simulation setup

To determine the guided modes and their reflection of the end facet, we define a simulation of a single 80% germanium nanowire lying on its side facet on a sapphire (Al_2O_3) substrate (figure 38). The model from Jena shown in appendix B is again used to define the material refractive index. The simulation only requires a small part of the wire to be simulated, specifically the end of the nanowire so the light can travel a short distance ($\sim 1\mu m$) and then reflect of the end facet. To make sure the light doesn't unintentionally couple to the PML, the spacing between the side facets of

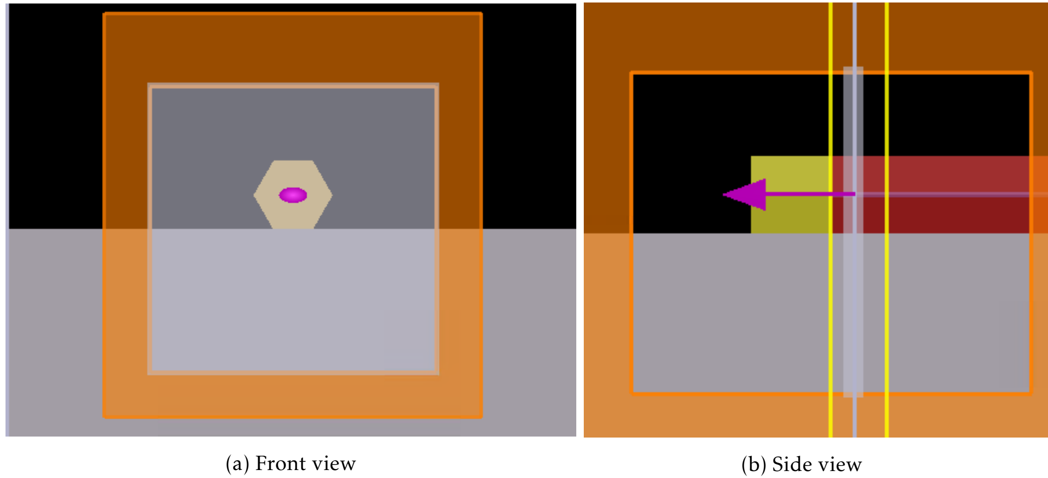

(a) Front view (b) Side view

Figure 38: A schematic front and side view of the simulation geometry showing the Wurtzite GaAs/SiGe Core/Shell nanowire with the optional gold cap on an Al_2O_3 substrate.

the nanowire and the PML is kept above two wavelengths. Optionally to increase the potential reflectivity, the end-facet can be simulated with a gold cap of $100nm$. The core diameter is set to a fixed $50nm$ diameter, while the total radius of the nanowire is varied.

The assumptions required in this simulation: A perfect nanowire is assumed, all facets are perfectly flat and untapered. Additionally, the gold is assumed to only exist on the end facet and not on the sides.

The light is injected into the simulation by a mode-source to excite a single guided mode. This source uses the refractive index profile from a cross-section of the structure perpendicular to the propagation direction to calculate the mode profiles that can exist this cross-section. This is achieved by finding the Eigenmodes by solving the Maxwell equations for this refractive index profile using a Finite Difference Eigenmode (FDE) solver [72]. The light is injected into the structure in the propagation direction in the shape of this Eigenmode and reflected off the end-facet or gold cap. The transmitted light travels further and is absorbed by the PML, the reflected light is measured by a field monitor and analysed using mode expansion. The field monitor records the time signal of the field in the cross-section of the structure behind the source (only reflected light) and then uses the chirp Z-transform to determine the spectral field profile. Then the modal reflection is calculated as the fraction of power reflected back into the source mode.

6.2 Simulation results

This calculation is done for the first 6 modes while varying the nanowire thickness and, as stated before, with and without gold cap. These modes are the HE11a, the HE11b, TE01, HE21a, HE21b and the TM01 mode. The resulting facet reflectivity as a function of nanowire radius is shown in figure 39. The Fresnel reflection calculated from the dielectric contrast using equation 5.1 and is annotated in the figure as the green dashed line at the value of $\sim 31\%$. The first modes, HE11a/b, appear when the nanowire has a radius of $\sim 0.2\mu m$. This means that the emission wavelength at this thickness starts to become guided. When the nanowire is not gold capped, the reflectivity of these modes tops out around the Fresnel reflection.

The TE01 mode, on the other hand, only starts to be guided at a higher radius of $\sim 0.29\mu m$ but it then climbs to nearly double the Fresnel reflectance at $\sim 58\%$ Which means that this mode has a lower cavity loss, and therefore should lase easier.

The HE21a/b modes, while becoming available, never have the highest reflectivity and are therefore uninteresting as they will never have the lowest loss and therefore they will never show any lasing behaviour.

The TM01 mode achieves even higher reflectivity of $\sim 66\%$. While the difference between the TM01 and the TE01 is not as big as the difference between the HE11a/b and the TE01 modes, it still has even lower mirror loss which makes it a contender for lasing as well.

The story is reversed when the end facet is capped with gold. While all modes go up significantly in reflectivity, the HE11a/b modes achieve a facet reflectivity of $\sim 85\%$, outperforming the TE01 and TM01 modes for one facet especially at thinner nanowire widths. Although both end facets will have to be covered in gold for the HE11a/b mode to actually outperform the other two modes in total mirror loss. If only one facet can be capped, the TE01 and TM01 are still superior. That is assuming the gold only influences the nanowires optically. Gold, however, is notorious for being an efficient deep-level trap in both silicon [73] and germanium [74, 75].

In the current fabrication process we can only cap one of the two end-facets. Therefore the focus will be on thicker wires optimised for the TE01 or TM01 mode as those will give the lowest loss.

The optimum nanowire diameters for the uncapped wires are given in table 1 together with the generalised ratio $\frac{nd}{\lambda}$ for which d is the nanowire diameter and $\frac{\lambda}{n}$ the wavelength inside the material which for 80% germanium is given by the vacuum wavelength $\lambda = 2.23\mu m$ and the refractive index $n = 3.483$.

Table 1: The optimal nanowire thickness for the lowest loss modes and the generalised ratio of the nanowire diameter and the wavelength in the material with with refractive index $n = 3.483$ and the vacuum wavelength $\lambda = 2.23\mu m$.

Mode	Optimum $d_{total}(nm)$	$\frac{nd}{\lambda}$
HE11a/b	580	0.92
TE01	880	1.39
TM01	1140	1.80

The E-field intensity profiles of the HE11, TE01 and TM01 mode are shown in figure 37. It is clearly visible that the field distribution in the modes is very different. The HE11a/b/ mode exists mostly in the center of the nanowire, though this does mean that a significant part of the mode exists in the core, which doesn't contribute to the gain. The TE01 mode on the other hand looks like a great modal overlap with the shell, most of this mode should therefore participate in creating gain combined with the high facet reflectivity this can be a strong contender for lasing. Finally, the TM01 mode has more of the mode profile in the shell than the HE11, but still has part of the mode in the passive core. Nevertheless, the facet reflectivity of the TM01 mode is higher.

Future experiments will have to show which of these two parameters, modal reflectivity and modal overlap with the gain medium, is more important for lasing. For the experiments conducted on the nanowires, care should be taken that the width of the nanowire at least allows for the TE01 mode to be strongly reflected at $\sim 800nm$ diameter.

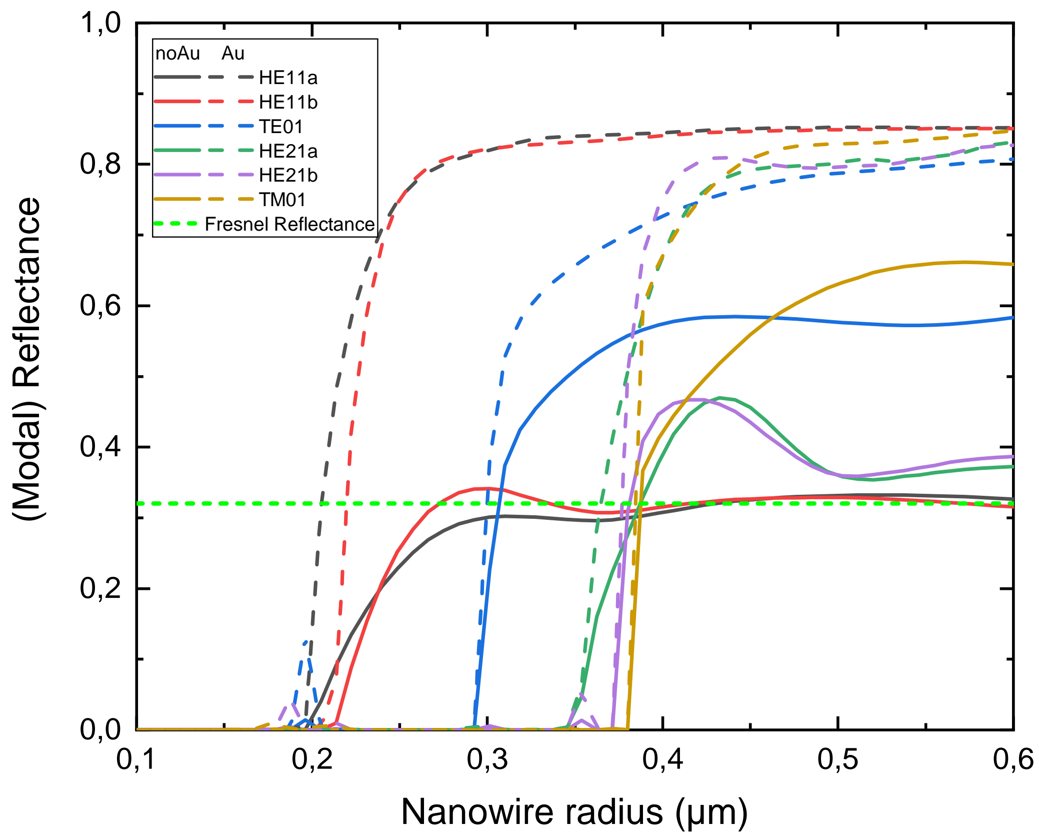

Figure 39: The modal reflection as a function of the nanowire radius for the first six available modes both with and without gold capping. The gold capped reflectance is higher than the uncapped reflectance, this suggests that gold capped wires are superior. For uncapped nanowires in order of increasing radius the HE11a/b, TE01 and the TM01 modes are the lowest loss. Interestingly, the uncapped modal reflections can exceed the bulk Fresnel reflection.

6.3 Method

The samples will be investigated primarily by Time-Resolved PL. As stated before in chapter 4.3, the TRPL experiment results in a histogram of counts as a function of time delay. An example of such a histogram is shown in figure 40. The histogram is baseline corrected by substracting the mean value calculated between $18ns$ and $25ns$ and analysed to determine two quantities.

First the total PL intensity I_{PL} is determined by calculating the trapezoidal integral from $10.72ns$ to $24.0ns$

$$I_{PL} = \int_a^b f(t)dt \approx \frac{\Delta t}{2} \sum_k (f(t_{k-1}) + f(t_k)) \tag{6.1}$$

where t_k is the time delay on bin k, Δt is the bin width of $4ps$ given the histogram f. Sometimes, to prevent the detector from saturating, a neutral density (ND) filter is placed before the detector. The intensity must then be corrected according to appendix A.

And secondly, to perform lifetime analysis, the (initial) lifetime τ is extracted by fitting a single exponential decay to the histogram from $11.4ns$ to $13.2ns$

$$Y = y_0 + Ae^{-\frac{t-t_0}{\tau}} \tag{6.2}$$

where Y is the measured value in counts, A the amplitude of the decay, τ the initial lifetime of the decay and t the time delay. The baseline $y_0 = 0$ due to the baseline correction performed before fitting, and t_0 marks the starting point of the decay which is chosen at the start of the decay. An example of this fit is plotted in figure 40 as the red line.

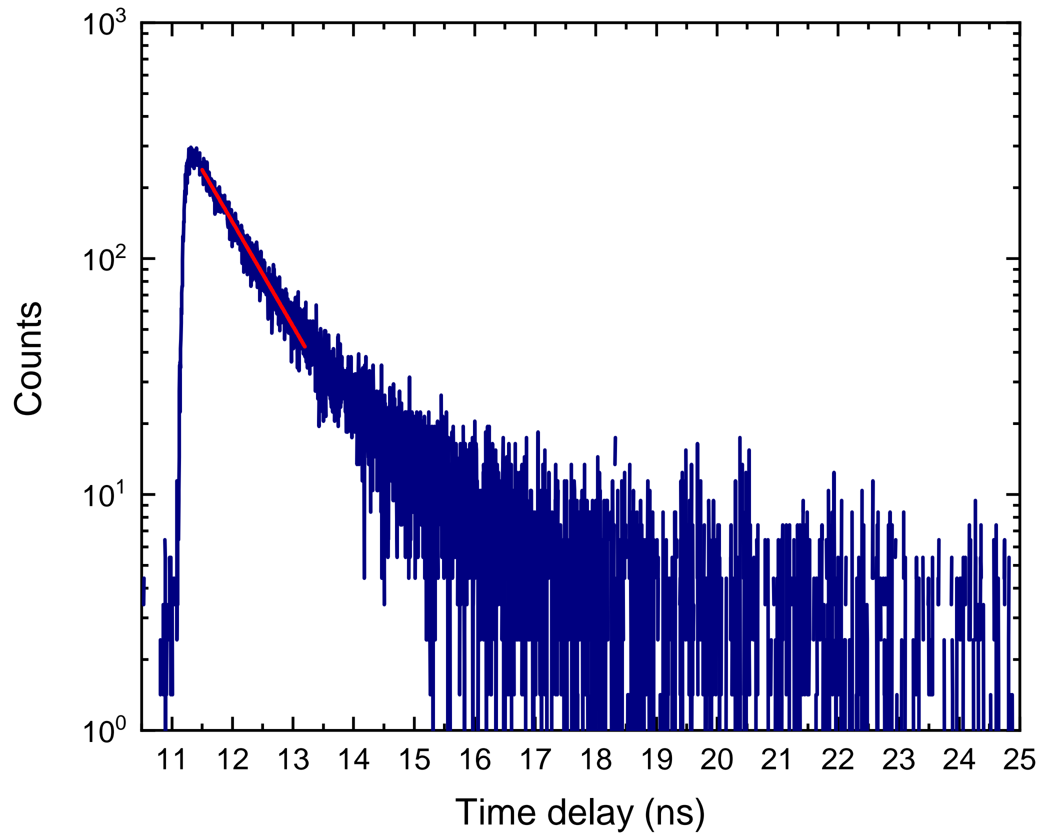

Figure 40: A baseline corrected TRPL histogram of sample I at 4K with a pulse fluence of $92\frac{\mu J}{cm^2}$ fitted with the single exponential giving $\tau = (0.98 \pm 0.01)ns$. A $ND = 0.67$ filter is used to prevent the detector from overloading. The result was not corrected for this as it is unimportant when determining the lifetime.

6.4 Results

A number of measurements are done using TRPL on swiped single nanowires to investigate the nanowires' properies for lasing. But first the properties of the measured and/or imaged samples are introduced. These samples are shown in table 2 and will be further referred to as samples I-IV. For the SiGe samples (I-III) the output composition is determined from the macro PL spectra measured at 4K using the FTIR. The peak position is then related to the composition via the empirical relation from equation 1.1 and is found to be 80%, 87% and 80% for samples I-III respectively. As sample IV was grown using only germanium it was not required to determine the composition as no silicon was introduced during growth. From these measurements it is evident that for SiGe compositions there exists some run-to-run variation in the incorporation rate as a certain input percentage does not necessarily always corresponds to the same output percentage. The geometrical properties are found from SEM images for samples I,II and IV respectively shown in figures 42a, 42b, and 50. All samples have the same nominal length around $h = 6\mu m$. Sample I has a core diameter of $2r_{core} = 188nm$ and a total diameter of $d_{total} = 1.5\mu m$. Sample II is grown from the same cores as sample I, but it is only $d_{total} = 1.0\mu m$ thick. Sample III, due to ongoing measurements, has not been imaged by SEM but as it was grown identical to sample II except a thinner core of $2r_{core} = 110nm$ was used, the other properties are assumed identical. Finally sample IV was only used for SEM images to illustrate the result of gold capping but the sizes are given for completeness, the core diameter is $2r_{core} = 182nm$ and the total diameter is $d_{total} = 0.65\mu m$. Important to note here is that samples I-III are all bigger than the previously stated $\sim 800nm$ total diameter, so at least the low loss TE01 guided mode should be available.

Table 2: The geometric and composition parameters for the measured and/or imaged samples.

Sample	Sample name	$2r_{core}(nm)$	$d_{total}(\mu m)$	$h(\mu m)$	Input ratio $Si_{1-x}Ge_x$ (%)	Output ratio $Si_{1-x}Ge_x$ (%)
I	H06196	188	1.5	6	90	80
II	H06200	188	1.0	6	88	78
III	H06291	110	1.0	6	88	80
IV	H06235	182	0.65	6	100	100

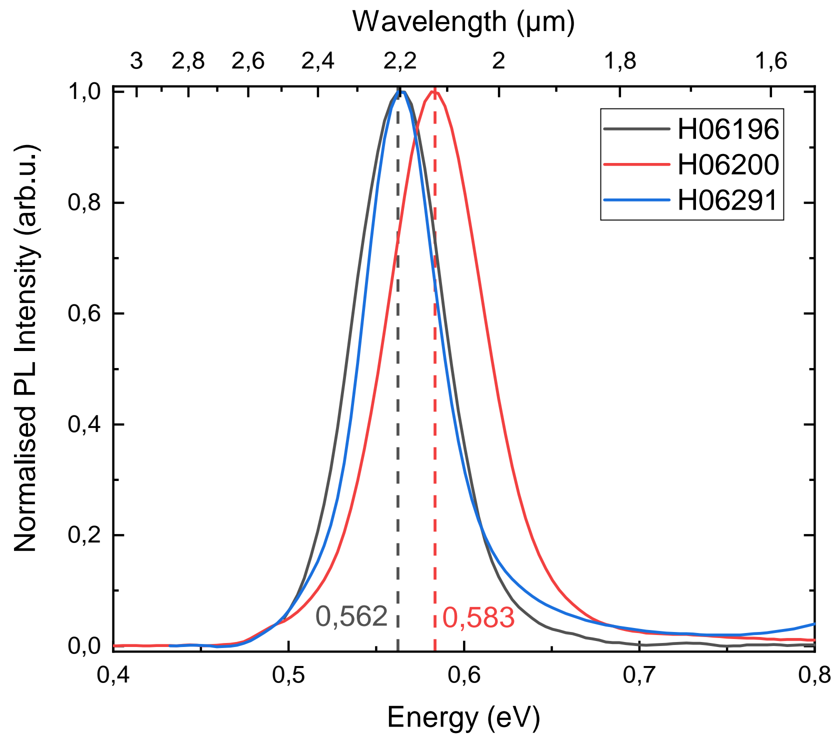

Figure 41: The FTIR comparison to determine the output alloy compositions. The spectra are measured using macro-PL at 4K with an laser power of 40mW. The peak positions are found to be $0.562eV$ for H06196 and H06291 and $0.583eV$ for H06200, using equation 1.1 this results in a composition of 80% and 78% respectively.

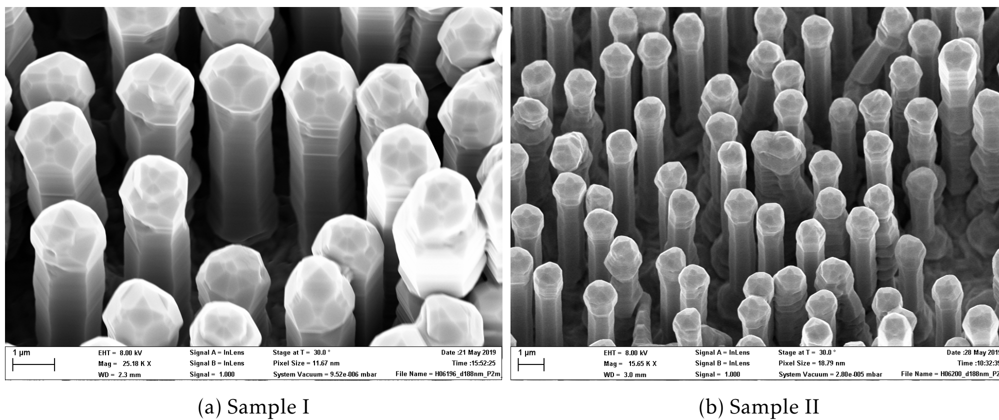

(a) Sample I (b) Sample II

Figure 42: SEM images of the nanowire arrays from (a) sample I and (b) sample II to illustrate the sample quality. The nanowires of both samples show straight side facets associated with good crystal quality but also a mushroom top.

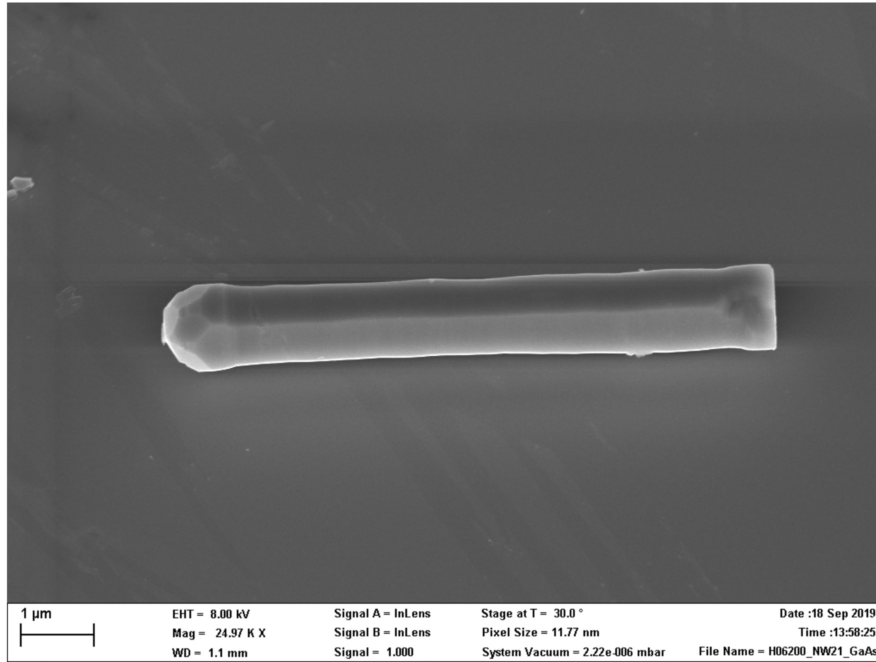

Figure 43: A SEM image of a swiped nanowire from sample II showing the flat bottom facet where the nanowire broke free from the original substrate during swiping.

The SEM images of samples I and II (figure 42) also illustrate the general nanowire quality. Most nanowires have straight side facets indicating that they have good crystal quality However, the tips of the nanowires show a dome like structure after an inverse tapered section. This combination of inverse tapering and dome is lovingly referred to as the mushroom top. The inverse tapering is expected to be caused by growth kinetics and the dome is formed when shutting down the growth and leaving the Wurtzite growth window due to cooling and subsiding precursors amounts.

In TRPL we want to do measurements on single nanowires, therefore these wire are mechanically transferred or ”swiped” from the array to another substrate. From the SEM image of a swiped nanowire in figure 43, it is visible that the bottom of the nanowire, where it broke off of the original substrate, shows a straight facet. This flat bottom facet is very desirable as it acts as an efficient mirror for the nanowire cavity closely resembling the structure from the facet reflection simulations shown previously.

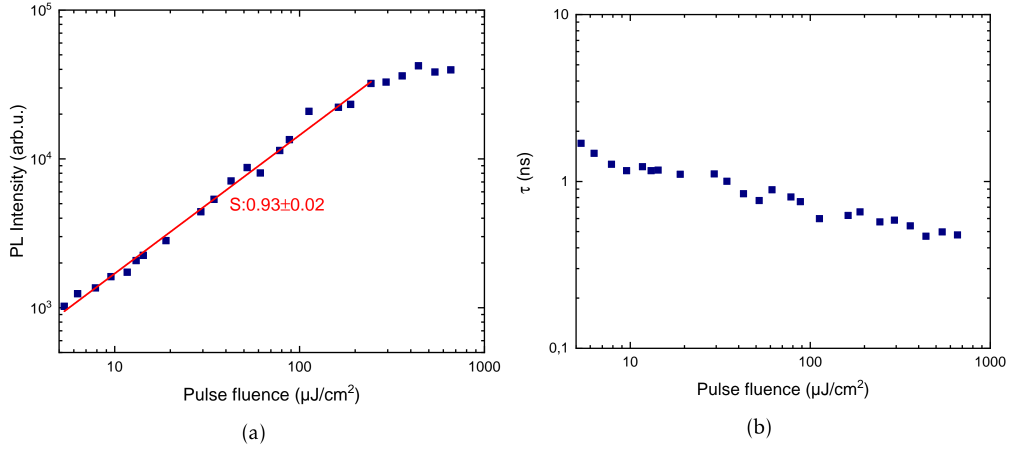

Figure 44: The a) PL intensity and b) lifetime as a function of pulse fluence. a) The intensity is showing a power slope close to unity indicating that radiative recombination is dominant. b) the lifetime is showing a steady decrease of the lifetime with increasing fluence. This could be caused by exciting close to the doping concentration, or by SRH processes due to increased temperature or by introducing new traps due to the excitation pulses.

6.4.1 Radiative limit

To create a laser it is important that the material is an efficient light emitter. Therefore the radiative recombination rate should be dominant over the non-radiative rate. We investigate this by measuring the PL of sample III as a function of power and temperature.

When the sample PL is measured for increasing pulse fluence, the found behaviour is shown in figure 44. In this measurement the slope S, from the power law $I_{PL} \propto P^S$, for the integrated PL is determined to be 0.93 ± 0.02. This value is very close to the slope of 1 expected for radiative recombination according to equation 2.2. This suggests that the sample is in the radiative regime.

On the other hand, the lifetime can be seen to slowly decrease when the power is increased. This could mean that we excite higher than, or very close to, the doping concentration after which the lifetime is expected to decrease according to equation 2.6. Alternatively this can be explained with SRH traps. Either by strongly illuminating the sample the temperature is increased such that the lifetime starts decreasing due to higher trap activity, and/or we could be actively increasing the number of traps inside the sample according to equation 2.7.

When we now measure the PL as a function of temperature on the same nanowire, we actually find a surprisingly boring yet interesting re-

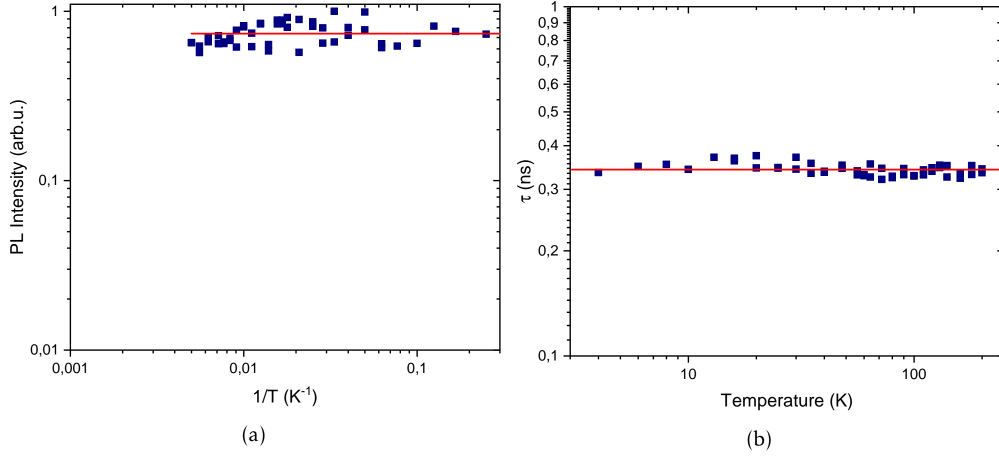

Figure 45: The a) Arrhenius plot and b) lifetime plot as a function of temperature. No characteristic SRH behaviour is found in either, the lifetime is not decreasing and the intensity did not quench unit the nanowire suddenly failed. This behaviour indicates that the radiative recombination channel is dominant.

sult. Both the total PL intensity and lifetime are completely unfazed by the increasing temperature up to a temperature of $200K$ as shown in figure 45. The Arrhenius plot in (a) does not show the rapid thermally activated quenching associated with thermally activated SRH traps and neither does the lifetime decrease in (b) as expected from equations 2.11 and 2.7. This means that SRH recombination is not dominant regardless of temperature. Giving a strong indication that the nanowire is in the radiative regime which is important for efficient light emission and one of the key properties for lasing.

After the temperature was increased above $200K$, the nanowire experienced a Rapid Uncontrolled Liquification and/or Evaporation (RULE) event. In such an event the nanowire's PL is rapidly quenched and uncorrelated black-body radiation saturates the detector. Afterwards, either the nanowire looks similar to the nanowire in figure 46, partially or completely molten, or the nanowire has disappeared entirely either by evaporating.

For most nanowires, to determine the lifetime, it is sufficient to use the single exponential function from equation 6.2. However, for some nanowires, when the initial lifetime is determined for increasing fluence, the lifetime is found to be increasing for higher fluences after the initial normal decrease. When a nanowire with this behaviour is examined in more detail, it is found that these nanowires show a histogram that takes increasingly longer to start significant decay. This behaviour is illustrated

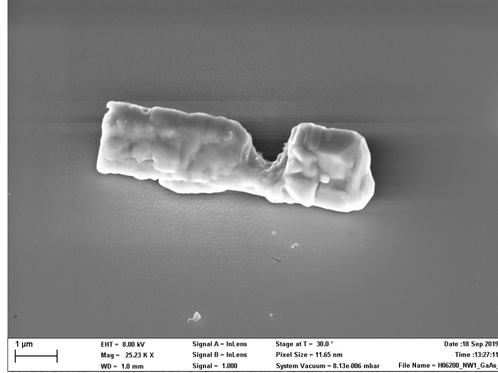

Figure 46: The SEM image of a nanowire from sample II to give an impression of the aftermath of a RULE event (the nanowire failing thermally). It is clearly visible the pulse-laser melted the nanowire and burned a hole in it.

in figure 47 for a nanowire from sample I.

This result looks similar to the result from Borgström et al. [76] where an exciton state was found to be feeding of the biexciton. Therefore we propose the hypothesis of a third state that is feeding the regular radiative transition via an intersubband transition. This would explain the flat-top behaviour as this third state emptying into the radiative recombination channel will cause it to initially saturate before starting to decay. Due to the shape of the flat top this third state is expected to be non-radiative or only very weakly, because otherwise the PL would have shown a biexponential decay due to the emission at different rates.

In principle, two such possibilities are available as shown in figure 48, either a level that feeds electrons to the radiative channel, or a level that feeds holes to the radiative channel. However, as the system is degenerately n-doped, only the level feeding holes (right) is likely. Assuming this extra level originates from the material, then figure 5 suggests this level is the second valence band at Γ^{+}_{7v+} as this is the closest available band. Coincidentally, in germanium, the band-to-band transition between this band and the conduction band should be dipole forbidden as seen from figure 5 which matches the observe non-radiative state. However we must be careful with this reasoning because, as the nanowire consists of hex-SiGe, we cannot assume the accuracy of these selection rules due to the alloy breaking the symmetry.

Such a third level might be very interesting for lasing if it can be used as a pump transition or reservoir to maintain the population inversion required in the emission band for stimulated emission. Additionally if carriers can be (partially) stored in this third state instead of in the nor-

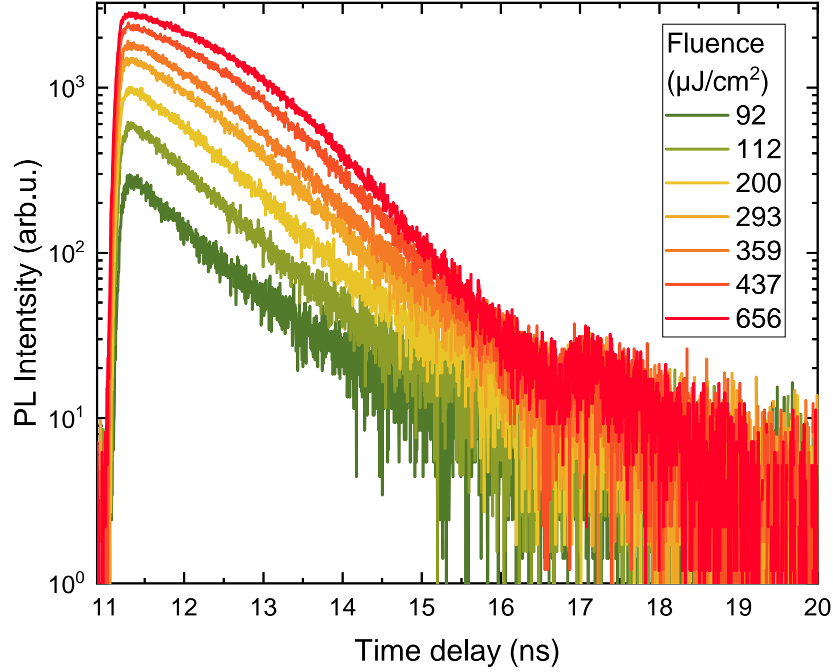

Figure 47: The PL histogram as a function of increasing pulse fluence showing the peak of the histogram broadening and flattening towards longer delays for higher fluences.

mal emission level, this could potentially help limit the gain spectrum to lower energies. This limiting behaviour originates from the increased density of states above the energy of the 3rd level because this increased reservoir slows down further band filling. The additional available states cause less carriers to be available at higher energies, therefore it cannot emit as strong at those higher energies, meaning the gain spectrum is limited to lower energies.

The nanowires showing this behaviour should be further studied by measuring the PL spectrum to determine if this third state is non-radiative or slightly radiative. If the state is radiative, the measurement can be followed up by spectrally resolved TRPL to see if the temporal behaviour is different.

Finally, repeated measurements on a nanowire while going to increasingly high excitation densities can show a permanent decrease in lifetime. This is shown in figure 49a for a nanowire of sample I. When going from the first sweep (green) to the last sweep (red) each finishing at a slightly higher excitation density, the lifetime decreases each sweep. The slight increase in the lifetime visible here for higher excitation density again is due to the previously shown flat-top behaviour. When now looking at the

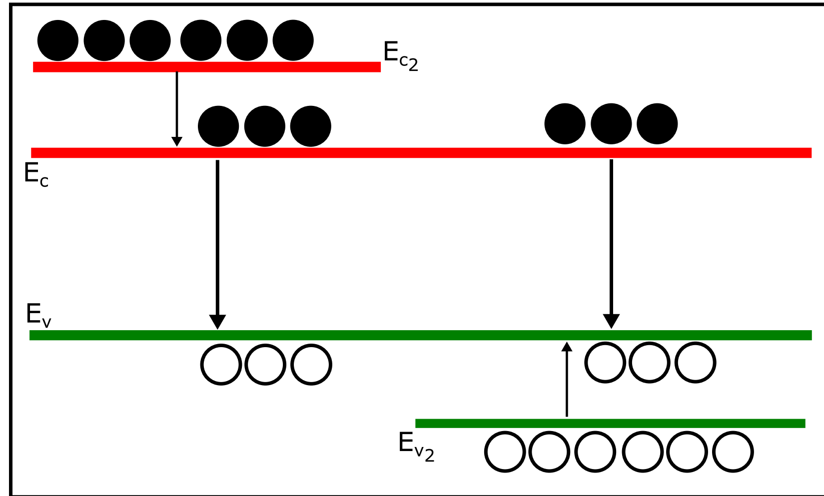

Figure 48: A schematic of the two possible three level systems, and additional conduction band level on the left and a valence level on the right. Given the degenerate n-doping of the nanowires, it is expected only changes in behaviour of the holes are visible as electrons are in excess. Therefore the right system is the most probable case.

PL intensity (b), there is a difference and the intensity is becoming lower each sweep. Interestingly, when the ratio of the PL intensity and the lifetime is plotted (c), the spread in the distribution becomes less. This means that the intensity and the lifetime are correlated which could indicate that we are creating traps inside the material causing the SRH lifetime τ_{SRH} to decrease. There are two possibilities if this is the case. Either the pump pulse is so strong that the nanowire is immediately damaged, or the damage originates from a raised temperature. The current hypothesis is that the damage is introduced thermally. The thermal contact of the nanowires with the surface may be poor because of the mushroom head, meaning only the two tips of the nanowire are in contact with the surface or a nanowire lying on its edge instead of its side facet. This could potentially be mitigated by improving the thermal contact by (partial) embedding the nanowire inside another material to increase the contact, and therefore cooling, area. Additionally, the current laser excites the sample with $1mJ/cm^2$ at a repetition rate of $40MHz$ using photons with a wavelength of $1050nm$ which corresponds to and energy of $1.18eV$. However if a laser with a lower rep rate is used, the sample has more time to cool down in-between pulses which, if the damage is indeed thermally induced, should also reduce or completely eliminate the problem. Additionally using the current laser $1.18eV$ is absorbed but only $\sim 0.6eV$ is emitted by the material, therefore approximately half the energy is lost to heat. Therefore the

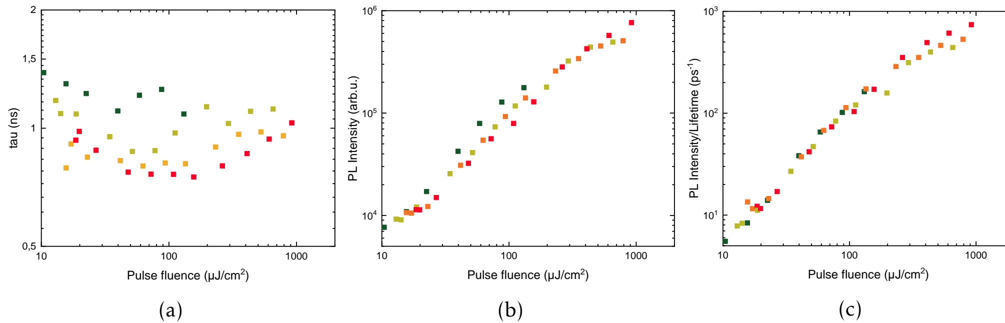

(a) (b) (c)

Figure 49: The lifetime, PL intensity and the ratio between those as a function of increasing excitation density at a rep rate of $40MHz$. The color of the point indicates in which measurement the point was measured, from the first sweep in dark green to the last sweep in red. a) The lifetime permanently decreases after going to increasingly high powers. b) The PL intensity decreases as well after higher powers have been touched. The ratio shows reduced spread compared to just the intensity indicating that the PL intensity and lifetime are correlated. This could be a sign of generating permanent traps in some wires.

above solution can be further improved by using a wavelength closer to the emission wavelength to avoid unnecessarily heating the sample.

The hex-SiGe nanowires are confirmed to be in the radiative recombination dominated regime required for lasing even up to higher temperatures like 200K which is an important step in the direction of creating a room temperature laser. Additionally we observed saturation, or flat top, behaviour in certain nanowires which is an indication of a third state feeding the radiative recombination. This third state could be interesting as a pumping level and reservoir to sustain the population inversion at the emission level. The nanowires showing this behaviour should be further studied by measuring the PL spectrum to determine if this third state is radiative or non-radiative. If the state is radiative, the measurement can be followed up by spectrally resolved TRPL to see if the temporal behaviour is different. Finally it is shown that after nanowires are exposed to very high excitation densities, the nanowires can become permanently damaged. We hypothesise this due to temperature and can be mitigated by improving the thermal contact, lowering the rep-rate and/or increasing the excitation wavelength.

6.4.2 Gold capping

When designing a laser cavity, the cavity loss should be minimised. From the modal reflectance simulation, we found the possibility to significantly increase the facet reflectivity by capping the nanowire with gold. There-

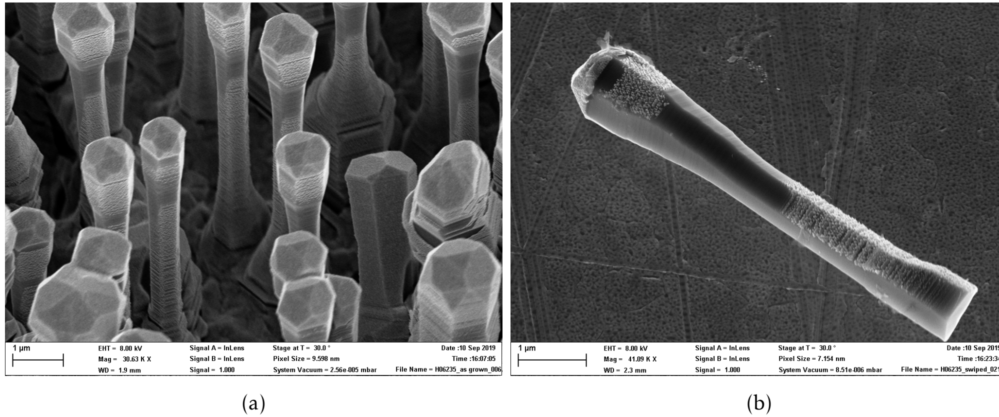

(a) (b)

Figure 50: Sem images of a) an as-grown gold capped section of sample IV and b) of a single swiped nanowire. It is visible that gold has been deposited on the top, but also on the nanowire side facets. This is likely caused by being mounted at a slight angle during the deposition.

fore we cleave a part of sample I and deposit the gold on top according to chapter 3.2 in an attempt to see enhanced PL. The result of such a deposition on standing nanowires of sample IV is shown in figure 50a. Both capped and uncapped nanowires are then transferred to separate pieces of the $Si/Cr/Au/SiO_x$ substrate, figure 50b gives an impression of how the resulting nanowires are placed on the sample. The top of the nanowire is covered in a layer of gold as expected, however there is also some deposition on the side facets of the nanowires. While the bottom facet after transfer is not covered by the metal, this facet is known to show a clean break when mechanically transferred from the original substrate and, although lower than a clean break with metal cover, the clean break is also expected to have a high reflectivity as can be seen from the simulation results.

The influence of the gold capping on the PL and the lifetime is now investigated statistically by measuring around 20 nanowires on both the capped and uncapped sample. These results are compared in figure 51 and the result is surprising. Where the capped sample was expected to be better in terms of intensity and lifetime due to the added reflectivity, it is found to be worse. The PL intensity is approximately a quarter of the uncapped nanowires and also the lifetime is down by approximately a quarter.

In principle it is possible that the nanowires are already lasing and we are just unable to observe it due to the setup not collecting the emitted laser emission. Assuming this is the case, then the lifetime would

be decreased due to an increased contribution of the the faster stimulated emission. The reduced intensity can then be explained because of increased in-plane directionality of the emission out the nanowire's end facet as only light emitted upwards can be collected by the Cassegrainian objective. Additionally, the mushroom head can no longer scatter as much light due to the gold capping reflecting more light.

However, a more probable explanation for this result is the deposition of gold on the side facets of the nanowires. These gold granules make the surface rough, which can cause increased scattering loss. Additionally as stated before, gold is a very efficient deep level trap which can diffuse in both silicon and germanium. Due to the relatively poor thermal contact, this diffusion might also be assisted by the nanowire heating up from the laser pulses. This would mean that the losses due to SRH recombination could have been increased significantly. Furthermore, the simulations were done for a gold cap on a perfectly flat end facet for a non tapered wire, while in reality, we have a reverse taper in combination with the mushroom head which has not been taken into account. This would mean that, in its current form, capping the nanowire tips with gold is actually detrimental to the PL. Finally, as gold-capping was a one-shot attempt, we might also just have been unlucky with the part of the sample that was cleaved to perform the gold capping on.

In contrast to our expectations, we observed a decrease in PL. We hypothesise that the gold deposited on the sidewalls is causing SRH recombination by functioning as a trap. To further investigate this theory the gold capped nanowires should be measured through increasing temperature to see how the Arrhenius function and lifetime compare to those of uncapped nanowires. If the gold is indeed acting as a SRH recombination center, the Arrhenius should either show an activation energy that is not present for uncapped nanowires or a much stronger quenching strength.

The gold capping process could potentially be improved by growing an oxide shell by atomic layer deposition (ALD) around the nanowire before the gold deposition to protect the hex-SiGe from direct contact with the gold.

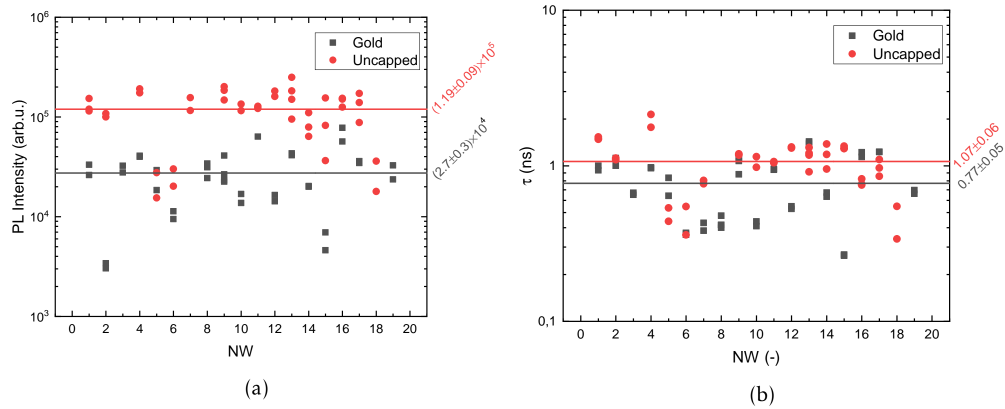

(a)

(b)

Figure 51: The results of the statistical measurement of a) the PL intensity and b) the lifetime of ~ 20 wires on both the capped and uncapped sample. The PL intensity of the capped nanowires is approximately a quarter of the uncapped wires. Additionally the lifetime is shorter by approximately a quarter. This result shows that, at least the current form of, gold capping is actually detrimental to the PL.

7 Summary & Conclusion

In this work we evaluated two hex-SiGe laser structures using numerical and experimental methods. First we dove into the design parameters of the photonic band edge laser (PBEL). For the PBEL to work, the emission energy of the hex-SiGe alloy needed to match the photonic band edge of the dielectric band. By calculating the generalised photonic crystal design parameters, it was possible to show it was possible to fulfil this requirement. The estimated target design parameters for 100% germanium are $r = 0.155\mu m, a = 0.864\mu m$, for 97% they are $r = 0.145\mu m, a = 0.846\mu m$ and for 87.5% this target is found to be $r = 0.120\mu m, a = 0.663\mu m$. It was also shown that perturbations to the design were within the margin given by the broad PL width. We also show that the nanowire height should only marginally influence the band edge location above $3\mu m$. Finally it was determined that the extra vertical modes that emerge while increasing the nanowire height have bad overlap with the nanowire and should therefore pose no danger to the band-edge lasing mode.

According to these specifications a sample was fabricated to try and verify the presence of photonic behaviour using Fourier plane imaging microscopy (FPIM). Unfortunately, the FPIM measurement was inconclusive as no diffraction pattern was found. A possible explanations for this result is the variance in the geometry and positioning that still plagued the structure. However also the rough substrate with the relatively low amount of nanowires participating in the measurement could have hampered the measurement. Finally as the bandgap of hex-Ge is $0.356eV$ and the excitation laser has a photon energy of $2.76eV$, it is also possible that the nanowires absorbed much of the incident light instead of coherently scattering it leaving a signal smaller than the noise.

Next the single nanowire Fabry-Perot laser was introduced. The facet reflectivity of an 80% hex-SiGe nanowire was determined for the first six available optical modes. From these calculations we found the HE11a/b, TE01 and the TM01 modes subsequently have the highest facet reflectivity for increasing nanowire diameter. When this result is combined with the overlap between the mode and the nanowire shell, the TE01 is found to be the most promising lasing mode at an optimal total diameter of $d_{total} = 880nm$ for a $2r_{core} = 50nm$ with a facet reflectivity of $\sim 58\%$.

Nanowires in this thickness range were then characterised using time-resolved photoluminescence. While no smoking gun was found to prove the nanowires are showing laser-like behaviour, there were some interesting findings. The nanowires showed behaviour characteristic for the radiative recombination dominated regime. A power slope near unity for

the intensity and a slowly decreasing lifetime for increasing excitation density and a lifetime and intensity that stayed constant for increasing temperature.

Furthermore we found a flat-top behaviour which we hypothesise to be a saturation effect from a third state, most probably the second valence band, feeding the radiative recombination channel via an intersubband transition. This can potentially be a very interesting property for lasing as this state could be used as a pumping transition and reservoir to maintain the population inversion required for stimulated emission in the emission state. Additionally we hypothesise that the gain spectrum could be limited to lower energies because the increased density of states from the third level slows down the band filling up to higher energies.

Another interesting effect is seen when the nanowires are exposed to very high excitation densities. Exposure to these high powers can permanently reduce the measured lifetime of the nanowire. This reduction in lifetime was found to be correlated with a proportional decrease in intensity indicating that we are creating traps in the material. We hypothesised that this damage is thermal in origin as the nanowires often have poor thermal contact with the substrate due to their geometry.

Finally from simulations it was found that capping the nanowire end facet with gold would enhance the modal reflectance across the board. The increased reflectance should lower the threshold gain which is important for lasing. However when comparing the measurements of the gold capped nanowires to the uncapped ones, both the lifetime and the integrated intensity was reduced by a quarter. This could be explained by increased directionality from a larger contribution of the stimulated emission. Though a more probable cause is that the reduction is caused by a sharp increase in SRH recombination caused by the deposited gold. Therefore we expect that the current process of gold capping of the nanowires is detrimental to the PL. To further investigate this result, the gold capped wires should be measured through temperature to see if the intensity quenches at higher temperatures indicating an increase in SRH traps.

7.1 Outlook & Recommendation

To determine if the current PBEL structure can show lasing, the PL spectrum of the different rows of nanowires should be determined as a function of excitation density. It is important that the structure is evenly illuminated using a line shaped laser spot, this can be done using a telescope made by cylindrical lenses [77]. When measuring through power, one should be on the lookout for tell-tale signs of lasing: a sharp increase in

intensity and a decrease of the PL peak width.

In addition to the 1D lines, this investigation can be repeated for a 2D photonic crystal variant of this design. Because of the additional confinement, it should be possible to increase the dielectric band edge energy towards higher energies allowing alloys with more silicon to be used while keeping realistic nanowire diameters and pitches. The FPIM measurement should also be retried for a 2D photonic crystal. Because more nanowires will participate in the diffraction compared to the lines, the signal can be stronger.

However it is important that the structure is improved from a growth perspective. The disorder in nanowire position should be reduced to make sure the scattering losses are as little as possible. Additionally the nanowire-to-nanowire variance should be further reduced to avoid strong localization or or scattering due to changes in the nanowire geometry.

Finally an interesting optimisation to the PBEL can be made by introducing a chirp into the photonic crystal [78–81]. By increasing the distance between a couple of outer nanowires at the two ends of the photonic crystal line, the band edge is lowered. By lowering the band edges, the lasing mode is now shifted into the bandgap effectively turning the outer nanowires into mirrors. This will reduce the amount of nanowires required for the laser as well as reduce its footprint and loss.

For the single nanowire Fabry-Perot laser, it is important that the thermal contact with the substrate is improved so the nanowires can handle the high excitation power up to higher ambient temperatures. This is needed because a laser integrated with electronics should be lasing at room temperature. A long term solution is to optimise the growth such that there is no longer any (inverse-)tapering or mushrooming effect. The nanowire will then lie flat on the surface improving thermal contact area. This will also benefit the threshold gain by providing a second flat end facet and less scattering and out coupling loss due to straight side facets. A stop-gap solution can be to (partially) embed the nanowires in a dielectric shell like SiO_x or Al_2O_3. This will also increase the thermal contact area with the substrate.

Another innovation required for improved compatibility with CMOS is to eliminate both the gold catalyst and the GaAs core. As discussed before, gold is a diffusing deep level trap and therefore strictly forbidden in any CMOS fabrication process. Futhermore as the GaAs core is still a III-V material and the goal is to replace the III-V materials with hex-SiGe, therefore a growth process needs to be developed to grow the material without the core present.

Finally when measuring PL on nanowires, it is important to take into

account the directionality of the emission. Because in a nanowire laser most of the light is coming out of the end facets. When designing a setup for measuring spectrally resolved µPL, care should be taken that this emitted light can be collected and measured. One solution is to keep the nanowires upright by embedding them in a transparent polymer, depositing a mirror on the top and polishing away the substrate as much as possible. The measurement can then be conducted by measuring through the remaining substrate. Another solution is to create a setup where the excitation path and emission path are separated in a two axis cryostat. The laser can be focussed by the objective though the top window as usual to excite the nanowire, however a second objective is used to collect the nanowire's emission parallel to the substrate from a window on the side of the cryostat.

References

[1] G. Moore, *Progress in digital integrated electronics*, 1975. [Online]. Available: http://www.eng.auburn.edu/~agrawvd/COURSE/E7770_Spr07/READ/Gordon_Moore_1975_Speech.pdf.

[2] A. Kannan, N. E. Jerger, and G. H. Loh, "Exploiting interposer technologies to disintegrate and reintegrate multicore processors", *IEEE Micro*, vol. 36, no. 3, pp. 84–93, May 2016. DOI: 10.1109/mm.2016.53.

[3] Tirias Research, *The 2nd generation amd epyc processor redefines data center economics*, Aug. 2019. [Online]. Available: https://www.amd.com/system/files/documents/TIRIAS-White-Paper-AMD-Infinity-Architecture.pdf.

[4] I. Cutress, *The amd threadripper 2990wx 32-core and 2950x 16-core review, feed me: Infinity fabric requires more power*, online, Aug. 2018. [Online]. Available: https://www.anandtech.com/show/13124/the-amd-threadripper-2990wx-and-2950x-review/4.

[5] N. Jones, "How to stop data centres from gobbling up the world's electricity", *Nature*, vol. 561, no. 7722, pp. 163–166, Sep. 2018. DOI: 10.1038/d41586-018-06610-y.

[6] K. Rupp, *42 years of microprocessor trend data*, Feb. 2018. [Online]. Available: https://www.karlrupp.net/2018/02/42-years-of-microprocessor-trend-data/.

[7] A. Shilov, *Amd previews epyc 'rome' processor: Up to 64 zen 2 cores*, Nov. 2018. [Online]. Available: https://www.anandtech.com/show/13561/amd-previews-epyc-rome-processor-up-to-64-zen-2-cores.

[8] P. Coudrain, P. Chausse, L. Arnaud, D. Lattard, E. Guthmuller, G. Romano, A. Gueugnot, F. Berger, J. Beltritti, T. Mourier, M. Gottardi, J. Charbonnier, S. Minoret, C. Ribiere, G. Romero, P.-E. Philip, Y. Exbrayat, D. Scevola, D. Campos, M. Argoud, N. Allouti, R. Eleouet, A. Garnier, C. F. Tortolero, C. Aumont, D. Dutoit, C. Legalland, J. Michailos, S. Cheramy, G. Simon, P. Vivet, R. Velard, A. Vinci, F. Ponthenier, A. Farcy, and R. Segaud, "Active interposer technology for chiplet-based advanced 3d system architectures", in *2019 IEEE 69th Electronic Components and Technology Conference (ECTC)*, IEEE, May 2019. DOI: 10.1109/ectc.2019.00092.

[9] T. Alexoudi, N. Terzenidis, S. Pitris, M. Moralis-Pegios, P. Maniotis, C. Vagionas, C. Mitsolidou, G. Mourgias-Alexandris, G. T. Kanellos, A. Miliou, K. Vyrsokinos, and N. Pleros, "Optics in computing: From photonic network-on-chip to chip-to-chip interconnects and disintegrated architectures", *Journal of Lightwave Technology*, vol. 37, no. 2, pp. 363–379, Jan. 2019. DOI: 10.1109/jlt.2018.2875995.

[10] D. Miller, "Device requirements for optical interconnects to silicon chips", *Proceedings of the IEEE*, vol. 97, no. 7, pp. 1166–1185, Jul. 2009. DOI: 10.1109/jproc.2009.2014298.

[11] N. Jiang, P. Parkinson, Q. Gao, S. Breuer, H. H. Tan, J. Wong-Leung, and C. Jagadish, "Long minority carrier lifetime in au-catalyzed GaAs/AlxGa1-xAs core-shell nanowires", *Applied Physics Letters*, vol. 101, no. 2, p. 023 111, Jul. 2012. DOI: 10.1063/1.4735002.

[12] A. Liu and Y. Rosenwaks, "Excess carriers lifetime in InP single crystals: Radiative versus nonradiative recombination", *Journal of Applied Physics*, vol. 86, no. 1, pp. 430–437, Jul. 1999. DOI: 10.1063/1.370748.

[13] O. Semyonov, A. Subashiev, Z. Chen, and S. Luryi, "Radiation efficiency of heavily doped bulk n-InP semiconductor", *Journal of Applied Physics*, vol. 108, no. 1, p. 013 101, Jul. 2010. DOI: 10.1063/1.3455874.

[14] P. Y. Yu and M. Cardona, *Fundamentals of Semiconductors*. Springer Berlin Heidelberg, 2010. DOI: 10.1007/978-3-642-00710-1.

[15] E. M. T. Fadaly, A. Dijkstra, J. R. Suckert, D. Ziss, M. A. J. v. Tilburg, C. Mao, Y. Ren, V. T. v. Lange, S. Kölling, M. A. Verheijen, D. Busse, C. Rödl, J. Furthmüller, F. Bechstedt, J. Stangl, J. J. Finley, S. Botti, J. E. M. Haverkort, and E. P. A. M. Bakkers, "Direct bandgap emission from hexagonal ge and sige alloys", Nov. 2, 2019. arXiv: http://arxiv.org/abs/1911.00726v1 [cond-mat.mes-hall]. [Online]. Available: http://arxiv.org/pdf/1911.00726v1.

[16] C. Rödl, J. Furthmüller, J. R. Suckert, V. Armuzza, F. Bechstedt, and S. Botti, "Accurate electronic and optical properties of hexagonal germanium for optoelectronic applications", *Physical Review Materials*, vol. 3, no. 3, Mar. 2019. DOI: 10.1103/physrevmaterials.3.034602.

[17] C. Kittel, *Introduction to Solid State Physics*. John Wiley & Sons Inc, Oct. 28, 2004, 704 pp., ISBN: 047141526X. [Online]. Available: https://www.ebook.de/de/product/4290142/charles_kittel_introduction_to_solid_state_physics.html.

[18] M. Wanlass, P. Ahrenkiel, D. Albin, J. Carapella, A. Duda, K. Emery, D. Friedman, J. Geisz, K. Jones, A. Kibbler, J. Kiehl, S. Kurtz, W. McMahon, T. Moriarty, J. Olson, A. Ptak, M. Romero, and S. Ward, "Monolithic, ultra-thin GaInP/GaAs/GaInAs tandem solar cells", in *2006 IEEE 4th World Conference on Photovoltaic Energy Conference*, IEEE, 2006. DOI: 10.1109/wcpec.2006.279559.

[19] A. Sharkawy, S. Shi, and D. W. Prather, "Multichannel wavelength division multiplexing with photonic crystals", *Applied Optics*, vol. 40, no. 14, p. 2247, May 2001. DOI: 10.1364/ao.40.002247.

[20] *From o to l: The evolution of optical wavelength bands*, FS.COM, Oct. 2015. [Online]. Available: https://community.fs.com/blog/from-o-to-l-the-evolution-of-optical-wavelength-bands.html.

[21] J. P. P. Abraham H. Oort, *Physics of Climate*. American Inst. of Physics, Feb. 12, 1992, 564 pp., ISBN: 0883187124. [Online]. Available: https://www.ebook.de/de/product/3734296/abraham_h_oort_jose_p_peixoto_physics_of_climate.html.

[22] P. Tronc, Y. Kitaev, G. Wang, M. Limonov, A. Panfilov, and G. Neu, "Optical selection rules for hexagonal GaN", *physica status solidi (b)*, vol. 216, no. 1, pp. 599–603, Nov. 1999. DOI: 10.1002/(sici)1521-3951(199911)216:1<599::aid-pssb599>3.0.co;2-h.

[23] Y.-S. Yoo, T.-M. Roh, J.-H. Na, S. J. Son, and Y.-H. Cho, "Simple analysis method for determining internal quantum efficiency and relative recombination ratios in light emitting diodes", *Applied Physics Letters*, vol. 102, no. 21, p. 211 107, May 2013. DOI: 10.1063/1.4807485.

[24] T. Schmidt, K. Lischka, and W. Zulehner, "Excitation-power dependence of the near-band-edge photoluminescence of semiconductors", *Physical Review B*, vol. 45, no. 16, pp. 8989–8994, Apr. 1992. DOI: 10.1103/physrevb.45.8989.

[25] R. Hall, "Recombination processes in semiconductors", *Proceedings of the IEE - Part B: Electronic and Communication Engineering*, vol. 106, no. 17S, pp. 923–931, May 1959. DOI: 10.1049/pi-b-2.1959.0171.

[26] W. Shockley and W. T. Read, "Statistics of the recombinations of holes and electrons", *Physical Review*, vol. 87, no. 5, pp. 835–842, Sep. 1952. DOI: 10.1103/physrev.87.835.

[27] C. H. Henry and D. V. Lang, "Nonradiative capture and recombination by multiphonon emission in GaAs and GaP", *Physical Review B*, vol. 15, no. 2, pp. 989–1016, Jan. 1977. DOI: 10.1103/physrevb.15.989.

[28] M. Leroux, N. Grandjean, B. Beaumont, G. Nataf, F. Semond, J. Massies, and P. Gibart, "Temperature quenching of photoluminescence intensities in undoped and doped GaN", *Journal of Applied Physics*, vol. 86, no. 7, pp. 3721–3728, Oct. 1999. DOI: 10.1063/1.371242.

[29] T. Numai, *Fundamentals of Semiconductor Lasers*. Springer Japan, 2015. DOI: 10.1007/978-4-431-55148-5.

[30] L. Asryan and S. Luryi, "Effect of internal optical loss on threshold characteristics of semiconductor lasers with a quantum-confined active region", *IEEE Journal of Quantum Electronics*, vol. 40, no. 7, pp. 833–843, Jul. 2004. DOI: 10.1109/jqe.2004.830207.

[31] J. D. Joannopoulos, *Photonic Crystals - Molding the Flow of Light - Second Edition*. Princeton University Press, Mar. 20, 2008, 304 pp., ISBN: 0691124566. [Online]. Available: https://www.ebook.de/de/product/7088035/john_d_joannopoulos_photonic_crystals_molding_the_flow_of_light_second_edition.html.

[32] J. P. Dowling, M. Scalora, M. J. Bloemer, and C. M. Bowden, "The photonic band edge laser: A new approach to gain enhancement", *Journal of Applied Physics*, vol. 75, no. 4, pp. 1896–1899, Feb. 1994. DOI: 10.1063/1.356336.

[33] S. Nojima, "Optical-gain enhancement in two-dimensional active photonic crystals", *Journal of Applied Physics*, vol. 90, no. 2, pp. 545–551, Jul. 2001. DOI: 10.1063/1.1379354.

[34] H.-Y. Ryu, S.-H. Kwon, Y.-J. Lee, Y.-H. Lee, and J.-S. Kim, "Very-low-threshold photonic band-edge lasers from free-standing triangular photonic crystal slabs", *Applied Physics Letters*, vol. 80, no. 19, pp. 3476–3478, May 2002. DOI: 10.1063/1.1477617.

[35] C. Monat, C. Seassal, X. Letartre, P. Regreny, P. Rojo-Romeo, P. Viktorovitch, M. L. V. d'Yerville, D. Cassagne, J. P. Albert, E. Jalaguier, S. Pocas, and B. Aspar, "InP-based two-dimensional photonic crystal on silicon: In-plane bloch mode laser", *Applied Physics Letters*, vol. 81, no. 27, pp. 5102–5104, Dec. 2002. DOI: 10.1063/1.1532554.

[36] S.-H. Kwon, H.-Y. Ryu, G.-H. Kim, Y.-H. Lee, and S.-B. Kim, “Photonic bandedge lasers in two-dimensional square-lattice photonic crystal slabs”, *Applied Physics Letters*, vol. 83, no. 19, pp. 3870–3872, Nov. 2003. DOI: 10.1063/1.1626004.

[37] F. Raineri, G. Vecchi, A. M. Yacomotti, C. Seassal, P. Viktorovitch, R. Raj, and A. Levenson, “Doubly resonant photonic crystal for efficient laser operation: Pumping and lasing at low group velocity photonic modes”, *Applied Physics Letters*, vol. 86, no. 1, p. 011 116, Jan. 2005. DOI: 10.1063/1.1846148.

[38] R. E. Algra, M. Hocevar, M. A. Verheijen, I. Zardo, G. G. W. Immink, W. J. P. van Enckevort, G. Abstreiter, L. P. Kouwenhoven, E. Vlieg, and E. P. A. M. Bakkers, “Crystal structure transfer in core/shell nanowires”, *Nano Letters*, vol. 11, no. 4, pp. 1690–1694, Apr. 2011. DOI: 10.1021/nl200208q.

[39] D. Jacobsson, F. Yang, K. Hillerich, F. Lenrick, S. Lehmann, D. Kriegner, J. Stangl, L. R. Wallenberg, K. A. Dick, and J. Johansson, “Phase transformation in radially merged wurtzite GaAs nanowires”, *Crystal Growth & Design*, vol. 15, no. 10, pp. 4795–4803, Sep. 2015. DOI: 10.1021/acs.cgd.5b00507.

[40] H. I. T. Hauge, M. A. Verheijen, S. Conesa-Boj, T. Etzelstorfer, M. Watzinger, D. Kriegner, I. Zardo, C. Fasolato, F. Capitani, P. Postorino, S. Kölling, A. Li, S. Assali, J. Stangl, and E. P. A. M. Bakkers, “Hexagonal silicon realized”, *Nano Letters*, vol. 15, no. 9, pp. 5855–5860, Aug. 2015. DOI: 10.1021/acs.nanolett.5b01939.

[41] R. S. Wagner and W. C. Ellis, “VAPOR-LIQUID-SOLID MECHANISM OF SINGLE CRYSTAL GROWTH”, *Applied Physics Letters*, vol. 4, no. 5, pp. 89–90, Mar. 1964. DOI: 10.1063/1.1753975.

[42] F. Glas, J.-C. Harmand, and G. Patriarche, “Why does wurtzite form in nanowires of III-v zinc blende semiconductors?”, *Physical Review Letters*, vol. 99, no. 14, Oct. 2007. DOI: 10.1103/physrevlett.99.146101.

[43] D. Jacobsson, F. Panciera, J. Tersoff, M. C. Reuter, S. Lehmann, S. Hofmann, K. A. Dick, and F. M. Ross, “Interface dynamics and crystal phase switching in GaAs nanowires”, *Nature*, vol. 531, no. 7594, pp. 317–322, Mar. 2016. DOI: 10.1038/nature17148.

[44] J.-C. Harmand, G. Patriarche, F. Glas, F. Panciera, I. Florea, J.-L. Maurice, L. Travers, and Y. Ollivier, "Atomic step flow on a nanofacet", *Physical Review Letters*, vol. 121, no. 16, Oct. 2018. DOI: 10.1103/physrevlett.121.166101.

[45] D. Scarpellini, A. Fedorov, C. Somaschini, C. Frigeri, M. Bollani, S. Bietti, R. Nöetzel, and S. Sanguinetti, "Ga crystallization dynamics during annealing of self-assisted GaAs nanowires", *Nanotechnology*, vol. 28, no. 4, p. 045 605, Dec. 2016. DOI: 10.1088/1361-6528/28/4/045605.

[46] D. Sullivan, "Z-transform theory and the FDTD method", *IEEE Transactions on Antennas and Propagation*, vol. 44, no. 1, pp. 28–34, 1996. DOI: 10.1109/8.477525.

[47] Sullivan, *Electromagnetic Simulation 2E*. John Wiley & Sons, Jun. 7, 2013, 198 pp., ISBN: 1118459393. [Online]. Available: https://www.ebook.de/de/product/20034546/sullivan_electromagnetic_simulation_2e.html.

[48] K. Yee, "Numerical solution of initial boundary value problems involving maxwell's equations in isotropic media", *IEEE Transactions on Antennas and Propagation*, vol. 14, no. 3, pp. 302–307, May 1966. DOI: 10.1109/tap.1966.1138693.

[49] *Meep documentation, yee lattice*, Online. [Online]. Available: https://meep.readthedocs.io/en/latest/Yee_Lattice/.

[50] S. D. Gedney and B. Zhao, "An auxiliary differential equation formulation for the complex-frequency shifted PML", *IEEE Transactions on Antennas and Propagation*, vol. 58, no. 3, pp. 838–847, Mar. 2010. DOI: 10.1109/tap.2009.2037765.

[51] V. Kalvin, "Limiting absorption principle and perfectly matched layer method for dirichlet laplacians in quasi-cylindrical domains", *SIAM Journal on Mathematical Analysis*, vol. 44, no. 1, pp. 355–382, Jan. 2012. DOI: 10.1137/110834287.

[52] V. Kalvin, "Analysis of perfectly matched layer operators for acoustic scattering on manifolds with quasicylindrical ends", *Journal de Mathêmatiques Pures et Appliquées*, vol. 100, no. 2, pp. 204–219, Aug. 2013. DOI: 10.1016/j.matpur.2012.12.001.

[53] L. Mertz, "Auxiliary computation for fourier spectrometry", *Infrared Physics*, vol. 7, no. 1, pp. 17–23, Mar. 1967. DOI: 10.1016/0020-0891(67)90026-7.

[54] N. Wiener, "Generalized harmonic analysis", *Acta Mathematica*, vol. 55, no. 0, pp. 117–258, 1930. DOI: 10.1007/bf02546511.

[55] D. C. Champeney, "Power spectra and wiener's theorems", in *A Handbook of Fourier Theorems*, Cambridge University Press, 1987, pp. 102–117. DOI: 10.1017/cbo9781139171823.012.

[56] D. J. H. Davies, *The Physics of Low-Dimensional Semiconductors*. Cambridge University Press, Apr. 18, 2009, 460 pp., ISBN: 052148491X. [Online]. Available: https://www.ebook.de/de/product/2783946/j_h_davies_davies_the_physics_of_low_dimensional_semiconductors.html.

[57] M. von Ardenne, "Das elektronen-rastermikroskop", *Zeitschrift für Physik*, vol. 109, no. 9-10, pp. 553–572, Sep. 1938. DOI: 10.1007/bf01341584.

[58] K. C. A. Smith and C. W. Oatley, "The scanning electron microscope and its fields of application", *British Journal of Applied Physics*, vol. 6, no. 11, pp. 391–399, Nov. 1955. DOI: 10.1088/0508-3443/6/11/304.

[59] T. H. MAIMAN, "Stimulated optical radiation in ruby", *Nature*, vol. 187, no. 4736, pp. 493–494, Aug. 1960. DOI: 10.1038/187493a0.

[60] E. Hecht, *Optics*. Harlow: Pearson, 2014, ISBN: 978-1292021577.

[61] M. Nomura, S. Iwamoto, A. Tandaechanurat, Y. Ota, N. Kumagai, and Y. Arakawa, "Photonic band-edge micro lasers with quantum dot gain", *Optics Express*, vol. 17, no. 2, p. 640, Jan. 2009. DOI: 10.1364/oe.17.000640.

[62] H. Kim, W.-J. Lee, A. C. Farrell, J. S. D. Morales, P. Senanayake, S. V. Prikhodko, T. J. Ochalski, and D. L. Huffaker, "Monolithic InGaAs nanowire array lasers on silicon-on-insulator operating at room temperature", *Nano Letters*, vol. 17, no. 6, pp. 3465–3470, May 2017. DOI: 10.1021/acs.nanolett.7b00384.

[63] Y. Lai, S. Pirotta, G. Urbinati, D. Gerace, M. Minkov, V. Savona, A. Badolato, and M. Galli, "Genetically designed l3 photonic crystal nanocavities with measured quality factor exceeding one million", *Applied Physics Letters*, vol. 104, no. 24, p. 241 101, Jun. 2014. DOI: 10.1063/1.4882860.

[64] K. Debnath, M. Clementi, T. D. Bucio, A. Z. Khokhar, M. Sotto, K. M. Grabska, D. Bajoni, M. Galli, S. Saito, and F. Y. Gardes, "Ultrahigh-q photonic crystal cavities in silicon rich nitride", *Optics Express*, vol. 25, no. 22, p. 27 334, Oct. 2017. DOI: 10.1364/oe.25.027334.

[65] E. Palik, *Handbook of optical constants of solids*. San Diego: Academic Press, 1998, ISBN: 978-0-12-544415-6.

[66] *Sources - dipoles*, Lumerical. [Online]. Available: https://support.lumerical.com/hc/en-us/articles/360034382794-Sources-Dipoles.

[67] *Time signal for dipole source*, Knowledge Exchange, Apr. 2017. [Online]. Available: https://kx.lumerical.com/t/time-signal-for-dipole-source/5394/2.

[68] C. Jamois, R. Wehrspohn, L. Andreani, C. Hermann, O. Hess, and U. Gösele, "Silicon-based two-dimensional photonic crystal waveguides", *Photonics and Nanostructures - Fundamentals and Applications*, vol. 1, no. 1, pp. 1–13, Dec. 2003. DOI: 10.1016/j.photonics.2003.10.001.

[69] B. Tian, X. Zheng, T. J. Kempa, Y. Fang, N. Yu, G. Yu, J. Huang, and C. M. Lieber, "Coaxial silicon nanowires as solar cells and nanoelectronic power sources", *Nature*, vol. 449, no. 7164, pp. 885–889, Oct. 2007. DOI: 10.1038/nature06181.

[70] P. Krogstrup, H. I. Jørgensen, M. Heiss, O. Demichel, J. V. Holm, M. Aagesen, J. Nygard, and A. F. i Morral, "Single-nanowire solar cells beyond the shockley–queisser limit", *Nature Photonics*, vol. 7, no. 4, pp. 306–310, Mar. 2013. DOI: 10.1038/nphoton.2013.32.

[71] D. Saxena, F. Wang, Q. Gao, S. Mokkapati, H. H. Tan, and C. Jagadish, "Mode profiling of semiconductor nanowire lasers", *Nano Letters*, vol. 15, no. 8, pp. 5342–5348, Jul. 2015. DOI: 10.1021/acs.nanolett.5b01713.

[72] Z. Zhu and T. Brown, "Full-vectorial finite-difference analysis of microstructured optical fibers", *Optics Express*, vol. 10, no. 17, p. 853, Aug. 2002. DOI: 10.1364/oe.10.000853.

[73] G. Bemski, "Recombination properties of gold in silicon", *Physical Review*, vol. 111, no. 6, pp. 1515–1518, Sep. 1958. DOI: 10.1103/physrev.111.1515.

[74] H. H. Woodbury and W. W. Tyler, "Triple acceptors in germanium", *Physical Review*, vol. 105, no. 1, pp. 84–92, Jan. 1957. DOI: 10.1103/physrev.105.84.

[75] W. C. Dunlap, "Amphoteric impurity action in germanium", *Physical Review*, vol. 100, no. 6, pp. 1629–1633, Dec. 1955. DOI: 10.1103/physrev.100.1629.

[76] M. T. Borgström, V. Zwiller, E. Müller, and A. Imamoglu, "Optically bright quantum dots in single nanowires", *Nano Letters*, vol. 5, no. 7, pp. 1439–1443, Jul. 2005. DOI: 10.1021/nl050802y.

[77] J. G. Ritter, J.-H. Spille, T. Kaminski, and U. Kubitscheck, "A cylindrical zoom lens unit for adjustable optical sectioning in light sheet microscopy", *Biomedical Optics Express*, vol. 2, no. 1, p. 185, Dec. 2010. DOI: 10.1364/boe.2.000185.

[78] J. Ø. Kjellman, T. Tanemura, and Y. Nakano, "Compact photonic crystal disk cavity optimized using the gentle confinement method and boundary design", *Japanese Journal of Applied Physics*, vol. 54, no. 4, p. 042 001, Mar. 2015. DOI: 10.7567/jjap.54.042001.

[79] B.-S. Song, S. Noda, T. Asano, and Y. Akahane, "Ultra-high-q photonic double-heterostructure nanocavity", *Nature Materials*, vol. 4, no. 3, pp. 207–210, Feb. 2005. DOI: 10.1038/nmat1320.

[80] H. Kim, W.-J. Lee, A. C. Farrell, A. Balgarkashi, and D. L. Huffaker, "Telecom-wavelength bottom-up nanobeam lasers on silicon-on-insulator", *Nano Letters*, vol. 17, no. 9, pp. 5244–5250, Aug. 2017. DOI: 10.1021/acs.nanolett.7b01360.

[81] H. Kim, T.-Y. Chang, W.-J. Lee, and D. L. Huffaker, "III–v nanowire array telecom lasers on (001) silicon-on-insulator photonic platforms", *Applied Physics Letters*, vol. 115, no. 21, p. 213 101, Nov. 2019. DOI: 10.1063/1.5126721.

Appendices

A Neutral density filter calibration

When the SNSPD from the TRPL setup overloads, a neutral density filter is used to attenuate the signal. Because the filters do not necessarily have the same transmission over all wavelength, we require a calibration measurement. The effective ND is determined from the integrated PL intensity measured on sample I for which the parameters are shown in table 2. The ND value of a neutral density filter is given by

$$T = \frac{I}{I_0} = 10^{-ND} \tag{A.1}$$

where I is the intensity with the filter in place, I_0 is the intensity without the filter in place and T is the transmission ratio. The results of this analysis are shown in table 2 showing that the $ND0.3$ filter matches closely with an effective value of 0.274 while the $ND1.3$ value is significantly lower than expected at only 0.668. These calibration values are used to correct the intensity of the measurement when the detector overloads and a filter is therefore required. To now interpret the integrated PL intensity, we should calculate I_0 from the measured I using equation A.1 with the corresponding ND value.

Table 3: The calibration showing the expected and effective ND calculated using equation A.1 from integrated PL measurements on sample I at $4K$ with a pulse fluence of $131 \frac{\mu J}{cm^2}$.

ND_{spec}	$I_{filtered}(kcps)$	$I_{unfiltered}(kcps)$	$T = \frac{I_{filtered}}{I_{unfiltered}}$	ND_{eff}
0.3	(102 ± 3)	(192 ± 9)	0.532	0.274
1.3	(43 ± 3)	(201 ± 6)	0.215	0.668

B Hex-SiGe refractive index material models

To simulate the hex-$Si_{1-x}Ge_x$ with FDTD, a model of the complex refractive index as a function of frequency is required for the material. The complex refractive index is given by [60]

$$\underline{n} = n + i\kappa \tag{B.1}$$

where n is the refractive index and κ is the extinction coefficient. This material property is a by-product of the *ab initio* DFT bandstructure calculations performed by the collaborators at the Friedrich-Schiller-Universität Jena and provided by them. The refractive index of the material is calculated for each variation of an 8 atom unit cell varying from pure germanium to pure silicon. From these results the compositions $x = 1.0, 0.875, 0.75$ are relevant for the performed simulations. The complex refractive indices as a function of frequency for the $x = 1.0$ and $x = 0.875$ alloy compositions are given in figures B.1 and B.2. For $x = 0.75$, the unit cell consists of two silicon atoms and six germanium atoms. Taking into account the symmetry of the hexagonal structure, there are seven unique clusters with a slightly different refractive index. As each configuration is equally likely to be grown into the material, the seven results are averaged to a configuration averaged refractive index shown in figure B.3.

If a model is required for an intermediate composition, then the refractive index for each frequency is calculated by linearly interpolating the closest two known compositions. For example, the $x = 0.97$ data is obtained by interpolating between the models for $x = 1.0$ and $x = 0.875$.

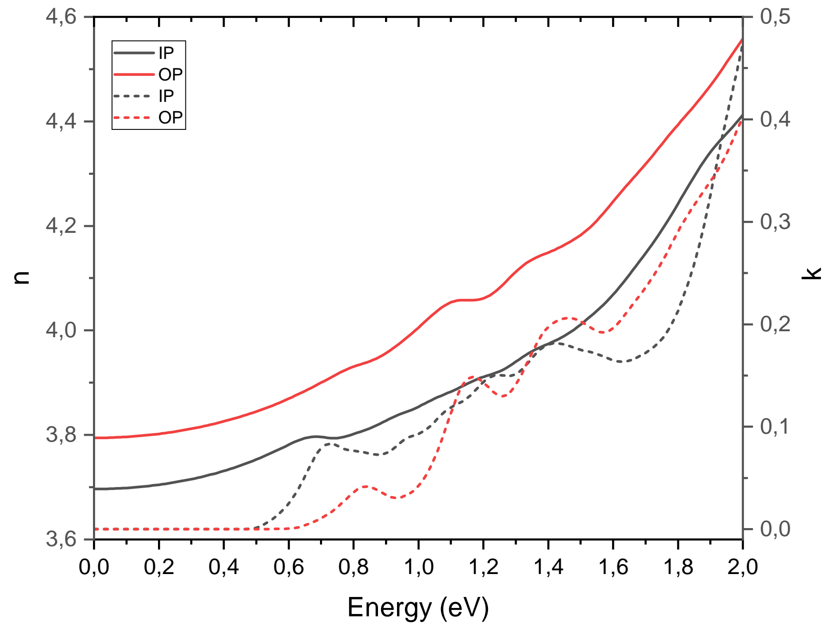

Figure B.1: The real (line) and imaginary (dashed) parts of the refractive index (line) for the in-plane x-y (gray) and out-of-plane z (red) direction for the 100% germanium alloy

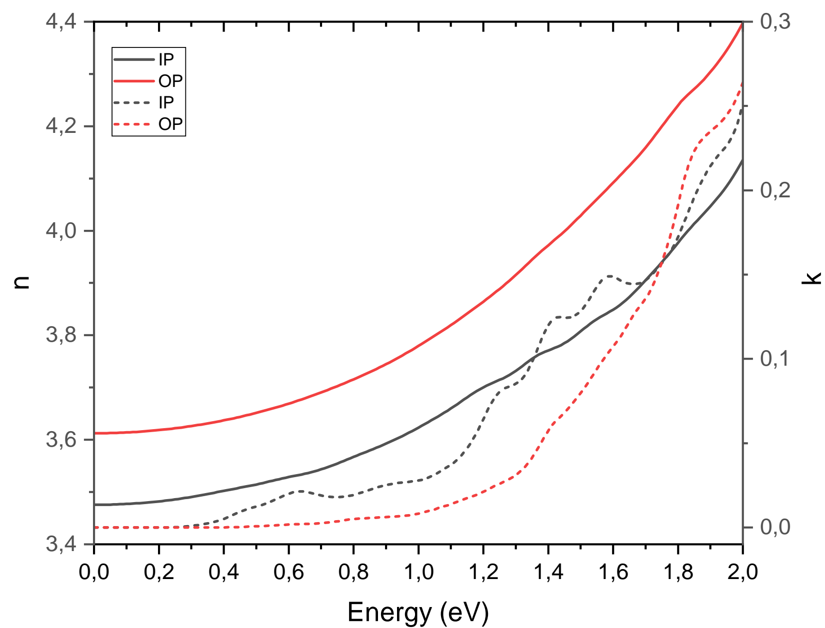

Figure B.2: The real (line) and imaginary (dashed) parts of the refractive index (line) for the in-plane x-y (gray) and out-of-plane z (red) direction for the 87.5% germanium alloy

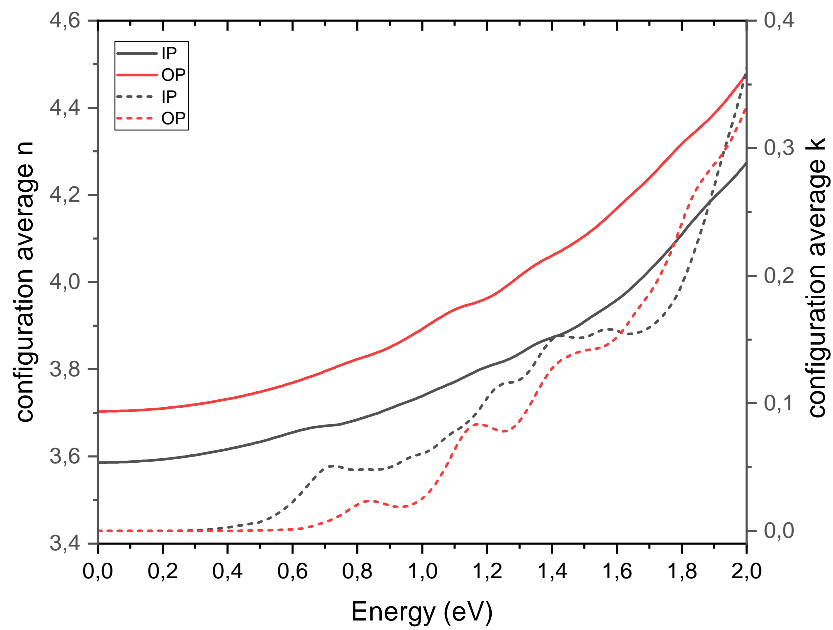

Figure B.3: The real (line) and imaginary (dashed) parts of the configuration averaged refractive index (line) for the in-plane x-y (gray) and out-of-plane z (red) direction for the 75% germanium alloy